



MAX-PLANCK-INSTITUT  
FÜR PHYSIK



---

# Towards Precision Time and Energy Measurements in Highly Granular Hadronic Calorimeters

Dissertation by  
Christian Graf

---

TECHNISCHE UNIVERSITÄT MÜNCHEN

Fakultät für Physik

MAX-PLANCK-INSTITUT FÜR PHYSIK

(Werner-Heisenberg-Institut)

Munich, March 2020



TECHNISCHE UNIVERSITÄT MÜNCHEN  
Fakultät für Physik

**Towards Precision Time and Energy Measurements  
in Highly Granular Hadronic Calorimeters**

Christian Graf

Vollständiger Abdruck der von der Fakultät für Physik der Technischen Universität München zur Erlangung des akademischen Grades eines

**Doktors der Naturwissenschaften (Dr. rer. nat.)**

genehmigten Dissertation.

Vorsitzender:

Prof. Dr. Andreas Weiler

Prüfer der Dissertation:

1. Hon.-Prof. Dr. Allen C. Caldwell
2. Prof. Dr. Bastian Märkisch

Die Dissertation wurde am 12.03.2020 bei der Technischen Universität München eingereicht und durch die Fakultät für Physik am 08.07.2020 angenommen.



## Abstract

Calorimeters with a high granularity in transverse and longitudinal direction are essential for the design of particle flow focussed detector systems at future  $e^+e^-$ -collider experiments. The CALICE scintillator-SiPM analog hadronic calorimeter (AHCAL) is such a highly granular calorimeter. This thesis studies the high precision timing capabilities on channel level of a new generation of AHCAL prototypes and their potential for the energy reconstruction.

A time calibration scheme is developed for the AHCAL using test beam data. For muons, a time resolution of 6.3 ns is achieved with a partially equipped prototype. For electromagnetic and hadronic showers the time resolution broadens due to an electronics effect occurring at higher occupancies in the detector. Late energy depositions, which are consistent with slow neutron events in their radial, longitudinal and hit energy distributions, are observed for hadronic showers. When comparing the amount of those late energy depositions to simulated data, significant deviations are observed.

It is further investigated to what extent the hit time measurements can be used to improve the energy resolution of the AHCAL. Strong correlations between late energy depositions in a hadronic shower and deviations of the reconstructed energy from the true energy are visible in simulated data of an AHCAL prototype. It is shown that these correlations can be exploited to enhance the energy resolution by about 15 % compared to the standard energy reconstruction. However, this improvement does not outperform traditional software compensation (SC) methods. It is further shown that global observables describing the hit energy spectrum of a hadronic shower can be used to correct the energy reconstruction in a similar way as observables constructed from the hit time measurements.

Finally, a machine learning setup is developed on the basis of an artificial neural network for the energy reconstruction in the AHCAL. It is shown that the longitudinal shower profiles of hadronic showers can be used to enhance the energy resolution. Together with other global features the energy resolution can be improved by up to 40 % in simulated data. This amounts to a significant enhancement over the traditional SC approach. Training the network on simulated data and subsequently applying it to test beam data leads to improvements in the energy resolution of about 30 %.

The studies presented in this thesis add to our understanding of the time development of hadronic showers in calorimeters and its simulation. Furthermore, it is shown that multivariate, machine learning based methods for the energy reconstruction hold the potential for significant improvements in the energy resolution of highly granular calorimeters.



## Zusammenfassung

Kalorimeter mit einer hohen Granularität, sowohl in transversaler als auch in longitudinaler Richtung, spielen eine wichtige Rolle in der Entwicklung neuer Detektorsysteme für zukünftige Experimente an  $e^+e^-$ -Beschleunigern mit einem Fokus auf dem Particle Flow Ansatz. Das CALICE Szintillator-SiPM Analoge Hadronische Kalorimeter (AHCAL) ist solch ein hochgranulares Kalorimeter. In dieser Arbeit werden die hochpräzisen Zeitmessungen auf Kanal-Ebene einer neuen Generation von AHCAL-Prototypen studiert und es wird das Potential dieser Zeitmessungen für eine Verbesserung der Energierekonstruktion untersucht.

Eine Zeitkalibrierung für das AHCAL basierend auf Testbeam-Daten wird vorgestellt. Für Muonen wird mit einem AHCAL Prototypen eine Zeitauflösung von 6.3 ns erreicht. Für elektromagnetische sowie hadronische Schauer wird eine geringere Zeitauflösung beobachtet. Der Grund hierfür ist ein Effekt in der Ausleseelektronik bei höheren Detektor Auslastungen. In hadronischen Schauern werden vermehrt späte Energiedepositionen gemessen, welche in ihrer räumlichen Verteilung und ihrem Energiespektrum konsistent mit denen von langsamen Neutronenprozessen sind. Die Menge der späten Energiedepositionen weicht signifikant von denen ab, die in simulierten Daten gemessen werden.

Des Weiteren wird untersucht in wie weit sich die Zeitmessungen für eine Verbesserung der Energieauflösung des AHCALs benutzen lassen. Starke Korrelationen zwischen späten Energiedepositionen und Abweichungen der rekonstruierten zur wahren Teilchenenergie sind für hadronische Schauer in der Simulation eines AHCAL Prototyps sichtbar. Es wird gezeigt, dass diese Korrelationen ausgenutzt werden können, um die Energieauflösung im Vergleich zur Standardrekonstruktion um 15 % zu verbessern. Die Verbesserung ist jedoch geringer als mit herkömmlichen Softwarekompensationstechniken (SC) möglich ist. Zusätzlich wird gezeigt, dass globale Variablen, die aus den Energiespektren der Schauer abgeleitet werden, die Energieauflösung auf eine ähnliche Weise verbessern können wie solche Variablen, die von den Zeitmessungen abgeleitet werden.

Abschließend wird ein Ansatz zur Energierekonstruktion im AHCAL auf Basis eines neuronalen Netzwerkes entwickelt. Es wird gezeigt, dass longitudinale Schauerprofile von hadronischen Schauern benutzt werden können, um die Energieauflösung zu verbessern. Zusammen mit weiteren globalen Variablen kann die Energieauflösung auf simulierten Daten um 40 % verbessert werden. Dies entspricht einer signifikanten Verbesserung gegenüber herkömmlichen SC Methoden. Wenn das Netzwerk auf simulierten Daten trainiert wird und anschließend auf Testbeam-Daten angewendet wird, verbessert sich die Energie-

auflösung im Vergleich zur Standardrekonstruktion um 30 %.

Die Analysen, die in dieser Arbeit vorgestellt werden, verbessern unser Verständnis der Zeitentwicklung von hadronischen Schauern und deren Simulation. Des Weiteren kann gezeigt werden, dass Methoden zur Energierekonstruktion, die auf modernen, neuronalen Netzwerken basieren, das Potential zu signifikanten Verbesserungen in der Energieauflösung von hochgranularen Kalorimetern haben.

# Contents

<b>Abstract</b>	<b>iii</b>
<b>Contents</b>	<b>vii</b>
<b>Introduction</b>	<b>1</b>
<b>I Theoretical and Experimental Background</b>	<b>3</b>
<b>1 Physics Foundations</b>	<b>5</b>
1.1 Open Questions in Particle Physics . . . . .	5
1.2 Future $e^+e^-$ -Collider Concepts . . . . .	8
1.3 Interaction of Particles with Matter . . . . .	11
1.4 Calorimetry . . . . .	16
1.5 Simulation of Hadronic Showers . . . . .	28
1.6 Calorimetry at Future $e^+e^-$ -Collider Experiments . . . . .	29
<b>2 CALICE Analog Hadronic Calorimeter</b>	<b>33</b>
2.1 AHCAL Concept . . . . .	33
2.2 AHCAL Physics Prototype . . . . .	36
2.3 AHCAL Technological Prototype . . . . .	37
2.4 Energy Reconstruction in the AHCAL . . . . .	42
2.5 Detector Simulation . . . . .	45
<b>II Time Analysis</b>	<b>49</b>
<b>3 Data Preparation</b>	<b>53</b>
3.1 Experimental Setup . . . . .	53
3.2 Pre-Selection . . . . .	54
3.3 Event Selection . . . . .	55
3.4 Simulation Validation . . . . .	59

<b>4</b>	<b>Time Calibration</b>	<b>67</b>
4.1	Calibration of the Reference Time . . . . .	67
4.2	Calibration of the Hit Time . . . . .	69
4.3	Evaluation of the Time Calibration . . . . .	73
4.4	Muon Time Resolution . . . . .	75
4.5	Conclusions . . . . .	78
<b>5</b>	<b>Electron Time Analysis</b>	<b>79</b>
5.1	Late Energy Depositions in Electromagnetic Showers . . . . .	82
<b>6</b>	<b>Hadron Time Analysis</b>	<b>83</b>
6.1	Using Time Information to Remove Double Particle Events . . . . .	83
6.2	Pion Time Structure . . . . .	85
6.3	The Influence of Scintillator Saturation . . . . .	89
6.4	Pion-Proton Comparison . . . . .	90
6.5	Comparison to the T3B Experiment . . . . .	91
6.6	Comparison to Steel Absorber . . . . .	91
6.7	Conclusions . . . . .	92
<b>III Energy Reconstruction</b>		<b>95</b>
<b>7</b>	<b>Data Preparation</b>	<b>99</b>
7.1	Experimental Setup . . . . .	99
7.2	Test Beam Campaign May/June 2018 . . . . .	99
7.3	Monte Carlo Simulation . . . . .	100
7.4	Shower Start Finder . . . . .	102
7.5	Event Selection . . . . .	102
<b>8</b>	<b>Energy and Time Correlation Studies</b>	<b>105</b>
8.1	Correlation of Hit Energy Observables . . . . .	106
8.2	Correlation of Hit Time Observables . . . . .	108
8.3	Correlation of Shower Observables . . . . .	112
8.4	Limited Integration Time . . . . .	113
8.5	Test Beam Data Correlations . . . . .	116
8.6	Conclusions . . . . .	116
<b>9</b>	<b>Time Assisted Energy Reconstruction</b>	<b>119</b>
9.1	Correcting for Limited Integration Time . . . . .	119
9.2	Global Software Compensation . . . . .	120
9.3	Conclusions . . . . .	124

---

<b>10 Multivariate Energy Reconstruction</b>	<b>127</b>
10.1 Artificial Neural Networks . . . . .	127
10.2 Global Variables . . . . .	130
10.3 Shower Profiles . . . . .	131
10.4 Test Beam Geometry with 38 Layers . . . . .	134
10.5 Cross Check: Electrons . . . . .	136
10.6 Conclusions . . . . .	137
<b>IV Concluding Remarks</b>	<b>139</b>
<b>Conclusions</b>	<b>141</b>
<b>Outlook</b>	<b>145</b>
<b>A Supplementary Tables and Figures</b>	<b>147</b>
A.1 Time Analysis: PTP Setup . . . . .	148
A.2 Time Analysis: Lateral Shower Shape . . . . .	149
A.3 Energy Reconstruction: SC with Additional Variables . . . . .	150
<b>Bibliography</b>	<b>151</b>
<b>Acknowledgements</b>	<b>163</b>



# Introduction

In high energy particle physics, a calorimeter is a detector for measuring the energy of incoming particles in a destructive way. Calorimeters are crucial components in nearly all detector systems and they were essential to many advancements in particle physics, for example for the discovery of the vector bosons [1, 2], the discovery of the top quark [3, 4] and most recently the discovery of the Higgs boson [5, 6]. Calorimeter systems are continuing to be invaluable for future particle physics experiments with most challenging requirements on energy, time and spatial resolution.

Novel technologies, for example the development of high performance semiconductor-based photon detectors, allow the design of large scale calorimeters with unprecedented granularity [7]. Among other benefits the high granularity allows for a better spatial separation of individual particle showers in the calorimeter. Future  $e^+e^-$ -collider experiments rely on highly granular calorimeter systems to achieve the required energy resolution in measuring particle jets, necessary for example for precision measurements of the Higgs boson [8–10]. The CALICE collaboration is developing such highly granular calorimeter systems.

After demonstrating the physical capabilities of highly granular calorimeters [11–13], the CALICE collaboration currently is in the era of technological prototypes [14], proving the technological feasibility of building such calorimeters for an application in a future  $e^+e^-$ -collider experiment. One of the projects developed within the CALICE collaboration is the CALICE scintillator-SiPM analog hadronic calorimeter (AHCAL) [15]. In 2015, a partially equipped technological prototype of the AHCAL was operated in several test beam campaigns. For the first time, the cells of a CALICE prototype were equipped with timing capabilities in the order of one nanosecond providing 5-dimensional information on hit level ( $x$ -,  $y$ -,  $z$ -position, hit energy and hit time).

A key challenge for hadronic calorimeters is the complex nature of the physics processes and their variations within hadronic showers. Calorimeters with a high granularity offer the opportunity of a detailed spatial resolution of individual particle showers, getting insight in the physics processes happening in a given shower. The information can be used to enhance the energy resolution performance of the calorimeter by weighting each shower after the measurement on an event-by-event basis. This approach is called *software compensation* and is well established within the CALICE collaboration.

With the ability of precision time measurements within the calorimeter cells a new window opens for understanding hadronic showers. Previous experiments, as for example the T3B experiment, already demonstrated the complex time structure of hadronic showers and the possibility of its measurement with granular detectors [16]. Time measurements on calorimeter cell level may provide additional information on the development of a given hadronic shower. The main goal of this thesis is to explore to what extent hit time information can be used to enhance the energy resolution of a highly granular calorimeter.

This thesis is organized in four parts. The first part sets the theoretical and experimental foundations for this thesis. The physics of calorimetry as well as the interaction and the shower development of particles in matter are summarized in chapter 1. In chapter 2, the CALICE AHCAL project is described and details on the used technologies are given.

In the second part, the time analysis of the test beam data taken with an AHCAL prototype in a tungsten absorber is presented. The experimental setup and the data preparation are described in chapter 3. A time calibration scheme for the AHCAL is developed and presented in chapter 4. Subsequently, in chapter 5 and chapter 6 the time structure of electromagnetic showers and hadronic showers are analyzed and compared to simulated predictions.

The third part of this thesis is devoted to the energy reconstruction within the AHCAL. The experimental setup and the data preparation steps are described in chapter 7. In chapter 8, correlations of shower observables with the reconstructed energy are studied. For this, hit time observables are constructed from the hit time measurements and their correlation with the reconstructed shower energy is compared to the behavior of hit energy observables and observables describing the shower geometry. In chapter 9, methods are developed on simulated data to use the time information in the energy reconstruction process for enhancing the energy resolution. It is further investigated in chapter 10 whether machine learning techniques can improve the energy resolution. An artificial neural network framework, capable of handling large amounts of features, is developed on simulated data for energy reconstruction in the AHCAL prototype and tested on test beam data.

This thesis provides work towards a better understanding of the time development of hadronic showers, its simulation and its use in the energy reconstruction of highly granular hadronic calorimeters. Furthermore, a foundation for multivariate energy reconstruction with modern machine learning algorithms in such calorimeters is laid. With the spread of CALICE technologies to other experiments (e.g., the CMS HGCal [17]), the insights gained in this thesis may have applications also outside of  $e^+e^-$ -collider experiments.

## **Part I**

# **Theoretical and Experimental Background**



# Chapter 1

## Physics Foundations

In this chapter the physics motivation and experimental foundations for this thesis are set. The scientific motivation for new collider experiments is given in the light of most recent particle physics results. The physics goals of  $e^+e^-$ -colliders are requiring a new, highly granular approach to calorimetry. In this context, the interactions of particles traversing through matter and the foundations of electromagnetic and hadronic showers are discussed as the basic principles of calorimetry.

### 1.1 Open Questions in Particle Physics

In particle physics, most interactions between fundamental particles can be predicted with high precision by the standard model of particle physics. The standard model contains spin  $1/2$  particles (fermions) as well as bosons with integer spin. The gauge bosons with spin one are the carriers of three elementary forces: the electromagnetic force (photon), the weak force ( $W$ - and  $Z$ -bosons) and the strong force (gluons). The charged fermions of the standard model are making up all visible matter. They consists of three leptons and six quarks. Three neutrinos with zero charge are completing the set of fermions. Quarks are forming composite particles, called hadrons. A hadron consisting of two quarks is called a meson (e.g., the pion) and hadrons with three quarks are called baryons (e.g., the proton).

Within the standard model, a special mechanism is needed to explain why gauge bosons have mass. The Higgs field provides this mass generating mechanism through electroweak symmetry breaking. It was proposed in 1964 together with the existence of a new spin zero boson, the Higgs boson, produced by the quantum excitation of this field [18–20]. In 2012, the Higgs boson was finally discovered at the Large Hadron Collider (LHC), completing the standard model [5, 6].

The LHC is a proton collider working at collision energies of up to 13 TeV, reaching unprecedented high energies. Besides the discovery of the Higgs boson, the experiments at the LHC are confirming the predictions of the standard model for a large range of processes

with very high precision. Figure 1.1 compiles the theory prediction and the experimental measurements of the cross-sections for various standard model processes at the ATLAS experiment. Up to now, no significant deviations from the standard model were found for these processes. Nevertheless, the standard model has several shortcomings that disqualify it for a *theory of everything*. These include:

- It cannot explain gravity, one of the fundamental forces.
- It cannot explain the amount of matter/antimatter asymmetry observed in the universe
- It cannot explain the observed dark matter making up about 85 % of the matter in the universe.

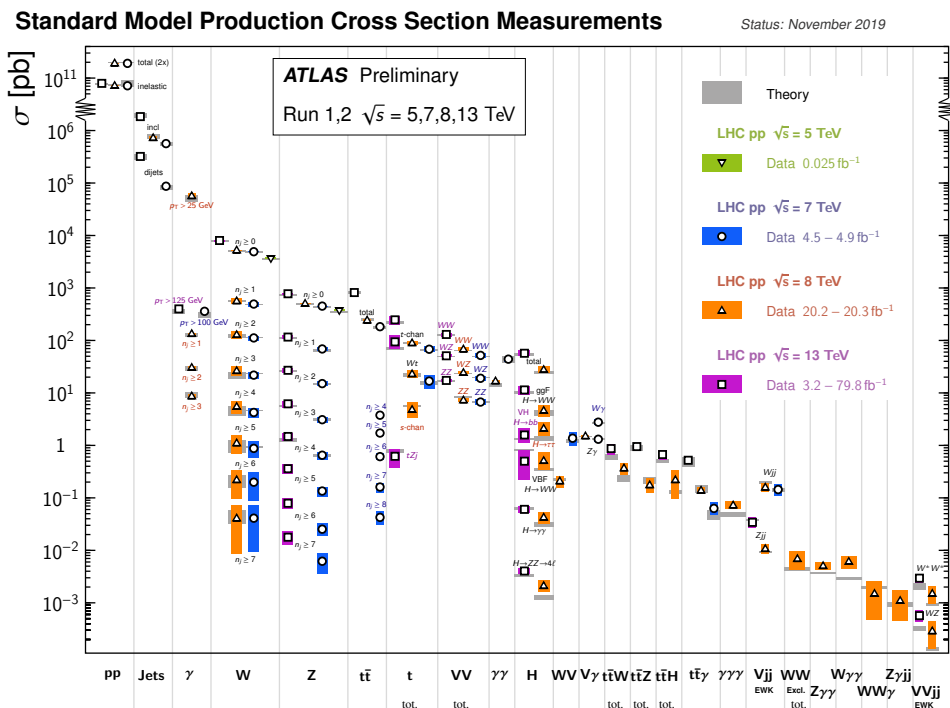


**Figure 1.1** – Theory predictions and experimental measurements of various standard model processes at the ATLAS experiment [21].

The above listed shortcomings motivate the extension of the standard model by new theories. These theories beyond the standard model often predict either new particles that may be observed at collider experiments or small deviations in known standard model processes. The effort to search for physics beyond the standard model can be broadly grouped into three categories. First, cosmological experiments offer a window to observations at very large scales that are including gravity (e.g., the observation of dark matter), but also at very early times of the universe such as the precise measurement of the cosmic microwave background. Second, collider based experiments at the energy frontier, as the LHC, are

aiming at the direct production of new particles at very high energies. Various models (e.g., supersymmetry) are predicting new particles at the TeV scale, which were not detected up to now.

The third way of searching for physics beyond the standard model are precision measurements of standard model processes. There is a wide range of existing or proposed precision experiments. One famous example is the  $g-2$  experiment at Fermilab [22] which aims at measuring the muon anomalous magnetic moment with a precision of 0.14 per million. This requires an interplay of precise theoretical calculations of the standard model prediction and precision measurements.

Besides the key role of collider based experiments for the discovery of new particles, they are also an important tool for precision measurements. For collider based precision measurement,  $e^+e^-$  colliders are often advantageous compared to  $pp$ -colliders. The proton is a composite particle consisting of quarks and gluons (called partons), with the strong force dominating the interactions. Electrons and positrons on the contrary are fundamental particles interacting with each other via the electroweak force. Therefore, the initial state of the two colliding particles is well known for  $e^+e^-$ -collisions, while in  $pp$ -collisions the energy distribution of the interacting partons of the two colliding protons follows a parton distribution function (PDF), leading to large uncertainties in the invariant mass of a collision. Additionally, so called *underlying events* may arise in  $pp$ -collisions forming secondary collisions besides the main, high energetic collisions. Compared to the large cross-sections for the strong interactions, many interesting processes (e.g., the production of Higgs bosons via higgsstrahlung, or vector boson fusion) are mediated by the electroweak force. This leads to a large hadronic background.

A prominent example of a precision  $e^+e^-$ -collider experiment is the Belle II experiment at the SuperKEKB accelerator [23]. The Belle II experiment is investigating the nature of the matter/antimatter asymmetry in  $B$ -meson decays. For this, the SuperKEKB accelerator is designed for producing  $B$ -mesons in large quantities.

With no new physics showing up at the LHC, precision measurements of the Higgs boson are one of the main focusses of the high energy particle physics community. Probing the exact nature of the Higgs boson may lead to conclusions reaching to far higher energy scales than the Higgs boson's rest mass. Until now, no  $e^+e^-$ -collider exists that can reach energies for the production of Higgs bosons. In the next section, the physics case for future  $e^+e^-$ -collider experiments reaching to these high energies is discussed and several proposed options are presented.

## 1.2 Future $e^+e^-$ -Collider Concepts

Experiments at  $e^+e^-$ -colliders offer the opportunity to measure particle interactions without a large hadronic background and with a well-defined initial state. This leads to several beneficial consequences for precision measurements compared to proton-proton collider experiments. Currently, there are several concepts discussed for possible future  $e^+e^-$ -colliders. In this section, the most important physics goals of such experiments will be discussed, followed by an introduction to several concepts for potential future  $e^+e^-$ -colliders.

### 1.2.1 Physics Goals

After the discovery of the Higgs boson, measuring its properties with high precision has become a special interest in particle physics. As the Higgs boson interacts with all massive particles of the standard model, it is likely to be a key to many of the open questions in particle physics. Hints about the exact nature of the Higgs sector can be inferred by precision measurements of the Higgs boson's coupling constants to other standard model particles. Additional, undiscovered Higgs bosons, or a composite nature of the Higgs boson are expected to result in deviations of those coupling constants compared to the standard model predictions.

The cross-sections for different Higgs production channels at  $e^+e^-$  colliders are shown in fig. 1.2. For the production of the Higgs boson, a center of mass energy of approximately  $\sqrt{s} = 250\text{ GeV}$  is necessary.

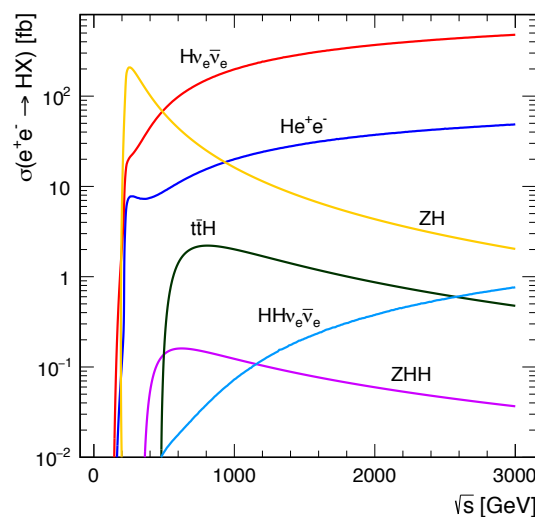


**Figure 1.2** – Higgs production cross sections in  $e^+e^-$  collisions for several processes [9].

### Higgs Factory at 250 GeV

At center of mass energies around  $\sqrt{s} = 250 \text{ GeV}$  the Higgs production cross-sections for the  $e^+e^- \rightarrow HZ$  process, also called *Higgsstrahlung*, reaches a maximum (see fig. 1.2). It is expected that the measurement of most of the coupling constants of the Higgs boson will achieve a precision of the order of 1 % at such an  $e^+e^-$ -collider.

The Higgsstrahlung production mechanism is of special interest for  $e^+e^-$ -collider experiments. As there are only four particles directly involved in this process and the initial  $e^+e^-$  state is known, properties of the Higgs boson can be inferred by measuring the  $Z$ -boson. This is done using the leptonic decay channels of the  $Z$ -boson into  $e^+e^-$ -pairs and  $\mu^+\mu^-$ -pairs. When the momentum of the two leptons is denoted with  $\mathbf{p}_{l^\pm}$  and their energy with  $E_{l^\pm}$ , the Higgs recoil mass  $M_{\text{recoil}}$  can be calculated as [24]:

$$M_{\text{recoil}}^2 = (\sqrt{s} - E_{l^+} - E_{l^-})^2 - |\mathbf{p}_{l^+} + \mathbf{p}_{l^-}|^2. \quad (1.1)$$

It should be noted that this measurement of the Higgs mass is completely model independent, as no assumptions about the Higgs boson have to be made. Instead, only the initial state and the decay products of the  $Z$ -boson have to be measured.

Besides a precise measurement of the the Higgs boson's mass, this technique allows the measurement of the total decay width of the Higgs boson, a measure from which invisible decays, e.g., decays into dark matter candidates, may be detected. With the  $Z$  recoil measurement, the cross-section  $\sigma(e^+e^- \rightarrow Zh)$  can be measured with high precision without explicitly measuring the Higgs itself. The total width of the Higgs boson  $\Gamma_{\text{tot}}$  can be calculated by [25]:

$$\Gamma_{\text{tot}} = \frac{\Gamma(h \rightarrow ZZ)}{\text{BR}(h \rightarrow ZZ)}, \quad (1.2)$$

where  $\Gamma(h \rightarrow ZZ)$  is the width of the  $h \rightarrow ZZ$  decay, which is proportional to  $\sigma(e^+e^- \rightarrow Zh)$ . The branching ratio  $\text{BR}(h \rightarrow ZZ)$  can be directly determined with the  $Z$  recoil measurement, by comparing the total number of  $Z$  bosons recoiling against the Higgs boson with the number of those Higgs bosons decaying into two  $Z$  bosons. At higher energies, other combinations of decay and production processes may provide more statistics and a more precise measurement of the Higgs' total decay width, following a similar logic with the Higgsstrahlung process as the key to model independent measurements.

### Top Quark Threshold and Above

The top quark is the heaviest of all standard model particles with a mass of  $m_t \approx 175 \text{ GeV}$ . Therefore it has the largest coupling to the Higgs boson (called *top Yukawa coupling*), which is expected to be close to unity and a key for our understanding of electroweak symmetry breaking. Together with the mass of the Higgs boson, the top quark's mass plays a crucial role

in probing the vacuum stability of the standard model. The top quark decays too fast to form bound states, which leads to the unique behaviour of a production threshold at energies around  $2m_t$  ( $\sqrt{s} \approx 350 \text{ GeV}$ ). A  $e^+e^-$ -collider offers the possibility to scan the threshold region of the top quark allowing for precise measurements of the top quark's mass [26].

At center of mass energies of  $\sqrt{s} = 500 \text{ GeV}$ , the production of two Higgs bosons becomes accessible. The process  $e^+e^- \rightarrow ZHH$  allows to measure the self-coupling of the Higgs boson, which has until now not yet been observed at the LHC and which holds large potential for deviations from the standard model prediction due to new physics [27]. Additionally, the top quark coupling to the Higgs can be measured at these energies via the  $e^+e^- \rightarrow t\bar{t}H$  process. At even higher energies of several TeV the production cross section for Higgs production via the  $e^+e^- \rightarrow H\nu_e\bar{\nu}_e$  are rising providing more statistics allowing for more precise measurements. Additionally, the double Higgs production can be measured via  $e^+e^- \rightarrow HH\nu_e\bar{\nu}_e$ . This process is complementary to the above mentioned  $e^+e^- \rightarrow ZHH$  process, as it has a different sensitivity to the Higgs self coupling constant and a different energy dependence.

### 1.2.2 Proposed Concepts for Future $e^+e^-$ -Colliders

Several proposals for  $e^+e^-$ -colliders are currently discussed in the community. These proposals can be grouped into two classes: circular and linear colliders. Circular  $e^+e^-$ -colliders, such as the FCC-ee [10] or CEPC [28], suffer greatly from synchrotron radiation. The power loss due to synchrotron radiation scales with high powers of the beam-particle's energy  $E$ , the particle's mass  $m$  and the radius of the accelerator  $r$ :  $P_{\text{sync}} \propto \frac{E^4}{r^2 m^4}$ . Because of the low mass of electrons, the power loss due to synchrotron radiation is the limiting factor for circular  $e^+e^-$ -colliders. Thus, they need to be of large circumference and are limited in energy usually to the Higgs factory scale or the top quark threshold. The FCC-ee accelerator, for example, is proposing a maximum collision energy of  $\sqrt{s} = 365 \text{ GeV}$  with an accelerator ring of about 100 km circumference. At these energies, however, circular colliders may reach higher luminosities compared to linear colliders. An additional benefit of circular colliders over linear colliders is the possibility of reusing the ring for a future high energy proton-proton collider.

Linear colliders are not limited by the power loss of synchrotron radiation, which allows them to reach higher energies. The linear geometry, however, has the disadvantage that particle bunches are lost after the collisions, while they can be reused in circular colliders. This makes it challenging for linear colliders at high energies to reach high luminosities. Very high focussing of the particle bunches at the interaction point is necessary, as well as the use of damping rings for reducing the beam emittance.

Current concepts for linear  $e^+e^-$ -colliders include the International Linear Collider (ILC) [8] and the Compact Linear Collider (CLIC) [9]. These two proposals are relying on different accelerator technologies and are thus facing slightly different challenges. For the ILC a staging approach starting at center of mass energies of 250 GeV with the possibility to upgrade to 380 GeV and 500 GeV is foreseen. CLIC could reach to even higher energies of up to 3 TeV.

A big advantage of  $e^+e^-$ -collider experiments are clean events without a large hadronic background. This allows the precise measurement of hadronic final states, which is especially important for the Higgs boson as it decays dominantly hadronically (mostly via  $H \rightarrow b\bar{b}$ ). Additionally, also the  $W$ - and  $Z$ -bosons decay to more than  $2/3$  hadronically. As these bosons are involved in many final states, an excellent jet energy resolution is important for all  $e^+e^-$ -collider experiments. All proposals of  $e^+e^-$ -collider experiments aim for a distinction between the hadronic decay of the  $W$ - and the  $Z$ -boson at the 95% level. This requires a jet energy resolution of 3 to 4% at 100 GeV. The jet energy resolution is usually limited by the performance of the calorimeters. Before discussing a modern detector layout capable of achieving the jet energy resolution requirements, the fundamental physics processes involved in calorimetry are discussed in the next section.

### 1.3 Interaction of Particles with Matter

In any particle physics experiment, the detection of particles is of high importance. Every particle detector relies on fundamental interaction processes of particles with matter. In this section the most important interactions are discussed, specifically focussing on processes relevant in calorimeter applications. Most content of this section is summarized from [29–31].

#### 1.3.1 Electromagnetic Interactions of Charged Particles with Matter

All charged particles may interact electromagnetically with the traversed medium. These electromagnetic processes are the dominating interactions of electrons, muons and photons with matter. Ionization and Bremsstrahlung are the most prominent electromagnetic interaction processes. They are described in detail in the following.

##### Excitation and Ionization

Charged particles traversing matter may excite and ionize the atoms of the passed material via electromagnetic interactions. While excitation refers to processes where electrons are excited from their initial states to higher discrete bound states, ionization refers to the transition of a bound electron to a state where the electron is no longer bound. The expected energy loss per unit path ( $dE/dx$ ) for these electromagnetic processes of massive charged particles with velocity  $v = \beta c$ , charge  $z$  and a rest mass much larger than the electron mass  $m_e$ , can be approximated using the *Bethe formula*:

$$-\left(\frac{dE}{dx}\right)_{\text{ioniz.}} = \frac{M(n) z^2}{\beta^2} \left[ \ln\left(\frac{2m_e c^2}{I} \frac{\beta^2}{(1-\beta^2)}\right) - 2\beta^2 \right]. \quad (1.3)$$

The material constant  $M(n)$  is only depending on the electron density of the material ( $n$  in  $\text{cm}^3$ ) and  $I$  is the mean excitation potential of the traversed medium. Corrections to the approximation of the Bethe formula include a shell correction term  $U$  and a density

correction term  $\delta$  (see also [29]). At higher energies above  $\beta\gamma = 1000$  radiative corrections become important. The Bethe formula reaches a minimum for relativistic energies around  $\beta \approx 0.95$ , or  $\beta\gamma \approx 3 - 4$  (see fig. 1.3 (left)). Particles at this energy-loss minimum are called *minimum ionizing particles (MIPs)*. Note that the minimum of the Bethe formula is only dependent on the material with regards to the mean excitation potential  $I$  which can be approximated by  $I \approx 10 \text{ eV} \cdot Z$  with  $Z$  being the charge of the nuclei in the traversed material. Particles with the MIP property serve as an important standard candle for measuring particle energy depositions via ionization in particle detectors. For high energies, the free electrons from the ionized atoms ( $\delta$ -rays) get significant amounts of kinetic energy and may in turn also ionize the material or even escape out of the absorber.

To approximate the energy loss of a charged particle in matter, the process can be treated as a series of independent successive events. For a thin absorber, the probability density distribution of the energy loss can be parametrized as a *Landau* distribution. For thicker absorbers, the probability distribution function becomes gaussian. The characteristic long tail to high energy losses of the Landau distribution is mainly due to fast secondary electrons.

For electrons and positrons eq. (1.3) does not hold because of the equality of the rest masses of the traversing and the excited electrons. In order to accurately describe the collision loss of electrons, a separate treatment is necessary (*Berger-Seltzer equation* [32]). The difference between the energy loss of electrons compared to more massive particles with charge  $z = 1$  decreases for higher energies.

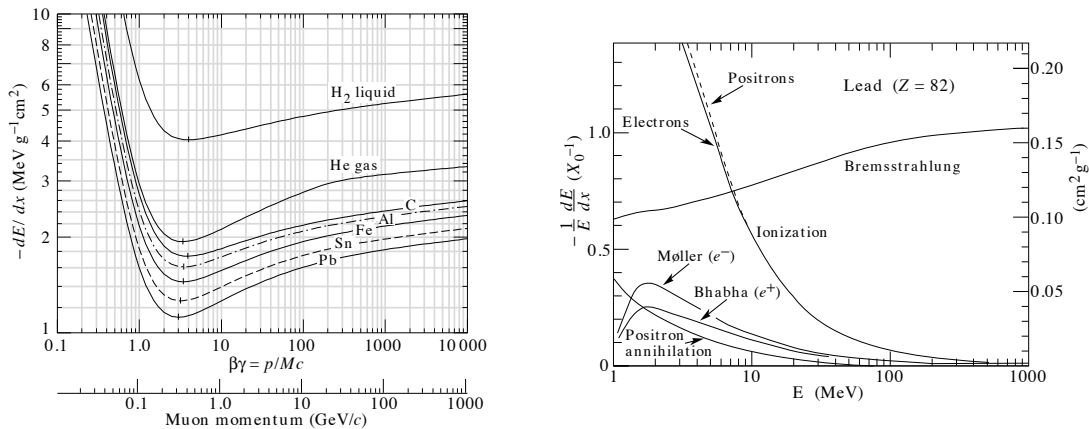


**Figure 1.3** – *Left*: Mean energy loss rate of charged particles via ionization in different materials. The characteristic minimum is clearly visible and relatively stable across different materials. *Right*: Energy loss contributions of different processes for electrons and positrons in lead. Both figures are taken from [33].

### Bremsstrahlung

Charged particles may lose energy by radiating a photon in the coulomb field of the nuclei of the traversed medium. This process is called *bremsstrahlung*. The energy loss per unit length

for a particle with charge  $z$ , rest mass  $m$  and energy  $E$  behaves as:

$$-\left(\frac{dE}{dx}\right)_{\text{brems.}} \propto \frac{z^2 E}{m^2}. \quad (1.4)$$

The energy loss due to bremsstrahlung is inversely proportional to the quadratic mass of the incoming particle and is thus most important for light particles such as electrons and positrons. Opposed to losses due to ionization, radiation losses scale linearly with energy. This indicates an increasing relevance of radiation loss at higher energies. Compared to electrons, ionization remains the main energy loss for the 200 times heavier muons for a wide range of energies up to several 100 GeV.

The proportionality factor between the energy  $E$  of an incoming electron and the mean radiation energy loss defines the *radiation length*  $X_0$  of the traversed material:

$$-\left(\frac{dE}{dx}\right)_{\text{brems.}} = \frac{E}{X_0}, \quad (1.5)$$

where the radiation length is material dependent (atomic number  $Z$ , atomic weight  $A$ ) and can be approximated as:

$$X_0 = \frac{716.4 \cdot A [\text{gmol}^{-1}]}{Z(Z+1) \ln(287/\sqrt{Z})} \text{ g cm}^{-2}. \quad (1.6)$$

The radiation length may differ significantly between different materials (e.g. iron:  $X_0 = 17.6$  mm, tungsten:  $X_0 = 3.5$  mm, or polystyrene  $X_0 = 424$  mm) The energy of incoming electrons where the radiation loss is larger than the ionization loss is called the critical energy  $E_c$ . It can be approximated for solid materials:

$$E_c = \frac{610 \text{ MeV}}{Z + 1.24}. \quad (1.7)$$

### Cherenkov Light

When charged particles with velocity  $v$  traverse a medium with refractive index  $n$  faster than the speed of light in that medium  $\frac{c}{n}$  Cherenkov light will be emitted. This effect results from the fact that a traversing charged particle polarizes the medium around its trajectory. For  $v < \frac{c}{n}$  the dipoles of the polarized atoms are arranged symmetrically and the dipole field integrated over all dipoles vanishes. For  $v > \frac{c}{n}$  the dipoles arrange in an asymmetric way and the resulting dipole field leads to the emission of Cherenkov light under a characteristic angle. This threshold effect can be used for particle identification purposes (Cherenkov counter). The total energy loss by Cherenkov radiation is usually much lower than the ionization loss (approximately 1 % for minimum ionizing particles).

### Additional Processes

In addition to ionization and radiation, charged particles may lose energy via virtual photons by the direct production of  $e^+e^-$ -pairs, or photonuclear interactions. These processes get increasingly relevant at high energies. For electrons and positrons Moeller-scattering, Bhabha-scattering and positron annihilation may play minor roles at energies below 100 MeV. The energy loss contributions for electrons in lead absorber are shown in fig. 1.3 (*right*).

### 1.3.2 Electromagnetic Interactions of Photons with Matter

For the interaction of photons with matter three processes are most important:

- **Photoelectric effect:** Complete absorption of the photon by the atomic electron cloud of the atoms.
- **Compton scattering:** Scattering of the photon on quasi-free electrons.
- **Pair production:** creation of  $e^+e^-$  pairs in the coulomb field of an electron or a nucleus.

The photoelectric effect dominates at low photon energies below 50 keV - 500 keV. For photon energies of several MeV the pair production process is dominating. In between, the largest contribution is due to Compton scattering. Unlike charged particles, the photon gets absorbed as soon as it interacts with the medium. This leads to an exponential reduction in intensity of any incoming photon beam with initial intensity  $I_0$ :

$$I = I_0 e^{-\mu x}, \quad (1.8)$$

where  $x$  is the thickness of the traversed medium and  $\mu$  is the mass attenuation coefficient depending on the cross sections of the various absorption processes in the given material. The mean free path of high energetic photons is related to the radiation length as  $\frac{7}{9} X_0$ .

### 1.3.3 Nuclear Interactions of Hadrons with Matter

Charged particles may interact with the electrons of the traversed matter in an electromagnetic way as described above. Additionally, hadrons interact with the nuclei of the traversed medium by interactions via the strong force. For neutral hadrons nuclear interactions are the only possibility of energy loss. In general, the number of processes involved in hadronic interactions with matter is much larger than the ones described for electromagnetic interactions, leading to a more complex behavior. In the following the process of nuclear spallation and the interactions of neutrons with matter are discussed.

### Nuclear Spallation

A nucleus interacting with an incoming hadron will most likely undergo spallation. The incoming hadron interacts with the quasi-free nucleons, which in turn may travel through the nucleus and collide with additional nucleons. Part of these nucleons may get enough energy to escape from the nucleus, while others lead to excited states of the nucleus. The number of protons and neutrons released in the fast spallation process is on average the ratio of protons and neutrons in the target nuclei. The escaping particles may form pions or other unstable hadrons in cases where the transferred energy is high enough.

On a slower time scale, excited nuclei de-excite by evaporating neutrons, protons, or heavier hadrons such as  $\alpha$ -particles, the vast majority of which are usually neutrons. The excess energy of the nucleus is radiated via photons. Several hundred of different processes may occur during a spallation process with similar probability, thus leading to a large diversity in the outcome of a nuclear interaction. The large number of spallation products may themselves interact with the absorber material leading to a hadronic shower. The spallation process is schematically illustrated in fig. 1.4 (*left*).

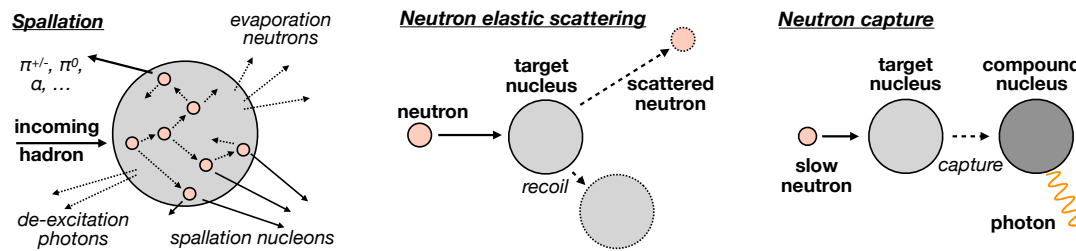


**Figure 1.4** – Hadronic interactions in matter. *Left:* Spallation of a nucleus by an incoming hadron. *Middle:* Neutron elastic scattering. *Right:* Neutron capture.

### Interactions of Neutrons with Matter

Neutrons differ in their interactions considerably compared to charged particles, because they may only interact hadronically with the traversed medium. Neutrons may lose their kinetic energy via three key processes (see also [34]):

- **Elastic neutron scattering:** Elastic scattering (illustrated in fig. 1.4 *middle*) is usually the dominant interaction for neutrons with energies between 1 eV and 1 MeV. The maximum energy fraction lost by neutrons scattering elastically on nuclei (atomic mass  $A$ ) for each collision is given by the kinematic limit for central collisions:

$$E_{\text{loss,max}} = \frac{4A}{(A+1)^2} \cdot \quad (1.9)$$

Thus, the full energy of the neutron can be transferred to a hydrogen nucleus by a single collision with an average loss of energy of 50 %. For heavier nuclei the fractional

average energy loss drops rapidly being only 3.4 % per collision for iron.

- **Neutron capture:** Neutrons that have lost nearly all of their kinetic energy may be captured by the absorber's nuclei. During this process, binding energy of the (now heavier) nucleon gets released usually by the emission of photons. If the captured neutron was first released via evaporation, the binding energy lost during the evaporation process (which is lost for calorimetric purposes) is gained back during the capture process. The neutron capture process is illustrated in fig. 1.4 (*right*).
- **Inelastic neutron scattering:** Besides nuclear spallation at higher neutron energies, neutrons may lose energy via inelastic scattering by exciting the target material's nuclei. This process usually becomes relevant for neutron energies above a few MeV, but is largely material dependent. The excited nuclei further de-excite by emitting photons.

During the spallation process discussed above, many neutrons may be evaporated. The kinetic energy of these evaporated particles in the spallation process is Maxwell-Boltzmann distributed and on average about 3 MeV [34]. If the energy of these neutrons is higher than the binding energy of the material they are interacting with, they may themselves induce a spallation process. However, the kinetic energy distribution of evaporation neutrons favours elastic neutron scattering.

## 1.4 Calorimetry

A calorimeter is an important part of most high energy particle detector systems. It is used to measure the energy of particles in a destructive way by absorbing all of the particle's energy. In this section, the basic operating principles of a calorimeter, as well as the process of the energy measurement and sources of uncertainty are discussed.

When passing through matter, a high energy incoming particle may interact with the medium in several ways, thereby leading to the generation of an electromagnetic or hadronic shower, depending on the nature of these particles (details about the shower development are provided in section 1.4.2 and section 1.4.3). During the shower process, the kinetic energy of the incoming particle is transformed in several ways, e.g. into the generation of fast secondary particles, excitation of atoms, radiation of photons, heat generation, or the loss of binding energy due to spallation. Traditionally, a calorimeter is used to infer the energy produced by a chemical reaction by measuring the produced heat. In particle physics calorimeters, measuring the energy of particles and radiation via the production of heat exists as well [35]. Despite their success at low energy precision measurements, these types of calorimeters are not applicable for high energetic particles. Large detector volumes are necessary to fully contain the showers generated by such particles and the generated heat is too low to be measured. Thus, a high energy calorimeter needs to rely on other detection

mechanisms. One of the most common detection mechanisms is to measure the ionization energy of charged particles in a shower.

Calorimeters can be distinguished into two categories: *homogenous calorimeters* and *sampling calorimeters*. In a homogeneous calorimeter, the whole calorimeter serves as the active component and the complete shower can be measured. One of the most famous modern homogenous calorimeters is the Compact Muon Solenoid (CMS) electromagnetic lead tungstate crystal calorimeter [36]. Usually, the active material in a homogeneous calorimeter is of low density leading to very large detector geometries to fully absorb the incoming particles. When high density active materials are used, the calorimeter becomes very expensive, as is the case for the CMS calorimeter. For a more cost efficient detector design, the calorimeter is often build as a *sampling calorimeter*. In a sampling calorimeter, active materials and absorber materials are organized in an alternating layer structure. Here, the absorber material is usually of high density and is not instrumented. Thus, the shower is *sampled*, i.e., the energy depositions of the shower constituents can only be measured at certain points. An important property of a sampling calorimeter is the sampling fraction  $F_{\text{sample}}$  defined as the fraction of energy that a minimum ionizing particle deposits in the active materials of the calorimeter  $E_{\text{dep., active}}^{\text{mip}}$  with respect to the total energy deposited in the calorimeter  $E_{\text{dep., active}}^{\text{mip}} + E_{\text{dep., absorber}}^{\text{mip}}$ :

$$F_{\text{sample}} = \frac{E_{\text{dep., active}}^{\text{mip}}}{E_{\text{dep., active}}^{\text{mip}} + E_{\text{dep., absorber}}^{\text{mip}}} \quad (1.10)$$

Because of the different length scales of electromagnetic and hadronic showers, two types of calorimeters are used in high energy physics multi purpose detectors: an electromagnetic calorimeter and a hadronic calorimeter, each employing different technologies optimized for the specific shower type. Because of the smaller size of electromagnetic showers, the electromagnetic calorimeter is commonly placed in front of the hadronic calorimeter and consists of a higher granularity and sampling fraction. Scintillators are often used as an active material for a calorimeter, where the deposited energy of the shower particles is measured via scintillation light. Before discussing the development of electromagnetic and hadronic showers in a calorimeter, the scintillation mechanism is described in the next section.

### 1.4.1 Scintillators

When traversing matter, charged particles may excite the surrounding atoms and molecules into unstable states. These excited states usually decay quickly under the emission of photons (*scintillation*). For transparent materials, the generated light can be collected, measured and thus be used as a detection mechanism for charged particles. A wide variety of different scintillators in gaseous, liquid and solid form exist. Two types of scintillators exist: organic and inorganic scintillators. While inorganic scintillators typically have a high light output,

but suffer from long decay times, organic scintillators are much faster, in turn having lower light outputs. The instruments discussed in this thesis are based on organic scintillators, and thus are the focus of this section.

Polystyrene is an example of an organic scintillator. It consists of long hydrocarbon chains with benzene structures ( $C_6H_6$ ). The scintillation process is visualized in fig. 1.5 (*left*). The energy states of the molecules are organized in singlet states  $S_i$  and triplet states  $T_i$ . A charged particle traversing the scintillator may excite an electron from the ground state  $S_0$  to a higher state. The substructure of the higher energy levels is originating from vibrational modes of the molecule. The excited states tend to decay internally (within tens of ps), without the emission of photons, to the  $S_1$  state, from where they decay under emission of a photon to one of the vibrational states of  $S_0$ . The scintillator is self transparent because the photon emitted by the transition from  $S_1$  to one of the vibrational states of  $S_0$  is less than what would be needed to excite an electron from the non-vibrant  $S_0$  state to the  $S_1$  state. The transition between the  $S_1$  and  $S_0$  state is the fast component of the luminescence (typically up to a few ns). A slower component is due to transitions to the triplet states  $T_i$ . These transitions are suppressed by spin conservation, but may occur by a process called intersystem crossing. As the de-excitation process from the  $T_1$  to the ground state is again suppressed by spin conservation, this process occurs only on much longer time scales (up to seconds) and is known as *phosphorescence*.

For plastic scintillators, e.g., polystyrene, two additional materials may be added: a primary and a secondary fluor. The primary fluor is added in relatively high concentrations in the order of  $\mathcal{O}(1\%)$ . This assures a highly efficient coupling of the base plastic material to the primary fluor via dipole-dipole interactions (called Förster energy transfer). The primary fluor emits a photon which is shifted from the initial UV regime to a larger wavelength. Additionally, the primary fluor often reduces the decay time of the scintillator considerably. The secondary fluor acts as an additional wavelength shifter, increasing the emitted photons wavelength to the blue range of the visible light spectrum where usually photon detectors work more efficiently than for UV light. The absorption and radiation chain is illustrated in fig. 1.5 (*right*).

### Scintillator Saturation

In first order, the light output per unit length of the track of an ionizing particle ( $\frac{dL}{dx}$ ) in a scintillator is proportional to the energy loss of the traversing particle ( $\frac{dE}{dx}$ ). For high energy losses, however, this is not true and a saturation effect of the scintillation light is observed (see fig. 1.6). This effect can be parametrized and is known as Birks' law [39]:

$$\frac{dL}{dx} = L_0 \frac{dE/dx}{1 + k_B dE/dx}. \quad (1.11)$$

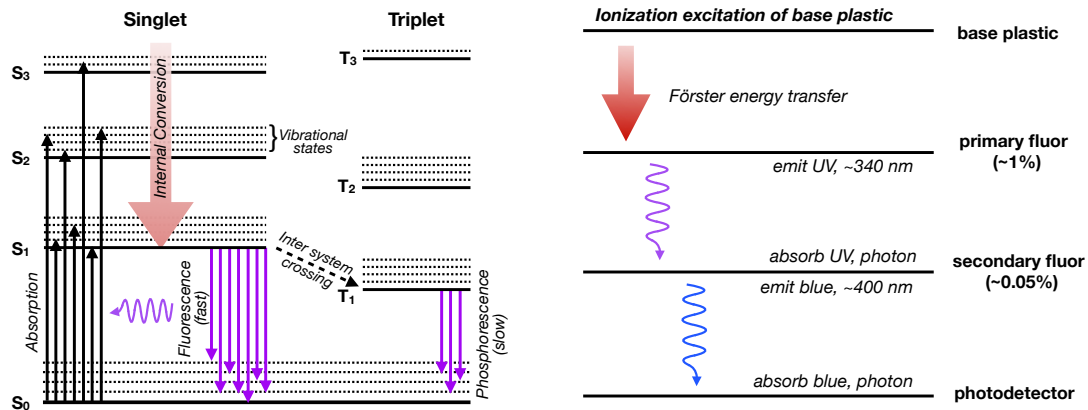


**Figure 1.5** – (Left: Schematic drawing of the scintillation mechanism via excitation of the  $S_0$  ground state and emission of a photon. Adapted from [37]. Right: Absorption and radiation scheme in a plastic scintillator. Adapted from [38]

Here,  $L_0$  is the light output for low energy densities and  $k_B$  is called Birks' constant which has to be determined for each scintillator material experimentally. The effect of scintillator saturation is more pronounced for hadronic showers than for electromagnetic ones. Even though electromagnetic showers are more dense, the  $\frac{dE}{dx}$  energy deposition of single electrons is generally very low for most electron energies. Only for low energetic electrons the energy depositions ( $< 100$  keV) get large enough to be affected by saturation. At these energies the electrons have already lost most of their energy and thus the overall effect on the electromagnetic shower is small. For hadronic showers a large amount of energy is deposited by particles, including nuclear fragments and protons, with relatively high  $\frac{dE}{dx}$  values. They are thus much more affected by scintillator saturation. More details about the differences of the development of electromagnetic and hadronic showers are given in the next section.

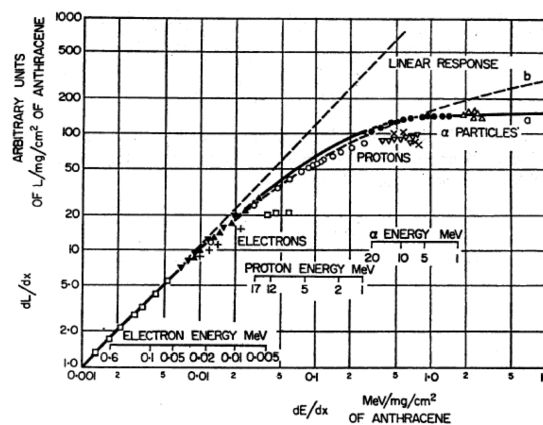


**Figure 1.6** – The effect of scintillator saturation: Production of scintillation light in anthracene for different particles. A clear saturation behaviour can be observed for higher energy densities. Figure taken from [37].

### 1.4.2 Electromagnetic Shower Development

At high energies, the dominant energy loss for electrons in matter is the emission of photons via bremsstrahlung. These photons in turn may have high energies that could lead to  $e^+e^-$  pair-production, thus doubling the particle count. For consecutive bremsstrahlung and pair-production processes an electromagnetic cascade forms. If the energy of a shower particle falls below the minimum energy allowing for pair-production, no new  $e^+e^-$  pairs are created. The increase in the number of shower constituents slows down and the shower is ending when all participating particles have lost their energy.

The characteristic longitudinal scale of an electromagnetic shower is given by the radiation length  $X_0$  which heavily depends on the material. The radial size of an electromagnetic shower can be effectively described by the *Molière radius*:

$$\rho_M = X_0 \frac{21.2 \text{ MeV}}{E_c}, \quad (1.12)$$

with  $E_c$  being the critical energy (eq. (1.7)). A cylinder with that radius around the central shower axis contains on average 90 % of the shower energy. As the electromagnetic shower is an exponential process (each pair-production process doubles the particle count) the depth of the shower in longitudinal direction scales logarithmically with the energy of the incoming particle.

### 1.4.3 Hadronic Shower Development

As pointed out above, hadrons traversing a thick absorber are likely to interact with the nuclei of the traversed medium via spallation. In the spallation process secondary particles are produced that may in turn produce additional particles themselves, thereby forming a hadronic shower. The processes happening in a hadronic shower are schematically depicted in fig. 1.7. This section discusses key properties of hadronic showers.

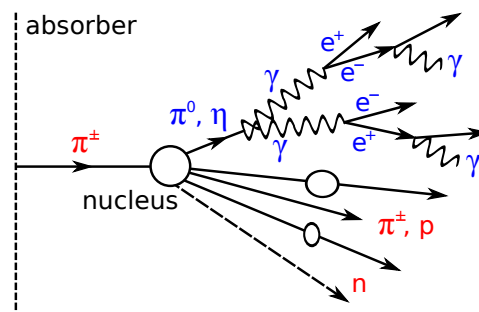


**Figure 1.7** – Development of a hadronic shower. Taken from [40].

### Electromagnetic Fraction

Among the generated secondary particles within a hadronic shower pions typically represent a large fraction. The charged pions decay via the weak force into charged leptons and the corresponding neutrinos (e.g.,  $\pi^+ \rightarrow \mu^+ \nu_\mu$ ) with a lifetime of 26 ns, allowing them to travel themselves in the medium, to interact with it and to eventually produce more hadrons before decaying. The neutral pions (and the  $\eta$  meson) decay via the electromagnetic force most likely into two photons ( $\pi^0 \rightarrow \gamma\gamma$ ) with a much shorter lifetime of  $8.4 \times 10^{-17}$  s and no further hadronic interactions prior to the decay. The photons further create  $e^+e^-$ -pairs, thus producing an electromagnetic sub-shower. The electromagnetic fraction  $f_{\text{em}}$  of a hadronic shower with initial energy  $E$  can be parameterized as follows:

$$f_{\text{em}} = 1 - \left( \frac{E}{E_0} \right)^{(k-1)}, \quad (1.13)$$

where  $k$  and  $E_0$  are material dependent constants. Typically values are  $k \approx 0.8$  and  $E_0 \approx 1$  GeV. The electromagnetic fraction increases with the energy of the incoming particle. For 10 GeV hadrons, the electromagnetic fraction is usually  $f_{\text{em}} \approx 30\%$  and for 100 GeV  $f_{\text{em}} \approx 50\%$  for commonly used heavy absorber materials (e.g., in lead [41]).

Baryon induced showers, such as a hadronic shower originating from a proton, are expected to have a slightly smaller electromagnetic fraction compared to a meson induced shower. Because of baryon number conservation, an incoming baryon is more likely to produce baryons. This reduces the number of  $\pi_0$  generated in the first steps of the shower.

### Invisible Energy

During the spallation process, significant amounts of neutrons and protons are released from the absorber nucleus. Part of the kinetic energy of the interacting particle is necessary to lift these nucleons out of the potential well of the nucleus (binding energy). This energy goes into the transformation of the absorber nucleus into one with a smaller atomic mass. This process cannot be measured directly and this so called *invisible energy* is lost for calorimetric purposes. In iron, the nuclear binding energy loss is about 16 % of the hadronic component [31].

The mean free path of a 1 MeV neutron in a lead absorber is 6 cm [31]. Thus, the neutrons may travel large distances in the calorimeter before interacting with the material. Eventually the neutrons are captured by a different nucleus and the binding energy can be gained back and measured via the radiation of photons. The neutron capture processes happen at long timescales up to several micro seconds after the initial collision and thus, they can only be measured for very long integration times and at large distances from the shower axis.

Besides the loss in binding energy the kinetic energy of recoil nuclei is an important source of invisible energy. On average it may contribute about 5 % to the overall hadronic component of a shower in an iron absorber [31]. Smaller contributions to invisible energy

may be due to neutrinos or muons, produced in pion or kaon decays, escaping the calorimeter. It is important to note that the phenomenon of invisible energy is occurring only in hadronic interactions. Therefore, due to the energy lost in the hadronic component, hadronic showers give a lower response in most calorimeters compared to electromagnetic showers of the same initial energy.

### Hadronic Shower Profiles

The longitudinal length scale of a hadronic shower is the nuclear interaction length  $\lambda_{\text{int}}$ . It is defined as the average distance a high energy hadron may travel within a given material before any nuclear interaction. The nuclear interaction length depends strongly on the absorber material. It is smaller for high density, high  $Z$  materials such as tungsten ( $\lambda_{\text{int}} = 96 \text{ mm}$ ) or iron ( $\lambda_{\text{int}} = 168 \text{ mm}$ ) and larger for low density materials as polystyrene ( $\lambda_{\text{int}} = 795 \text{ mm}$ ). However, the material dependence in the nuclear interaction length is not as large as for the radiation length  $X_0$ . In general, the nuclear interaction length is larger than the radiation length, leading to the fact that electromagnetic showers are starting on average earlier in an absorber material and are more compact in longitudinal direction.

Besides the longer length scales in longitudinal direction, hadronic showers also extend much larger in radial direction compared to electromagnetic showers of the same energy. A hadronic shower has a narrow core dominated by the electromagnetic sub-shower, where the radial size is defined by the Molière radius, and an outer part governed by the hadronic part of the shower. The isotropy of the spallation process leads to larger radial extent. Additionally, slow neutrons may travel long distances in all directions in the absorber before being captured.

#### 1.4.4 Fluctuations

The processes happening in a shower are subject to large event-to-event fluctuations, especially for hadronic showers. These fluctuations are the main source for the energy resolution of a calorimeter. Several different types of fluctuations are discussed in the following. Most of this section is summarized from [31].

#### Signal Quantum Fluctuations

Every detector with a detection efficiency smaller than one is affected by fluctuations in the number of signal quanta detected. For a scintillator based calorimeter these signal quanta inefficiencies are occurring in the emission and detection of the scintillation light by a photon detector. These fluctuations are following poissonian statistics, thus scaling with  $\sqrt{E}$ . Usually fluctuations in the signal quanta are dominated by other more pronounced fluctuations and do not define the energy resolution of a calorimeter.

### Sampling Fluctuations

In a sampling calorimeter the most obvious type of fluctuations are sampling fluctuations. As the absorber material is not instrumented, only parts of the shower are measured. Event to event fluctuations in the amount of energy deposited in the absorber of a shower lead to different calorimetric responses for incoming particles with the same initial energy. Similar to signal quantum fluctuations, sampling fluctuations follow poissonian statistics as well. The relative uncertainty in the energy measurement due to sampling fluctuations scales as:

$$\frac{\sigma_{\text{sample}}}{E} = a_{\text{sample}} \frac{1}{\sqrt{E}}, \quad (1.14)$$

where  $a_{\text{sample}}$  is a proportionality constant that usually decreases for higher sampling fractions ( $F_{\text{sample}}$ , as described in eq. (1.10)) as  $\frac{1}{\sqrt{F_{\text{sample}}}}$ .

In general, the hadronic shower component is subject to larger sampling fluctuations than the electromagnetic one. Nevertheless, sampling fluctuations are usually not the dominant fluctuations for hadronic showers.

### Fluctuations in the Electromagnetic Shower Content

As we saw in section 1.4.3, a calorimeter often shows different responses to the electromagnetic and hadronic part of the shower due to the invisible energy. Hence, event-to-event fluctuations in the electromagnetic fraction  $f_{\text{em}}$  of hadronic showers have direct influence on the energy measurement. The size of the electromagnetic part of a hadronic shower is given by the amount of energy carried by  $\pi_0$  created in the hadronic cascade. For a  $\pi_0$  created by chance in the first steps of the cascade this may be very large, while for another shower only relatively little energy may be carried by  $\pi_0$ . This leads to very large fluctuations. Usually, these fluctuations are dominating the energy resolution of hadronic showers for non-compensating calorimeters.

### Fluctuations in the Visible Energy

For hadronic showers considerable amounts of energy may be not observable for calorimeters because of the nuclear binding energy lost by releasing nucleons from the target nuclei. This process is subject to large event-to-event fluctuations. First, it is heavily correlated with the electromagnetic fraction of a particular shower, because this effects occurs only in the hadronic part of the shower. Additionally the amount of invisible energy in a shower may vary considerably depending on the exact processes happening in the complex hadronic cascade.

The loss of nuclear binding energy always coincides with the release of nucleons from the target nuclei. Typically many of these released fragments are neutrons. Thus, a strong correlation of the kinetic energy of these neutrons with the binding energy loss is expected

and was observed in simulations [42].

### Measurement Dependent Effects

The devices used to instrument the active media may lead to fluctuations in the energy measurement. For photon detectors e.g., random noise hits may add to the signal. Further, unusually large signals may be produced under certain circumstances, for example when a strongly ionizing particle is created inside the active medium, or right at the end of an absorber plate. Particles directly hitting the active surfaces of the readout devices (such as photodetectors) may also produce large signals that are not directly proportional to the deposited energy of the constituents of the shower.

Additionally, effects due to the setup of the calorimeter may include gaps between the active components leading to fluctuations in the amount of measured energy. If the calorimeter is too small in longitudinal or radial direction, significant amount of energy may be lost (*leakage*) with large event-to-event fluctuations. This is especially relevant for hadronic showers.

#### 1.4.5 Compensation

The fact that part of the hadronic shower cannot be measured directly by the calorimeter generally leads to a different response of the calorimeter for the electromagnetic part  $e$  of the shower and its hadronic part  $h$ . This difference is expressed with the  $e/h$  variable quantifying the response of the calorimeter to the electromagnetic part over the hadronic part of the shower. It can be written in terms of the response of the calorimeter to the different shower particles of a hadronic shower normalized to the MIP response [31]:

$$\frac{e}{h} = \frac{e/mip}{f_{rel} \cdot rel/mip + f_p \cdot p/mip + f_n \cdot n/mip}, \quad (1.15)$$

where  $rel$  is the response to relativistic, non-electromagnetic shower particles,  $p$  is the response to spallation protons and  $n$  is the response to evaporation neutrons. The relative fraction of these processes in the hadronic shower are represented by  $f_{rel}$ ,  $f_p$  and  $f_n$  respectively. The three parts of the hadronic component interact very differently with the surrounding material. The relativistic part loses its energy predominantly due to ionization and excitation. The vast majority of the spallation protons in a hadronic shower are non-relativistic and usually have a calorimeter response different from the relativistic part. The neutron's response is dominated by the neutron elastic scattering and neutron capture processes described in section 1.3.3.

Because of the invisible energy in the hadronic part of the shower, most calorimeters are *under-compensating*, meaning  $e/h > 1$ . For a careful calorimeter designs, however, the hadronic response can be enhanced in order to achieve *compensation*, meaning that  $e/h$

is close to one. A calorimeter with  $e/h < 1$  is called *over-compensating*. The large fluctuations in  $f_{em}$  and the invisible energy lead to a significantly worse energy resolution in non-compensating calorimeters for hadrons compared to compensating calorimeters.

The mechanisms how compensation can be achieved are most easily seen by rewriting eq. (1.15). In first approximation we can assume that in a typical calorimeter the relativistic hadronic part gives a similar energy response than the electromagnetic part of the shower ( $rel \approx e$ ). If we further assume that the fraction of the neutron contribution and the contribution due to spallation protons is proportional to each other ( $f_p \approx k \cdot f_n$ , with proportionality factor  $k$ ), we can write eq. (1.15) as:

$$\frac{e}{h} = \frac{e}{(1 - f_n(1 + k)) \cdot e + f_n \cdot (n + k \cdot p)} \quad (1.16)$$

$$= \frac{1}{1 + f_n \left[ \frac{(n+k \cdot p)}{e} - (1 + k) \right]}, \quad (1.17)$$

where the *mip* normalization is dropped and it is used that  $f_{rel}$  can be written as  $1 - f_n(1 + k)$  (because  $1 = f_{rel} + f_n(1 + k)$ ). In calorimeter applications the electromagnetic and hadronic part cannot be measured separately. Thus it is instructive to look at the calorimeter response ratio of pions and electrons ( $\pi/e$ ) of a given energy which relates to  $e/h$  as follows [31]:

$$\frac{e}{h} = \frac{1 - f_{em}}{\pi/e - f_{em}}. \quad (1.18)$$

Substituting eq. (1.17) and the above formular leads to:

$$\frac{1 - f_{em}}{\pi/e - f_{em}} = \frac{1}{1 + f_n \cdot C}, \quad (1.19)$$

with  $C = \frac{n+k \cdot p}{e} - (1 + k)$ . It follows that:

$$\frac{\pi}{e} = 1 + f_n \cdot (1 - f_{em}) \cdot C. \quad (1.20)$$

The fraction of the energy carried by neutrons  $f_n$  is understood relative to the hadronic part of the shower. Analogously we can define  $f_N = f_n \cdot (1 - f_{em})$  as the fraction of energy carried by neutrons with respect to the shower energy. Written in terms of  $f_N$  we get:

$$\frac{\pi}{e} = 1 + f_N \cdot C. \quad (1.21)$$

It can be seen that compensation can be achieved by tuning the  $C$  term to be close to zero (which implies  $n = p = e$ ). Historical, the effect of fission in depleted uranium ( $^{238}U$ ) was used to enhance the neutron response (see e.g., the ZEUS uranium-scintillator calorimeter

[43]). Compensation can also be achieved without the mechanism of fission and the use of uranium. By exploiting the large differences in the energy loss of evaporation neutrons in high  $Z$  absorber materials and hydrogen rich active materials via elastic scattering (see section 1.3.3), the neutron response of the calorimeter can be tuned by choosing the right ratio of both materials. Furthermore, the electromagnetic response of the calorimeter can be suppressed, for example by absorber layers of materials with a much smaller radiation length  $X_0$  compared to the nuclear interaction length  $\lambda_{\text{int}}$ , as it is the case for tungsten.

It is not always feasible to build an intrinsically compensating calorimeter without sacrificing other goals of the experiment. It can be seen from eq. (1.21) that if  $f_N$  can be estimated for each shower, compensation can be done "offline" by weighting each pion shower depending on  $f_N$ . This method is called offline, or *software compensation* and will be explained in more detail in section 2.4.3.

#### 1.4.6 Energy Resolution

The energy resolution of a calorimeter is defined by the fluctuations stated above. The relative energy resolution can be parameterized as:

$$\frac{\sigma_E}{E} = \sqrt{\left(\frac{A}{\sqrt{E}}\right)^2 + B^2 + \left(\frac{C}{E}\right)^2}. \quad (1.22)$$

Signal and sampling fluctuations are summarized by the stochastic term with the proportionality constant  $A$ . Inhomogeneities of the detector and calibration effects typically add a constant term  $B$  to the relative energy resolution. Effects that add an energy independent fluctuation (e.g., electronic noise) are denoted in the  $C$ -term. The relative energy resolution for this term scales with  $\frac{1}{E}$ .

Often, the  $C$ -term is only relevant for very low energies. At high energy experiments, the  $B$ -term is dominating, while the stochastic  $A$ -term dominates the lower end of the typical energy spectrums.

#### 1.4.7 Time Development of Hadronic Showers

The electromagnetic processes of a hadronic shower are very fast  $< 1$  ns. Their time distribution is mainly defined by the radial and longitudinal extension of the shower. This is also true for the relativistic part of the hadronic processes including all relativistic constituents. Because of the large extent of hadronic showers in radial and longitudinal direction, the propagation time of the shower may extend to a few ns.

Besides this quasi-instantaneous, relativistic shower component, two processes may lead to a delayed component extending to much later times after the start of the shower. First, non-relativistic, slow particles with large mean free path lengths may interact with the traversed medium. Second, delayed de-excitations of nuclei may lead to the production of

secondary particles. Instrumental effects may also lead to delayed calorimetric signals.

Typically, the evaporation neutrons originating from spallation processes are dominating this late part of the shower. In the first several 10 ns the evaporation neutrons are losing most of their energy via elastic scattering. Afterwards, these slow neutrons may be captured by the absorber's nuclei under the emission of photons. This process happens at very long time scales up to milliseconds after the shower start. The exact timescales of the processes are to a large extent material dependent.

Figure 1.8 shows the time distribution of hadronic showers in a steel and a tungsten absorber measured by the T3B experiment [16] using scintillators. Besides the instantaneous part, a delayed component with a fast and a slow subcomponent can be distinguished. The slow component is dominating the hit time distribution for hit times later than 50 ns and is extending to much larger hit times than shown here. The late shower activity is enhanced for the tungsten absorber compared to the steel absorber. In simulation studies it could be shown that the fast part of the late component is dominated by neutron elastic scattering processes, while the slow part is due to neutron capture [44].

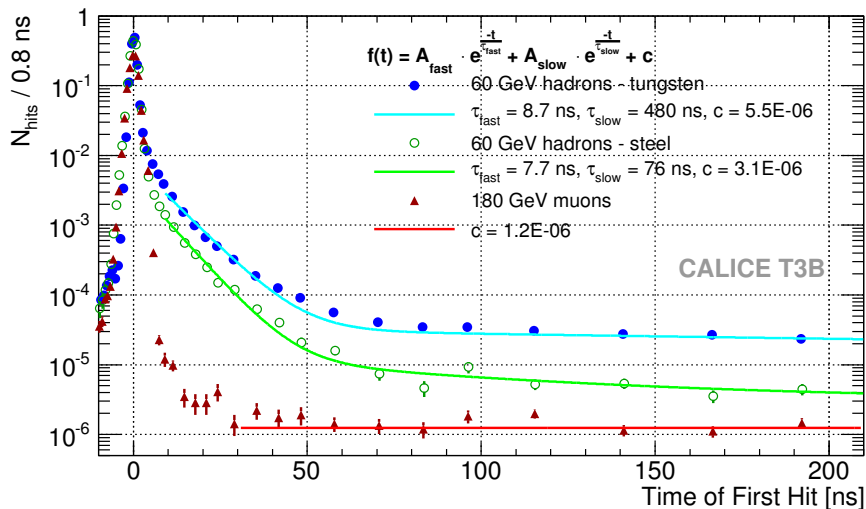


**Figure 1.8** – Time structure of 60 GeV hadrons in tungsten (cyan) and steel (green) compared to 180 GeV muons (red) measured by the T3B experiment [16].

The time distribution of a given shower is expected to correlate with its hadronic fraction [45]. For showers with a larger hadronic part, more neutrons are generated leading to a larger delayed component compared to a shower with a higher electromagnetic fraction. Similar, the absorber material plays a large role in the time distribution of hadronic showers. High  $Z$  materials are expected to produce more neutrons compared to materials with lighter nuclei, as observed in fig. 1.8.

When discussing the time development of the measured signals in a realistic calorimeter system, also instrumental effects have to be taken into account. Slow active materials and instrumentation could significantly delay signals. In plastic scintillators, for example, late

emission of photons due to phosphorescence could lead to late signal contributions (see section 1.4.1).

The precise measurement of the hit times in a calorimeter system could be used in various ways to enhance the detector performance. With higher luminosities, pile-up of collision events, or beam background events may degrade the performance of a detector system. High precision timing capabilities in the calorimeter are capable of reducing this problem. This is true for high luminosity proton-proton colliders [46] as well as for future  $e^+e^-$ -colliders with high beam backgrounds [47]. Because of the different time structures of electromagnetic showers compared to hadronic showers, the hit time information can also be used for particle identification purposes in a calorimeter [48, 49].

Novel, highly granular calorimeters, as discussed in section 1.6, may offer additional ways for performance improvements due to hit time information. First, timing cuts on hadronic showers may be used to reduce the size of hadronic showers leading to better cluster separations [50]. This can be useful for particle flow approaches (see below). Further, the time information could be used to enhance the energy reconstruction of such a calorimeter by using the correlations of the hit time measurements with the physics processes in the shower development. The latter is subject of this thesis in part III.

## 1.5 Simulation of Hadronic Showers

Simulating the response of calorimeters and thus the shower development in different absorber materials is an essential part of high energy physics. While electromagnetic showers are understood well and can be modeled with high precision, the simulation of hadronic showers is more involved. Because of the complex nature of hadronic showers, a single model can usually not describe the showers accurately over the complete energy range. Instead, a compilation of several models in so called *physics lists* are used for different energy ranges, particle types and applications. Throughout this thesis, the Geant4 framework [51] is used for the simulation of hadronic showers and several Geant4 based physics lists are employed.

Geant4 is a toolkit for simulating the passage of particles through matter based on Monte Carlo methods. For this, a detailed geometry description of the detector model together with its material composition is necessary. The physics interactions of the particles with the materials are following the processes implemented in the physics lists. Sensitive detector volumes can be defined to simulate the detector response. A detailed list of the physics processes implemented in Geant4 can be found in [52].

The following physics lists are used and compared for the time analysis in this thesis. All of these physics lists use the same common implementation to model electromagnetic interaction.

- **QGSP\_BERT:** This physics list relies on the *Bertini intranuclear cascade model* [53] for low energies ( $< 10\text{ GeV}$ ). The Bertini cascade models the intranuclear interactions as

subsequential particle-particle interactions. For high energies ( $> 25$  GeV) the *quark-gluon string model* is used to describe hadron-nucleon inelastic scattering. In the quark-gluon string model [54], a string is modeled between two quarks of the scattering particles. These strings can be fragmented (provided they carry enough energy) to generate quark-antiquark pairs. The produced quarks further form hadrons (hadronization). In between both models, the *LEP* model is used, which is a parameterized model based on fits to experimental data.

- **QGSP\_BIC:** In the QGSP\_BIC physics list, the Bertini cascade is substituted with a binary cascade model for low energies [55]. The main difference between both cascade models is the modeling of the nuclei. The high energy behavior is the same as for the QGSP\_BERT list.
- **FTFP\_BERT:** The FTFP\_BERT physics list employs the Bertini cascade as well but only up to 5 GeV. For higher energies, the *Fritiof parton string model* is used. This model differs from the quark-gluon string model in the string formation and the string fragmentation process [54].
- **QBBC:** The QBBC physics list uses the Bertini cascade up to 5 GeV, the Fritiof string parton model up to 25 GeV and the quark-gluon string model for higher energies.
- **High Precision Neutron Package\_HP:** The high precision neutron package is an extension to the QGSP\_BERT, FTFP\_BERT and QGSP\_BIC physics lists. It employs a special neutron treatment showing better performance of the time structure for hadronic showers in tungsten absorbers for Geant4 v9.3 [16].

## 1.6 Calorimetry at Future $e^+e^-$ -Collider Experiments

The ILD and SID detectors are proposals for future  $e^+e^-$ -collider experiments at the ILC [56] and based on these the CLICdet detector is proposed for CLIC [57]. As an example, a schematic view of the SID detector is shown in fig. 1.9. As for most multi purpose detectors, the ILD and SID detectors contain a vertex detector, a tracker, a calorimeter system as well as a muon detector. A strong magnetic field leads to a bending of the paths of charged particles from which the momentum of those particles can be determined in the tracker.

A special task of a multi purpose detector at a high energy particle physics experiment is the measurement of the energy of a *jet* of particles. A jet is formed by the hadronization process of a quark or a gluon and consists of many different particles. The measurement of the jet energy is important, because jets are produced in every hadronic final state of a high energetic particle collision. At the LHC experiments the jet energy resolution for 100 GeV jets is about 10 % [58, 59]. As discussed in section 1.2, future  $e^+e^-$ -colliders aim at a jet energy resolution of 3 to 4 % at 100 GeV.

Traditionally, the jet energy is measured by adding all energy depositions in the electromagnetic and hadronic calorimeter within a certain region defined by a jet clustering algorithm. With this approach it is not feasible to design a calorimeter that could reach the desired jet energy resolution, because the resolution is limited by the energy resolution of the calorimeter systems. Therefore, an alternative approach for measuring the jet energy is needed to achieve the desired jet energy resolution at future  $e^+e^-$ -colliders.

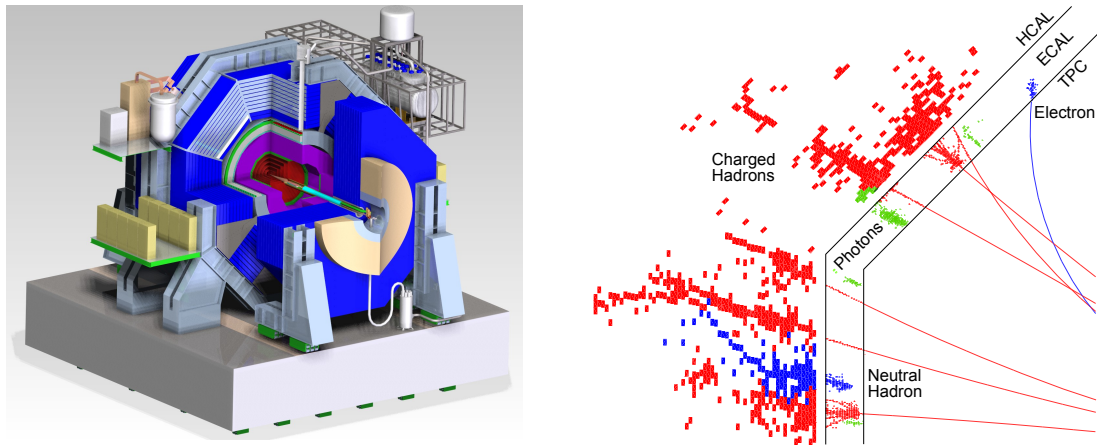


**Figure 1.9** – *Left*: Schematic view of the SID detector [56]. *Right*: A typical 250 GeV jet in a section of the ILD detector [60].

### 1.6.1 Particle Flow Approach

In a multi purpose detector, single charged particles can often be measured with much higher precision in the tracking detectors instead of the calorimeters. For jet energy measurements, this was exploited already in the ZEUS [61], ALEPH [62] and CMS experiments [63] and is called the *particle flow* approach.

The energy of a particle jet is on average carried to 62 % by charged particles, to 27 % by photons, to 10 % by neutral hadrons and to 1.5 % by neutrinos, with large event-to-event fluctuations. If the charged particles are measured in the tracking detector, the calorimeters are only needed for the measurement of photons and neutral hadrons. Consequently, the energy depositions of the charged particles need to be subtracted from the calorimeter response. This technique requires an excellent single particle identification within a jet.

For current proposals of  $e^+e^-$ -collider experiments, the detector design is optimized for the particle flow approach. In this context, the spatial resolution of the calorimeters plays an important role for separating neighboring and partially overlapping showers. The tracks of the charged particles need to be assigned correctly to the energy depositions in the calorimeter. The *confusion*, meaning the wrong association of energy depositions to the charged particle tracks, is dominating the jet energy resolution of a particle flow detector instead of the single particle energy resolution of the calorimeters at higher energies [64].

Thus, calorimeters with a fine 3-dimensional segmentation are required for such detector systems. The development of highly granular calorimeters imposes several challenges to be solved for future  $e^+e^-$ -collider experiments, mainly due to the high channel count.

In the next chapter, an overview of the CALICE Analog Hadronic Calorimeter (AHCAL) project is presented. The technologies used for realizing such a calorimeter are discussed and several prototypes which are used throughout this thesis are introduced.



## Chapter 2

# CALICE Analog Hadronic Calorimeter

The CALICE collaboration develops highly granular calorimeters for future high energy physics experiments. One of the main objectives is to explore and test various technologies to realize such a calorimeter. The focus within the CALICE collaboration is both on the electromagnetic and hadronic part of a calorimeter system.

One of the proposed technologies for a hadronic calorimeter is the AHCAL. The AHCAL is a sampling calorimeter using a steel or tungsten absorber. The active components are scintillators with a Silicon Photomultiplier (SiPM) read-out. In this chapter an overview of the AHCAL project is given. The used technologies of several prototypes are discussed and the reconstruction and Monte Carlo simulation processes are reviewed.

### 2.1 AHCAL Concept

As mentioned in section 1.6, the main goal of a hadronic calorimeter in a particle-flow oriented detector is the separation of neutral hadrons and charged hadrons and the precise energy measurement of neutral hadrons. Within the CALICE collaboration there are several detector concepts developed and studied. For the digital and semi-digital hadronic calorimeter projects, the focus is on an extremely high channel count. This comes at the cost of a reduced energy information for each channel. The digital calorimeter with a proposed cell size of  $1.0 \times 1.0 \text{ cm}^2$  gives information on whether or not a hit in a cell occurred (1 bit resolution) using resistive plate chambers [65]. The semi-digital calorimeter has three thresholds which indicate whether there was a small, medium or high energy deposition in this cell (2 bit resolution) [66].

The AHCAL aims at a cell size of  $3.0 \times 3.0 \text{ cm}^2$ . This allows for an analog energy measurement in each cell on the compromise of fewer channels. Also cell sizes of  $6.0 \times 6.0 \text{ cm}^2$  are studied with the aim to reduce the costs of the calorimeter [67].

For the absorber material, two options are discussed. For detectors at the ILC, steel is the preferred absorber material. Using tungsten as an absorber material has a main advantage of

a higher density. This allows for a more compact calorimeter which is especially interesting for a hadronic calorimeter at future  $e^+e^-$ -facilities that are aiming at higher energies ( $> 1$  TeV) as proposed for CLIC. On the downside, tungsten is significantly harder to manufacture and more expensive compared to steel. In addition, in tungsten, more neutrons are produced in hadronic showers which leads to a disadvantageous time structure (see section 1.4.7).

One of the main challenges of a scintillator based calorimeter system with small cell size is the detection of the scintillation light of particles passing through the active material. Traditionally, this is done using Photomultiplier Tubes (PMTs). PMTs are relying on a cascade of dynodes with a high bias voltage, usually in the order of a few kV. Between each dynode the electrical signal is amplified, leading to an output signal large enough to be measured by the readout electronics. Disadvantages of PMTs are including the high bias voltage, sensitivity to magnetic fields and the size, which typically is in the order of several cm. These properties are the reason why PMTs are not ideal for highly granular calorimeters, as they cannot be integrated easily into a compact layer structure in large quantities.

SiPMs are overcoming these drawbacks. They are much smaller than PMTs and they can be produced cost efficiently in large quantities. Furthermore, they are insensitive to magnetic fields and hence can be integrated into the active layers of a calorimeter. These properties make them highly suitable for high energy physics detectors [7]. The following section discusses the most important concepts of SiPMs.

### 2.1.1 Silicon Photomultiplier (SiPM)

SiPMs are silicon based photon detectors. Compared to traditional PMTs they are much smaller. As they are used as active elements within the AHCAL, their properties have a large influence on the detector's performance, the technical requirements of the readout electronics and the calibration procedure. The working principle of a SiPM is illustrated schematically in fig. 2.1. SiPMs consist of many photodiodes operated in parallel on one silicon chip in *Geiger mode*. On impact of a photon an electron-hole-pair may be created in the silicon. Due to the applied bias voltage, this electron-hole-pair gets amplified until the current exceeds a certain amount, which results in a *quenching* of the current. The result is a signal of a fixed amount of charge in that pixel, which can be measured. By measuring the output signal of the whole device the number of fired pixels can be inferred. This is in first order proportional to the number of photons reaching the SiPM. An important property of a SiPM is its breakdown voltage  $V_{\text{break}}$ , the minimal operating voltage for that the self amplification process occurs. The over voltage is defined as the operating voltage  $V_{\text{bias}}$  above  $V_{\text{break}}$  ( $V_{\text{over}} = V_{\text{bias}} - V_{\text{break}}$ ). In this section a few general properties of SiPMs are discussed:

- **Photon Detection Efficiency (PDE):** The PDE is the probability to detect a photon hitting the sensor. Typically, it is approximately 30 % but may heavily depend on the photon's wavelength, the overvoltage and the SiPM pixel size [68]. The PDE depends

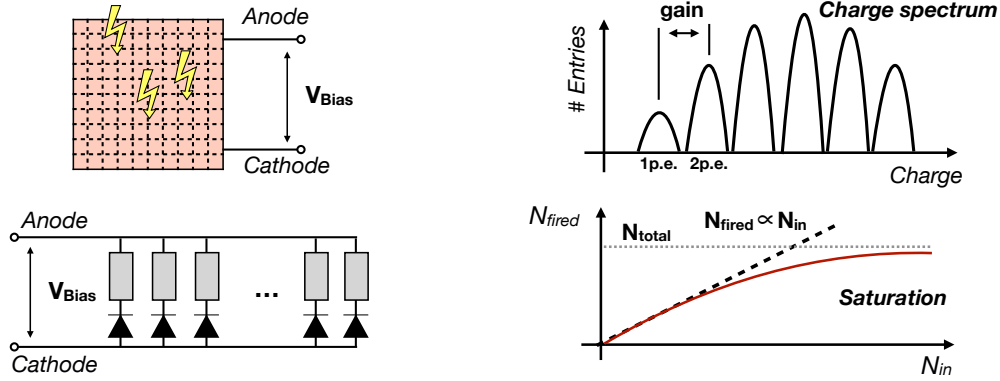


**Figure 2.1** – *Left*: Schematic top-view of a SiPM as a two dimensional array of pixels (*top*). Electronic schematics of a SiPM as an array of photodiodes in parallel. The output signal is the sum of the charge collected in each fired photodiode (*bottom*). *Right-top*: Idealized illustration of a charge spectrum of a SiPM. The measured charge depending on the number of fired pixels (p.e.) can easily be identified. The gain is the distance between the peaks in the charge spectrum. *Right-bottom*: Illustration of the saturation effect of a SiPM.

on the propability of the photon hitting an active part of the sensor (called the fill factor  $FF$ ), the probability of the photon creating an electron-hole pair (called the quantum efficiency  $QE$ ) and the propability of this electron-hole pair triggering an avalanche  $\epsilon_{\text{avalanche}}$ :

$$PDE = FF \cdot QE \cdot \epsilon_{\text{avalanche}}. \quad (2.1)$$

Because of the finite PDE, the detection of photons hitting the SiPM is a probabilistic process. Thus, the distribution of the number of detected photons originating from a fixed size of incoming photons follows a poissonian distribution

Due to this inefficiencies the resulting signal of a fixed amount of photons reaching the active area of a SiPM follows a poissonian distribution.

- **Gain:** The *gain* of a SiPM is the amplification of the initial electron-hole-pair. It is proportional to the applied overvoltage  $V_{\text{over}}$  and the capacitance of a SiPM pixel [69]:

$$\text{gain} \propto C_{\text{pixel}} \cdot V_{\text{over}}. \quad (2.2)$$

The gain can be determined by dividing the accumulated measured charge by the amount of fired pixels (see fig. 2.1 (*right*)).

- **Darkrate, crosstalk & afterpulses:** Several effects may cause a cascade in a pixel without an actual photon triggering the avalanche. The *darkrate* is the rate at which a single pixel of a SiPM fires without a photon reaching the pixel. In recent years the darkrate of common SiPMs improved from several MHz down to several kHz. When a SiPM produces a signal, two main effects can cause additional pixels to trigger an avalanche.

First, *crosstalk* between pixels on the SiPM can cause neighboring pixels to trigger an avalanche as well. Second, *afterpulses* may occur after a pixel was fired and trigger another avalanche in the same pixel.

- **Saturation:** As the amount of pixels in a SiPM is finite, and a single pixel has a dead-time of up to a few hundred ns, saturation effects occur if the number of incoming photons within this time scale gets close to the total number of pixels  $N_{\text{total}}$  of the SiPM. The expected number of fired pixels  $N_{\text{fired}}$  can at first order be approximated as

$$N_{\text{fired}} = N_{\text{total}} \cdot (1 - \exp(-\epsilon N_{\text{in}} / N_{\text{total}})), \quad (2.3)$$

with  $\epsilon$  being the efficiency (PDE) of an incoming photon leading to a fired pixel and  $N_{\text{in}}$  is the number of incoming photons. This is visualized in fig. 2.1 (*right*). The dynamic range of the SiPM can be enhanced by choosing a model with a particularly large number of pixels. This usually comes at the costs of a lower fill factor and thus a lower PDE.

- **Temperature dependence:** An important property of SiPMs is the temperature dependence of the breakdown voltage  $V_{\text{break}}$ , which in turn has an influence on the gain of the SiPM. A higher temperature leads to a higher break down voltage of the device, resulting in a lower over voltage and thus a lower gain. Typical temperature gradients are in the order of  $50 \text{ mVK}^{-1}$  [69]. This means that for high precision measurements the temperature has to be controlled.
- **Timing properties:** The SiPM has a fast component, the build-up of the avalanche process, which determines the time resolution of a SiPM. The decline of the signal is much slower (usually several 10 ns). The slow component is determining the deadtime of the SiPM. The time resolution of a single pixel of a SiPM is typically in the order of 100 ps [70]. In use with large plastic scintillators, the light development within the scintillator is usually the limiting factor for the time resolution of the combination of scintillator and SiPM.

## 2.2 AHCAL Physics Prototype

The AHCAL physics prototype [71] is the first large scale AHCAL prototype that was build with the goal to prove the physical concept of a highly granular calorimeter. The achievable energy resolution was studied and algorithms exploiting the granularity of the detector in order to enhance the energy resolution were developed [11]. Furthermore, the granularity allowed to perform studies of the details of the development of electromagnetic and hadronic showers. This was done with steel [72, 73] and tungsten [74, 75] absorbers and the results were

compared to Monte Carlo (MC) simulations. The latter studies are an important feedback for the improvement of these processes within the GEANT4 MC simulation [76].

## 2.3 AHCAL Technological Prototype

A second generation of AHCAL prototypes, the *technological prototypes*, have been constructed after the first successful series of test beams with the physics prototypes. The goal of the technological prototypes is to test different technologies for the active elements and to demonstrate the use of mass-production techniques for the construction. Key features that are established with the technological prototypes are the integrated electronics, *power pulsing*, and *active temperature compensation*. In this section the basic technologies of the technological prototypes are discussed as well as the different prototypes.

### 2.3.1 Front-end ASIC: SPIROC2

The *SiPM integrated readout chip* (SPIROC) [77] is used for reading out the SiPM signals in the technological prototypes discussed in this thesis. A schematic layout of one channel of the SPIROC2 chip is shown in fig. 2.2. SPIROC is designed specifically for SiPM readout for an HCAL at the ILC. One chip can operate 36 input channels. As active cooling should be minimized in the AHCAL one of the requirements for the ASIC is a power consumption below 25  $\mu\text{W}$  per channel. This requirement can only be fulfilled with the power-pulsing technique explained in section 2.3.2. In order to enhance the dynamic range, the SiPM output is amplified by two different preamplifiers, a low-gain preamplifier for large input signals and a high-gain one for small signals. After passing a slow shaper, the signals are stored in one of 16 memory cells. The 16 memory cells are a buffer implemented for each channel where the analog signals are stored until they are digitized. Depending on the height of the initial SiPM signal, the high-gain or the low-gain value is selected for digitization in a 12-bit analog to digital converter (ADC) and subsequently forwarded to the higher level data acquisition (DAQ) systems.

Hit time measurements are realized via a voltage ramp (see e.g., [79] for details). A voltage is ramping up with a steady slope, such that the time at which a given hit occurs is proportional to the height of the voltage. Upon a hit, the current height of the ramp is first stored in analog memory cells as for the charge measurement. Upon the end of the acquisition cycle the time information is digitized by the same ADC as the charge measurements. The digitized output values of the time measurement are called *TDC* values similar to the ADC values of the charge measurement. In order to avoid edge effects of the TDC ramps, two of such ramps are used in an alternating way. This is visualized in fig. 2.3. The intrinsic time resolution of the SPIROC2b chip was measured to be 1.7 ns [80].

The maximum time over which the voltage may ramp up for time measurements is called the *bunch crossing* length. A bunch crossing is the basic time unit in which hits across the

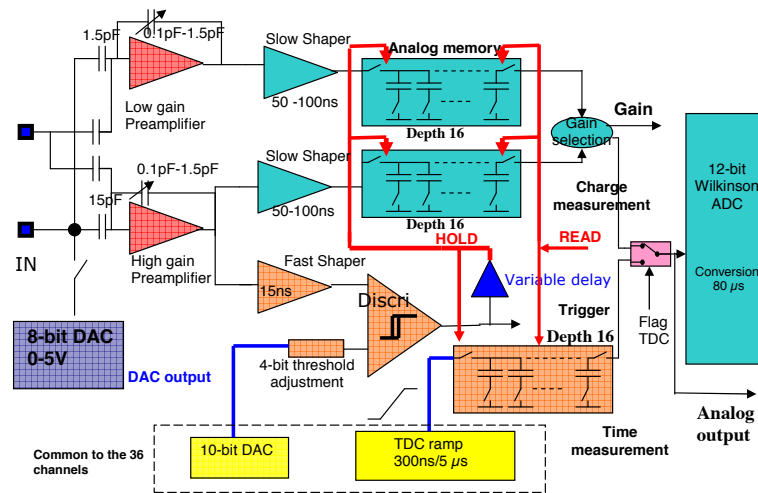


**Figure 2.2** – Schematic Layout of one channel of the SPIROC2 chip. Taken from [78].

detector are associated to the same event. For an  $e^+e^-$ -collider experiment this would be the time between particle collisions. The proposed collision time structure of the ILC foresees bunches of particles approximately 200 ns apart organized in bunch trains. The bunch trains occur with a frequency of 5 Hz. For test beam campaigns at the SPS at CERN, the time structure of events is organized in spills with repetition times usually in the order of tens of seconds with no guaranteed structure within the spills.

In order to account for these differences, the SPIROC ASIC can be operated in two modes. The *test beam mode* uses a bunch crossing length of 4000 ns, while the *ILC mode* has a bunch crossing length of 200 ns. A shorter bunch crossing length increases the slope of the ramp and thus gives a more precise time measurement. However, for test beam measurements this mode is not efficient, as many empty events are produced due to the much lower beam rate. Thus, for test beam campaigns usually the chip is operated with larger bunch crossing lengths. As the digitization of the time measurement is done with a 12-bit ADC, the bin width of one TDC value is about  $\frac{4000\text{ns}}{4096} \approx 1\text{ ns}$ . This approximation holds only if the voltage ramp uses the full dynamic range of the ADC. In reality, the slope of the ramp and its pedestal value varies significantly across different chips and thus a proper calibration is necessary.

### 2.3.2 HCAL Base Unit

The basic unit of an AHCAL active layer is the HCAL Base Unit (HBU). It is a circuit board hosting the SiPMs as well as the integrated readout electronics, the SPIROC chips. The HBU forms the connection of those elements to the higher level DAQ systems [81]. One HBU consists of four readout chips, each operating 36 channels. Four HBUs are assembled together to form a full *module*. Figure 2.4 shows the front and backside of an HBU. For a calorimeter at a future  $e^-e^+$  collider these modules can be mounted together to form bigger structures. For stability, the HBUs are mounted within a steel cassette of 0.5 mm thickness.

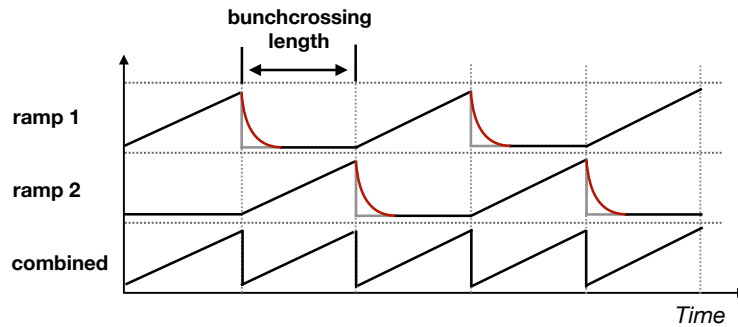


**Figure 2.3** – Timing scheme of the SPIROC TDC ramps. In order to avoid edge effects of the ramps shown exaggerated in red, the combination of two alternating ramps is used for time measurements. Adapted from [79].

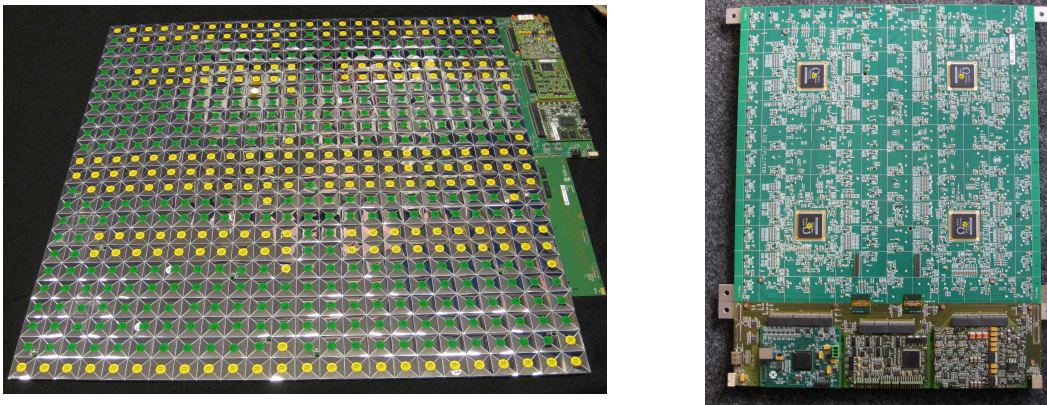


**Figure 2.4** – *Left*: Front side of a HCAL module made out of four HBUs equipped with scintillating tiles wrapped in reflective foil. *Right*: Backside of an HBU with the four readout ASICs (black) [15].

### Power Pulsing

The tight power budget of a readout chip for a highly granular calorimeter requires an optimal use of the available power. This is realized by exploiting the special time structure of future linear  $e^+e^-$ -colliders. With particle bunches organized in bunch trains extending over about 1 ms and a spacing between the bunch trains of about 200 ms, the readout electronics is idle for about 99% of the time. The concept of power pulsing [82, 83] is a rapid power cycling of the active components to power only the parts that are currently needed for readout and processing of the data.

### Temperature compensation

As described in section 2.1.1, the breakdown voltage of a SiPM and hence its gain is dependent on the temperature. While for the physics prototype this dependency is compensated with

temperature dependent calibration constants, for the technological prototypes an active regulation of the overvoltage of the SiPMs is implemented (temperature compensation). Temperature sensors on various points in the active layers are constantly measuring the surrounding temperature. The overvoltage of the SiPMs can then be regulated via the readout chip accordingly [84].

### 2.3.3 Data Acquisition and Event Building

The data acquisition system [85] is built up in several layers and is fully scalable for a large  $e^+e^-$ -collider detector. On each HCAL module, the *detector interface (DIF)* is the first step in the data aggregation. This component can handle up to 72 ASICs. The *Link Data Aggregator (LDA)* reads out all DIFs and sends the output packages to a computer for storing the raw data. The beam clock is delivered by the *Clock and Control Card (CCC)*. Furthermore, the CCC can deliver an external trigger validation signal during beam tests and it starts the acquisition cycle with the presence of a spill. During the acquisition cycle, the electrical SiPM signals are saved in the analog memory cells of the SPIROC ASIC. After a spill, the analog signals are converted to digital output by the ADC. In the subsequent readout phase, the data is processed further into the DAQ chain.

During each data acquisition cycle, data is recorded over several bunch crossings. The bunch crossing number associated to each hit is saved along with the hit energy and time information. For event building, all hits in the same bunch crossing are associated to the same event. Additionally, for test beam operation, the events are only processed further if they are validated by the external trigger generated by the coincidence signal of two trigger scintillators in front of the AHCAL.

### 2.3.4 Partially Equipped Technological Prototype

A first series of test beam campaigns with the partially equipped technological prototype (PTP) was conducted in 2015. The prototype consists of two (July 2015 test beam) or three (August 2015 test beam) ECAL modules (EBUs), eight partial HCAL modules (one HBU) and four full HCAL modules (four HBUs each). The large modules were placed with an increasing number of empty absorber layers for probing deeper parts of the hadronic showers. Two test beam campaigns were executed in 2015, one in July using a steel absorber stack [50, 86] and one in August using tungsten as the absorber material.

One of the goals of the PTP is to test different SiPMs and tile designs. For that purpose, SiPMs from different vendors (Hamamatsu, Ketek, CPTA and SenSL) and with a wide range of the number of pixels (800 to 12000) are used. The setup consists of scintillating tiles with and without wavelength shifting fibers as well as the new SiPM-on-tile design with surface mounted SiPMs. Figure 2.5 shows a scintillating tile with wavelength shifting fibers (*left*) and a tile with SiPM-on-tile design (*right*). While some of the tiles are wrapped with reflective foil,

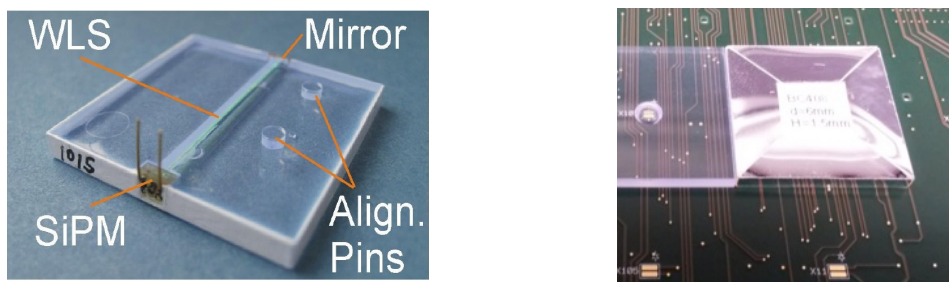


**Figure 2.5** – Different tile designs for the AHCAL prototypes. *Left:* Tile design with wavelength shifting fiber guiding the light to the SiPM mounted on the side of the SiPM. A mirror reflects the light on the opposite side. *Right:* SiPM-on-tile design using surface mounted SiPMs that are glued directly on the HBU. A dimple in the center focusses the scintillation light.

some modules contain scintillating tiles without wrapping. A complete list of the used SiPM and tile combinations for the August 2015 test beam is presented in appendix A.1. A picture and schematic drawing of the test beam setup are shown in fig. 3.1.

Another main objective of the test beams with the PTP is the testing of the integrated electronics. Additionally, it is the first prototype with the possibility of precision hit time measurements for all channels in a large scale CALICE prototype.

### 2.3.5 Small Technological Prototype

The small technological prototype consists of a small non-magnetic steel stack with 15 active layers each holding a single HBUs. Because of the compact size of the prototype the objective is mainly to study the AHCAL response to electromagnetic showers. Further, it is used to establish the concept of power pulsing within the AHCAL and to test the performance of the prototype in strong magnetic fields [87].

### 2.3.6 Large Technological Prototype

The large technological prototype (LTP) [15] was commissioned in 2018 and operated in test beam campaigns in May and June 2018. It consists of 38 modules, each containing four HBUs, resulting in 21888 channels in total. The construction of this prototype is a first step towards large scale mass production of channels which is necessary for the construction of a possible highly granular calorimeter at a future collider facility with  $\mathcal{O}$  (10 Million) channels.

It is homogeneously equipped with surface mounted SiPMs, and scintillating tiles without wavelength shifting fibers, a size of  $30 \times 30 \times 3 \text{ mm}^3$  and the characteristic dimple in the center (see fig. 2.5 *right*). The dimple helps coupling the SiPM to the scintillator and significantly enhances the uniformity of the collected light across different impact positions on the tile [88]. All tiles are wrapped in reflective foil.

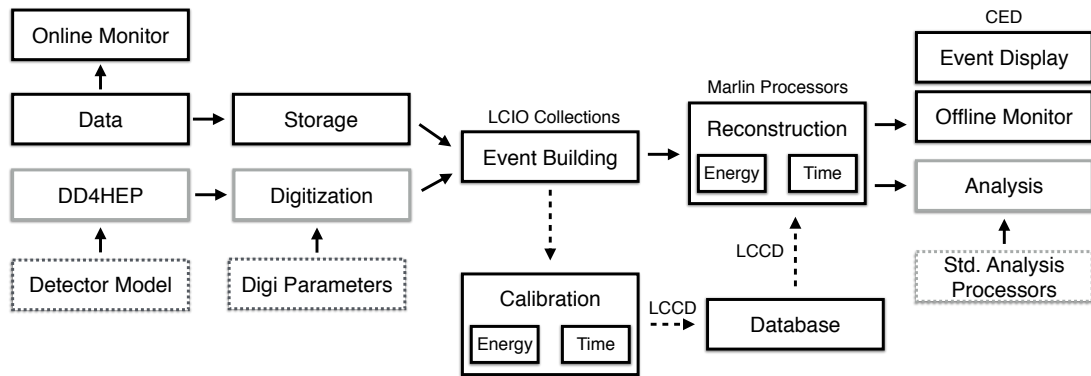


**Figure 2.6** – CALICE AHCAL software framework. Details about the different steps are given in the text.

## 2.4 Energy Reconstruction in the AHCAL

In this section a brief overview of the software environment used for the reconstruction and simulation of AHCAL data is given. Further, the standard methods for energy calibration and more advanced energy reconstruction techniques are discussed.

### 2.4.1 Software Framework

For event reconstruction, a dedicated set of software packages, the *CALICESoft* is used. It is build up on *ILCSofT* [89] and consists among others of MARLIN processors for energy calibration and reconstruction as well as geometries for MC simulation and processors for its digitization. An overview of the software workflow for event reconstruction including the simulation is given in fig. 2.6.

After initial event building steps for test beam data and a sophisticated digitization of the simulation data, both data and simulation run through the same reconstruction process. The common data structure are LCIO files from the ILCSofT package. The energy and time calibration of the detector is done on test beam data and the calibration constants are stored in a database. During the reconstruction process via MARLIN processors, these calibration constants are used. After the initial calibration higher analysis processors are run on the data. An event display is available, build up on CED (ILCSofT). During test beam campaigns a dedicated online monitor as well as an offline monitor assure fast data quality checks.

### 2.4.2 Standard Energy Reconstruction

An overview of the standard energy calibration process is illustrated in fig. 2.7. For the standard energy reconstruction several calibration steps are necessary. The general idea is to calibrate each cell to give the same response for high energetic muons. The most probable response that a traversing muon generates in a single cell is called 1 MIP and serves

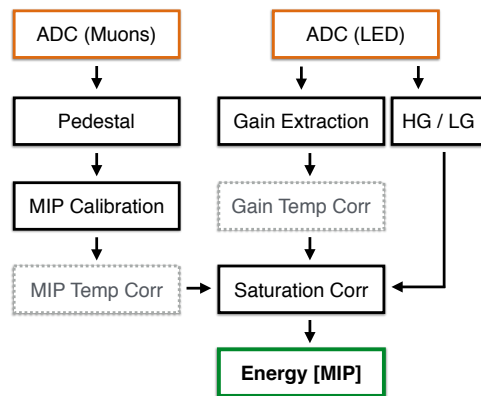


**Figure 2.7** – Energy calibration procedure. The temperature corrections were only necessary for the physics prototype.

as the basic unit for the energy measurement. In order to get the same minimum ionizing particle (MIP) response for all channels, differences between the readout electronics in the channels like the specific amplification factors and pedestal values have to be determined as well as differences in the light yield of the SiPMs. The calibration is done usually on high energetic muon data sets from test beam campaigns, as well as *LED runs* using a built in LED calibration system on the HBUs. Details on the calibration procedure for the PTP can be found in [50, 90, 91]. Details for the LTP are shown in [92, 93]. The different steps of this procedure are described briefly in the following section.

### Pedestal Calibration

Each cell in the detector may have a different electronic baseline that is a fixed offset, also called pedestal, of the measured analog SiPM signal. This has to be subtracted from the raw ADC value. The pedestal calibration is done using the ADC values in cells without a hit. For the PTP, the pedestal value is extracted on the single channel level. For the LTP, the data base structure and reconstruction software was adapted to allow for pedestal values on memory cell level. The cell to cell variations of the pedestal values are in the order of a few percent of a MIP. For the LTP the pedestal values were also determined separately for the low gain mode.

### Gain Calibration

The different SiPMs may have differences in the fixed output charge for a certain number of fired pixels, due to production differences or differences in the delivered operating voltage. The gain value is needed to infer the number of fired pixels of the SiPM. This in turn is the essential quantity for the saturation correction. The gain values are determined by the SiPM response spectra of dedicated LED runs on a channel by channel level.

### Saturation Correction

The effect of SiPM saturation is described in section 2.1.1. In order to counter this effect and maintain the linearity of the hit energy measurements in the calorimeter, a correction function (the inverse of eq. (2.3)) is applied depending on the number of fired pixels in the SiPM.

### High-Gain / Low-Gain Inter-calibration

Two modes for amplifying the SiPM signals are available in the SPIROC chip, depending on the amplitude of the input signal. Higher input signals use the low gain mode with less amplification, while low input signal use the high gain mode with more amplification. This enhances the dynamic range of the amplifiers. The ratio of the two amplification stages needs to be calibrated. This is done in dedicated calibration runs with the LED data and a special readout mode that can read out both the high gain and the low gain output of a signal. The inter calibration factors are determined for every channel.

### MIP Calibration

After all prior calibration steps, the output of all detector cells have to be calibrated with regards to a well defined energy deposition. This is done with the energy depositions of minimum-ionizing particles. Usually, high energetic muons at test beam campaigns are used as minimum-ionizing particles. The energy response spectra for high energetic muons are fitted on channel level with a convolution of a Landau function and a Gaussian function. The most probable value of the fit represents the most probable signal for minimum-ionizing particles, and is taken as the signal for 1 MIP, defining the single cell calibration.

Finally, the hit energy can be converted from ADC values to the MIP scale by using the *pedestal*, *MIP*, inter-calibration (*IC*) and *gain* calibration constants as following:

$$E_{\text{std}}[\text{MIP}] = f_{\text{sat.}}^{-1}(N_{\text{pixel}}) \cdot \left( \frac{(\text{ADC} - \text{pedestal})/\text{IC}}{\text{MIP}} \right), \text{ with } N_{\text{pixel}} = \frac{(\text{ADC} - \text{pedestal})/\text{IC}}{\text{gain}}, \quad (2.4)$$

with  $f_{\text{sat.}}^{-1}$  being the inverse of the SiPM saturation function.

The calibrated hit energies in MIP of an incoming particle showering in the detector can now be added up to define the energy sum in MIP of that event. At test beam campaigns, the energy of the incoming particles in GeV is known. Thus, a relation from MIP to GeV can be obtained, finalizing the energy calibration procedure.

### 2.4.3 Software Compensation

Software compensation is a method of enhancing the hadronic energy resolution by applying offline corrections to intrinsically non-compensating calorimeters. Following eq. (1.21), this

can be achieved by estimating the fraction of shower energy carried by neutrons. In the AHCAL this is done by exploiting the granularity of the calorimeter and using the fact that the electromagnetic part of the shower has a higher energy density than the hadronic part. There are two different approaches to this method studied within the CALICE collaboration: a global approach correcting the shower energy on an event basis by global observables of this shower, and a local approach using different weights for different parts of the hit energy spectrum and thus correcting the measured energy on the hit energy level.

For the physics prototype with steel absorber both approaches show similar results. A 12 % to 25 % resolution improvement is observed over energies ranging from 10 to 80 GeV [11]. Studies of the physics prototype with a tungsten absorber showed about 10 % improvement over the standard reconstruction results both for global and local SC [94, 95]. The improvements are less than for the steel absorber case, as the physics prototype with the tungsten absorber is close to compensating with a response to electrons and pions of  $\frac{e}{\pi} \approx 1$  compared to  $\frac{e}{\pi} \approx 1.2$  for the steel absorber.

## 2.5 Detector Simulation

The AHCAL prototypes are modeled within the MOKKA [96] and DD4HEP [97] packages. These packages are wrappers around the Geant4 simulation toolkit described in section 1.5. While for the PTP the MOKKA package is used, the detector geometry of the LTP is implemented in the more recent DD4HEP framework.

### 2.5.1 Detector Model

The main parts of the detector model are the absorber plates and the active layers of the AHCAL. The active layers are implemented as shown in fig. 2.8 (*left*). An air gap of 1.285 mm is assumed around the steel cassettes on each side. The HBU with all readout electronics is modeled as a printed circuit board (PCB) with an additional 1.5 mm mainly consisting of PVC (cable mix). The scintillator is consisting of polystyrene wrapped in a foil made out of polystyrene. The scintillation saturation is implemented in the simulation for polystyrene using birk's law (see section 1.4.1) and  $k_B = 0.07943 \text{ mm MeV}^{-1}$  [98]. For the Ecal Base Units (EBUs) in the PTP, the composition is the same with the exception of a thinner scintillator (2 mm). The total implementation of the active layer has a thickness of 9 mm. The absorber stacks are simulated as a series of steel plates (17.2 mm) for the steel stack or as 10 mm of a tungsten alloy (93 % W, 5.3 % Ni and 1.7 % Cu) and a 0.5 mm steel support for the tungsten stack [99]. This leads to a total layer depth of 26 mm for the steel stack and to 19.5 mm for the tungsten stack. Other elements in the beam line besides the AHCAL are modeled as well, as for example the trigger scintillators or the Cherenkov detectors. Figure 2.8 (*right*) visualizes the geometry implemented in the simulation for the PTP setup with tungsten absorber. In Geant4, particles are only created when their expected range in the material is larger than

a cut-off value (range cut). Throughout this thesis, this cut-off is set to the CALICE default value of 0.05 mm.

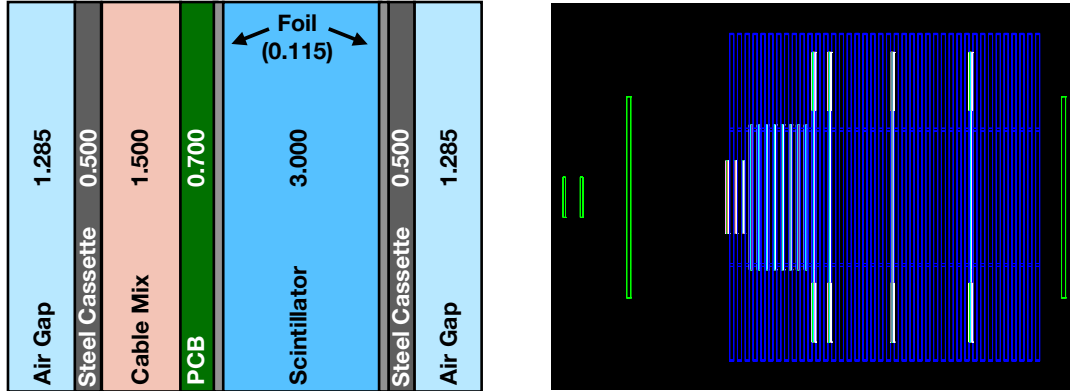


**Figure 2.8** – *Left:* Geometry implementation of an active layer in the AHCAL simulation. All values are given in mm. *Right:* Visualization of the tungsten PTP setup in the simulation. The tungsten layers are shown with a blue frame. The trigger scintillators (three in front, one behind) are shown in green.

### 2.5.2 Digitization

The output of the Geant4 simulation are energy depositions in the sensitive detector of the model implementation in GeV. The digitization procedure aims at transforming this idealized simulation output to a realistic detector output including effects on the data due to the active material, readout detectors and readout electronics. An overview of hit energy digitization steps is illustrated in fig. 2.9. Below, the effects included in the digitization are briefly described. Details on the digitization can be found in [100].

The effects of the readout electronics are emulated by modeling the time constants of the slow and fast shaper of the readout chip. This means that all simulated hits in a channel are integrated in a 50 ns time window.

Next, the single channel hit energy output in GeV needs to be transformed to the common energy scale of MIPs. This is done by a linear conversion factor ( $MIP2GeV$  factor), which is determined by simulated muons of 120 GeV. The hit energy distribution is fitted around the mode of the distribution with the convolution of a landau with a gaussian function. The most probable value of this fit is declared to represent 1 MIP. As for test beam data, a 0.5 MIP cut is applied in order to reject noise.

The statistics involved in the number of fired pixels of the SiPMs are implemented in the digitization. The number of fired pixels is modified by a poissonian smearing, which is important especially for low energetic signals. The number of theoretically fired pixels is calculated from the simulated hit energy in MIPs using the gain and MIP calibration constants as well as the inter-calibration (together representing the light yield of the channel) following

eq. (2.4). For large hit energies, the saturation of the SiPMs is implemented according to eq. (2.3).

For the PTP some of the tiles are not wrapped with reflective foil and thus optical crosstalk between the scintillating tiles has to be taken into account. A value of 12 % crosstalk for layers without wrapping are used according to [86]. Furthermore, dead channels or channels without calibration constants are ignored in the simulation.

The procedure for a proper digitization of the hit time measurements is described separately for the presented analyses in section 4.4 and section 7.3. After digitization, simulated data and test beam data are processed by the same reconstruction pipeline.

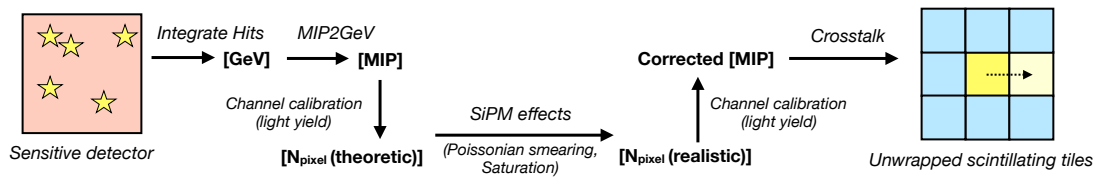


**Figure 2.9** – Digitization procedure of simulated data. Details about the different steps are given in the text.



## **Part II**

# **Time Analysis**



# Introduction and Overview

In the second part of this thesis a hit time calibration scheme for the AHCAL is developed. Furthermore, the time structure of hadronic showers is analyzed and compared to simulated data. The data used throughout this part of the thesis was taken at the August 2015 test beam campaign at the SPS (CERN) with the partially equipped technological prototype (PTP) in a tungsten absorber stack.

Tungsten as an absorber material in calorimeters is of interest because of its high density, allowing for more compact calorimeters and could be an option for example at CLIC, where high energies are reached. For analyzing the time structure of hadronic showers, tungsten is also an interesting absorber material to study. The high atomic mass of the tungsten nuclei leads to the generation of many slow neutrons during the spallation processes. For the T3B experiment, about six times as many hits between 100 to 200 ns were observed with a tungsten absorber compared to a steel absorber (see fig. 1.8 and [16]). The T3B experiment was operated in parallel to the AHCAL physics prototype and was consisting of 15 scintillating tiles placed in a strip behind the physics prototype. With the timing capabilities of the PTP the hit times can be measured with every channel of the calorimeter prototype.

The timing capabilities of the AHCAL technological prototype were first demonstrated in a test beam campaign in 2012 operating a full AHCAL layer [80, 101]. In [50] a time analysis of the July 2015 test beam campaign with the PTP in a steel absorber stack is presented. Compared to their analysis, the time calibration procedure described in this thesis (chapter 4) includes a novel strategy for the extraction of the pedestal and slope parameters.

This thesis presents the first analysis of the data obtained in the August 2015 test beam campaign. After a detailed description of the experimental setup in section 3.1, the event selection procedure is explained in section 3.2 and section 3.3. In section 3.4, the simulation geometry is validated and the simulated hadronic showers are compared to the test beam data. The results of the time calibration are evaluated in section 4.3 and the time resolution for a muon beam is shown in section 4.4. In chapter 5, the time resolution of electromagnetic showers is compared to MC simulations. A correction for electronic effects is applied to the test beam data and an additional smearing is imposed on the simulated data. Finally, the analysis of the time structure of hadronic showers is presented in chapter 6 and compared to simulations.



## Chapter 3

# Data Preparation

In order to make use of the available data, several data preparation steps are conducted: 1. Event building and hit energy reconstruction are performed; 2. malfunctioning and noisy channels, chips or even layers are identified and rejected for further analysis; 3. non-beam events are identified and rejected; 4. cuts on global event variables are applied in order to discriminate several particle types and to create pure data samples; 5. the MC simulation is tuned and validated against the data. These steps are described in detail in the following, after a description of the experimental setup.

### 3.1 Experimental Setup

The experimental setup of the PTP consisted of 15 active layers in a tungsten absorber stack with 40 equally spaced absorber layers of 10 mm tungsten and 0.5 mm steel support [99, 102]. The first three active layers were single Ecal Base Units (EBUs) with scintillator strips of  $4.5 \times 0.5 \times 0.2 \text{ cm}^3$  instrumented by Hamamatsu MPPCs. The first EBU layer was placed in front of the first tungsten absorber. For the presented analysis, the EBU data is not considered. Eight layers of single HBU layers with  $3 \times 3 \times 0.3 \text{ cm}^3$  scintillator tiles were placed behind the EBUs. Furthermore, four big layers consisting of four HBUs each, were placed with an increased number of empty absorber slots after the single HBU layers. Depending on the layer, scintillator tiles with and without wavelength shifting fibers, as well as different SiPMs were used. The hadronic interaction length of a layer (active layer plus absorber layer) is  $0.129\lambda_I$ . For the last large layer the material in front is in total equivalent to  $4.0\lambda_I$ . A picture of the test beam setup as well as a schematic drawing are shown in fig. 3.1. A detailed list of the configuration of active layers can be found in appendix A.1.

Two small and one large trigger scintillators were placed in front of the AHCAL and one large trigger scintillator was placed behind the AHCAL. Additionally, a Cherenkov detector was used in the beam line for particle identification. The coincidence signal of the small trigger scintillators is used to validate events and as a time reference. In order to integrate

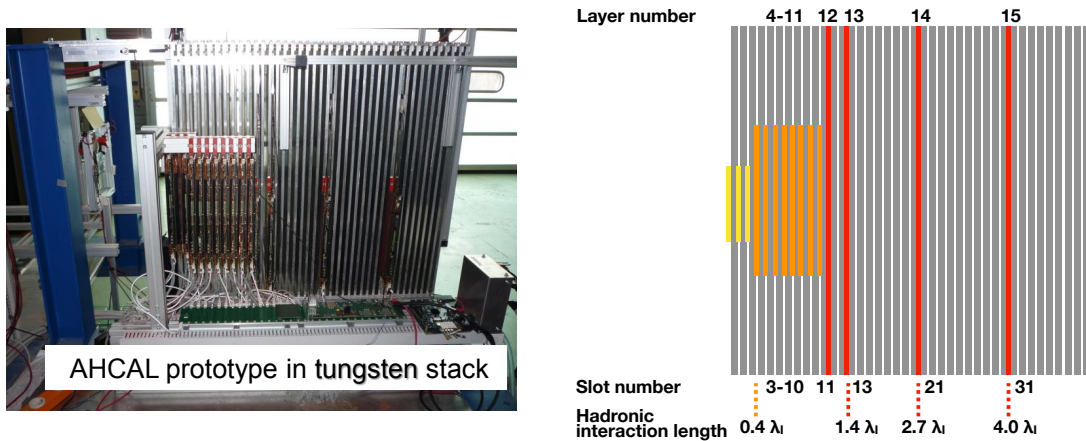


**Figure 3.1** – *Left:* Test beam setup of the AHCAL PTP in the tungsten absorber stack. *Right:* Schematic drawing of the setup. The tungsten absorber layers are shown in grey. The first three layers (yellow) are the EBUs, followed by the eight single HBU layers (orange). The four large layers (red) are placed in absorber slots 11, 13, 21 and 31. In addition to the layer number, the slot numbers and the equivalent of the hadronic interaction length  $\lambda_I$  in front of selected layers are given.

the time reference into the DAQ chain, six of the channels in the outer part of the large HBUs were used to read out the coincidence signal of the PMTs instrumenting the trigger scintillators, instead of the SiPMs. These channels are called  $T_0$ -channels. Initially there were six  $T_0$ -channels foreseen. For the test beam campaign that is discussed in this thesis, only two of them were working. For later test beam campaigns of the AHCAL a special board was used for the purpose of the reference time, which was not yet available for the campaign discussed in this part.

Data of 120 GeV muons, 20 GeV positrons as well as 10, 30, 50, 70 and 90 GeV positively charged pions is analyzed. The beam polarity during the test beam campaign was positive. Throughout this analysis, the term electron is used for positrons as well. Furthermore, the explicit charge of the pions and muons is omitted.

In addition to the test beam data, simulated data for the same energies were produced. The detector model is described in section 2.5.1, and for the digitization the procedure presented in section 2.5.2 is applied. For the MC simulations the QGSP\_BERT\_HP physics list was used for muons, electrons and pions, if not stated otherwise.

## 3.2 Pre-Selection

The pre-selection includes the selection of valid events by the event trigger as well as rejection of non-working channels and chips. On hit level, a 0.5 MIP cut is applied for suppressing noise hits.

### 3.2.1 Event Validation by $T_0$ Trigger

The  $T_0$ -channels, representing the coincidence of two of the trigger scintillators in front of the AHCAL, are used for the validation of events. Initially six of those channels were foreseen. For the test beam campaign in July three of them were still working [50, 86]. For this analysis one additional  $T_0$ -channel showed problems with the TDC (see chapter 5) and is thus excluded throughout the analysis. An overview of the status of the six  $T_0$ -channels is provided in table A.2

An amplitude cut on the  $T_0$ -signals is applied in order to reduce noise in these channels. The voltage ramps of the SPIROC chips was measured in the test beam mode to last for 3920 ns. During this analysis,  $T_0$ -hits are only accepted if they are in the time range of 500 to 3500 ns after the start of the voltage ramps. This is done in order to avoid edge effects of the TDC influencing the reference time as seen in the TDC-spectrum in fig. 4.1 (*left*) and further explained in section 4.1. For pion samples, this cut is extended to the range 500 to 2500 ns, making sure that late energy depositions up to 1000 ns after the reference time are included in the events. An event is declared valid if it has accepted hits in both  $T_0$ -channels that are within 5 ns (after time calibration, see section 4.1).

### 3.2.2 Channel, Chip and Layer Rejections

Several channels, chips, or whole layers are rejected throughout the analysis. First, any dead or noisy channels are excluded as well as channels for which any calibration constant could not be determined. In total 432 out of 3456 channels are affected by this. Module 11 shows inefficiencies in many channels (see section 3.4.1). As a consequence this module is excluded throughout the whole analysis, increasing the number of rejected channels to 513.

The modules in layers 5 and 6 are equipped with SiPMs with 12'000 pixels. For operation of these modules, the electronics settings had to be at critical values. For the occupancy correction described in chapter 5 these modules showed an especially bad behavior and are hence excluded throughout the timing analysis. Module 12 was found to show bad TDC spectra and is thus excluded throughout the timing analysis as well. Additionally, the chips in the corner of the big layers have very low statistics for the time calibration and are therefore not considered for the time analysis. In total 1792 channels are considered for the time analysis.

## 3.3 Event Selection

Events that involve two particles from the beam are rejected by identifying hit clusters in the time dimension based on the AHCAL time information. This procedure is explained in detail in section 6.1.

Several cuts are applied to discriminate different particle types. For Muons, a track

**Table 3.1** – List of cuts for different particle beams and beam energies. The CoG- $z$  cuts are given in mm. Additionally the number of accepted events after the selection is shown.

Beam	Energy	> Hits	< Hits	> $\overline{\text{Hit-z}}$	< $\overline{\text{Hit-z}}$	Track	Cher.	# Evt.
Muon	120 GeV	—	20	—	—	✓	—	182 000
Positron	20 GeV	16	60	—	130 mm	—	✓	68 200
Pion	10 GeV	16	—	120 mm	—	—	✓	15 900
Pion	30 GeV	18	—	130 mm	—	—	✓	60 500
Pion	50 GeV	20	—	150 mm	—	—	✓	80 700
Pion	70 GeV	20	—	170 mm	—	—	✓	102 200
Pion	90 GeV	20	—	180 mm	—	—	✓	80 400

(defined as a straight line of hits) is required and a maximum of 20 hits are allowed to ensure non-showering particles. The number of hits distribution is very powerful in discriminating between muons and other particles (see fig. 3.2a and fig. 3.2b). However, it is not possible to efficiently distinguish electrons from hadrons. This can be achieved by exploiting the position of the shower, as hadrons are expected to shower deeper in the calorimeter than electrons. For this the mean hit position in  $z$ -direction is used as a discriminative variable (see fig. 3.2c and fig. 3.2d). In fig. 3.3 the two dimensional distribution for the number of hits versus the mean hit position in  $z$ -direction is shown for electrons and pions before and after the selection. For higher energies, the distinction power of the variables increases. Because only 20 GeV electron data is available, the pion samples could not directly be compared with an electron beam of the same energy.

A Cherenkov threshold counter was present in the beam line. As the positive pion beam is expected to contain a significant amount of proton contamination, the pressure on the Cherenkov detector was selected for the pion beam such that it separates pions from protons. For electrons a hit in the Cherenkov detector is required as well in order to discriminate against heavier particles. A detailed list of cuts for different particle beams and beam energies is given in table 3.1.

For pion beams the cut on the required Cherenkov signal rejects 30 to 50 % of validated events, more for increasing energies. For positron beams about 25 % of the events are rejected because of a missing Cherenkov signal. The efficiency of the Cherenkov detector is not known precisely but estimated to be around 70 % [103] which would fit with the observed rejection numbers for positrons and low energetic pion beam for low contaminations. For 10 GeV pions 50 % of the Cherenkov validated events are rejected by the additional cuts. In this case, most events get rejected by the required minimum of 16 hits, as low energetic pions produce only few hits. For higher energetic pion beam the acceptance increases significantly. For 70 GeV pions only 15 % of the events get rejected after the Cherenkov cut, which are mostly muon, or pion events without a hard interaction (punch through pions). The acceptance for simulation events is comparable to data after the Cherenkov cut.

Because muons can be rejected very efficiently, no contamination of muons is expected in the electron or pion samples. Additionally, the muon beam is expected to be free from contamination of electrons or hadrons (see fig. 3.3a). In order to estimate the contamination of hadrons in the electron sample and electrons in the hadron sample we look at the respective event selection purities on simulated data. For a simulated 30 GeV positron beam about 3 % of the particles get selected by the 30 GeV pion selection criterion. Vice versa, for 30 GeV of simulated pions, about 1 % get selected by the positron selection cuts. It can be estimated in fig. 3.2c that before the event selection, the beam contamination is smaller

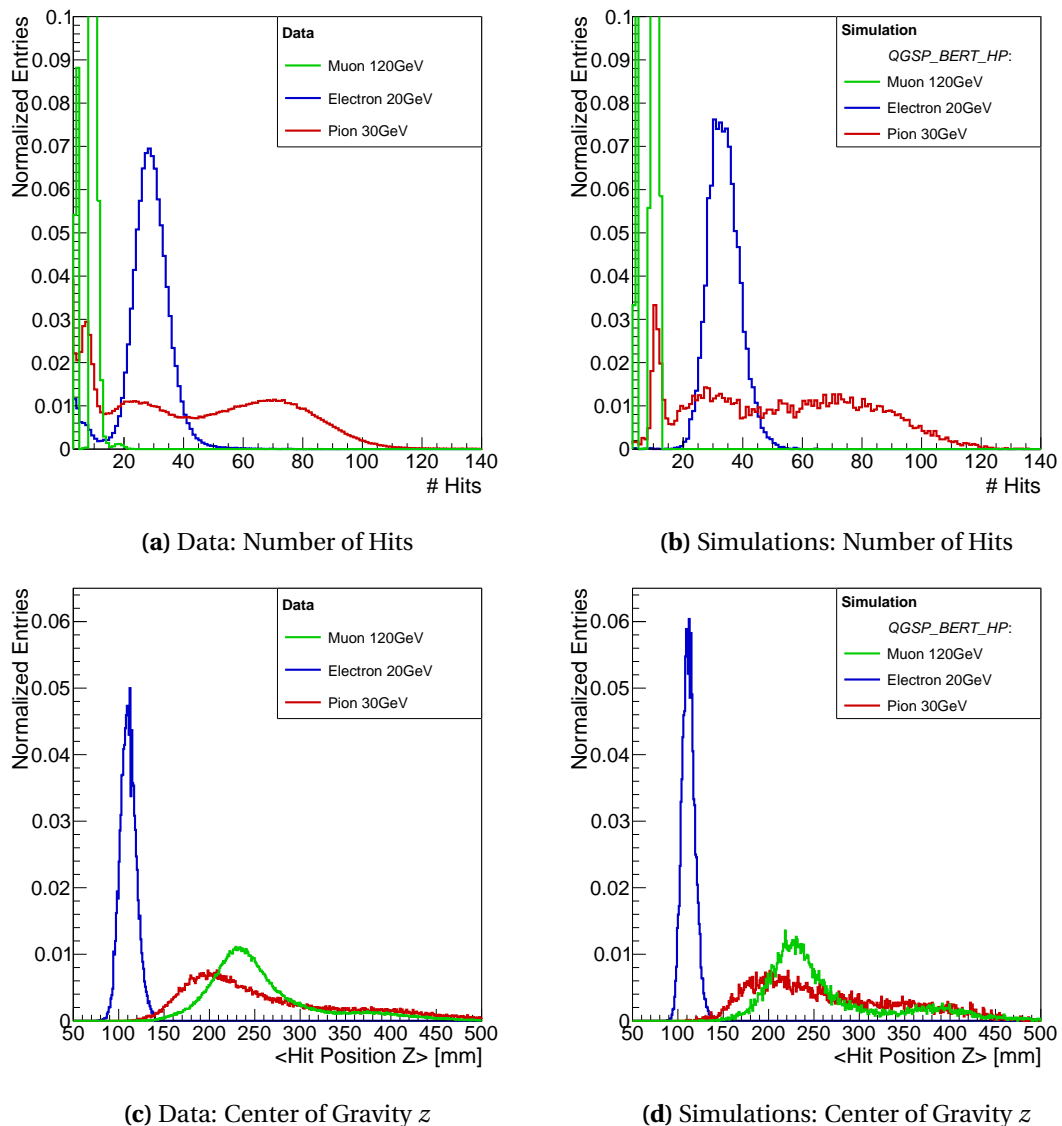


**Figure 3.2** – Number of hit distribution (*top*) and the distribution of the hit position in  $z$ -direction (*bottom*) for data (a), (c) and MC simulation with QGSP\_BERT\_HP physics list (b), (d). Plots shown for 120 GeV Muons, 20 GeV electrons as well as 30 GeV pions. The data is shown without event selection.

than 1 %. Together with the estimated selection purities the total contamination in the data samples after event selection is expected to be well below 1 in 1000.

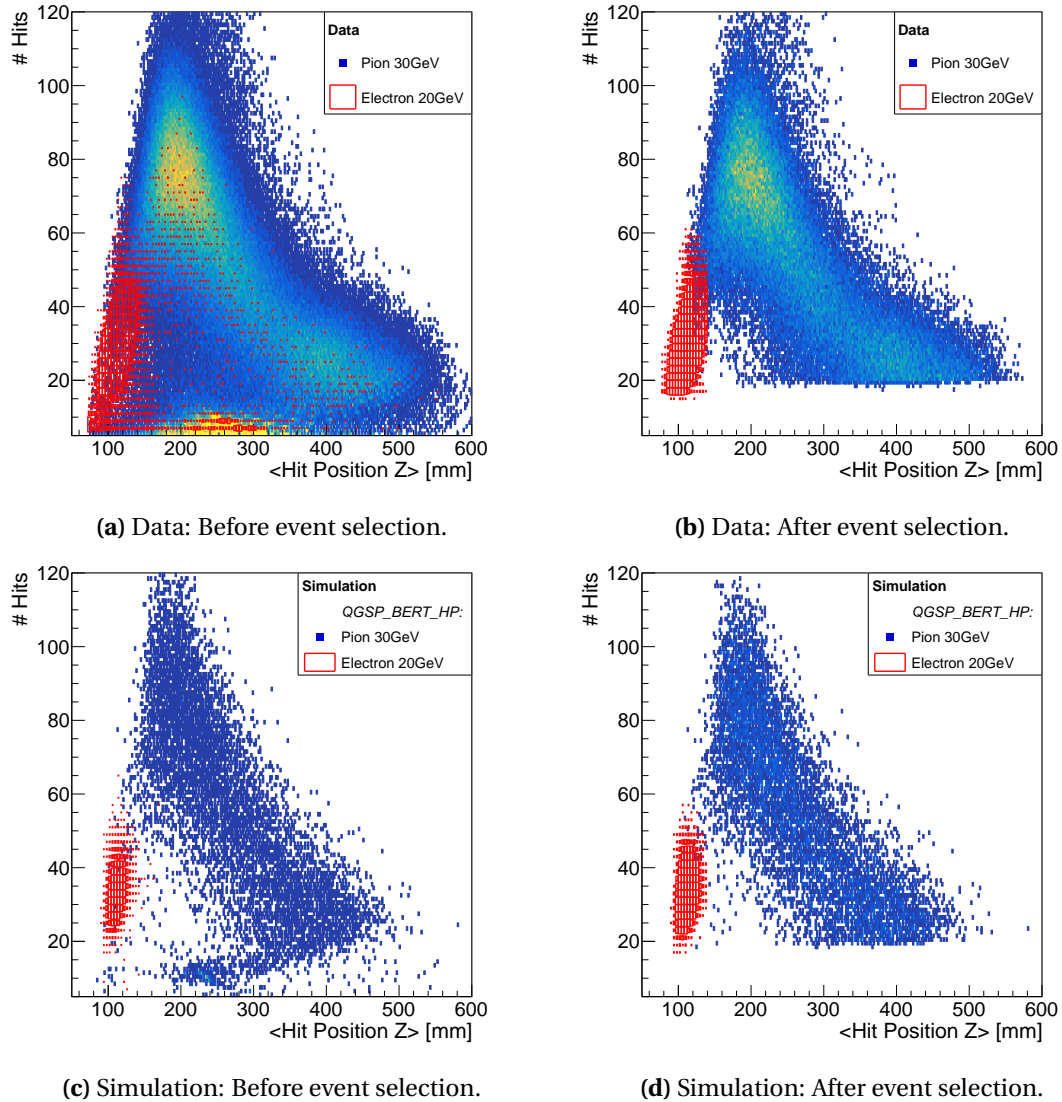


**Figure 3.3** – Number of hits over mean hit position in  $z$ -direction for data (a)/(b) and simulation (c)/(d) of 30 GeV pions and 20 GeV electrons before and after event selection. The pion data is shown with a color scale from blue to yellow, while the magnitude of the electron samples are indicated by the size of the red rectangulars. For data, the electron beam shows a clear hadron contamination. Both data sets have a significant contribution by muons or muon-like punch-through particles. After the event selection, the contamination of other particles is significantly reduced for both data sets.

## 3.4 Simulation Validation

In this section data and simulation distributions are compared. Of special interest are the geometric validation of the simulation model as well as the beam line model and the beam smearing parameters. Furthermore, the hit energies and the shower shapes will be compared and discussed.

### 3.4.1 Geometry Validation

A good cross-check of the consistency of the simulation model with the real world test beam setup is to investigate the distribution of hit positions for muon data as shown in fig. 3.4. No selection is applied to the data shown in this figure. It can be seen that the layers and tiles are at consistent  $z$ - and  $x$ -positions. For the  $z$ -position, the data and the simulation distributions are in reasonable agreement. Because of the relatively large number of excluded channels, this distribution is very prone to differences in the beam smearing. The largest deviations occur for layer 11, which is one of the malfunctioning layers that was excluded for further analysis. Significant deviations of about 15 % are also observed for layer 8. This may be due to inefficiencies of the detector in that layer. As the deviations are not too large, this layer is kept during the analysis. For the  $x$ -positions deviations of data and simulation are larger. This can be explained by an insufficient beam smearing for the muon beam in the simulation. As the muon beam smearing is not affecting the following analysis, it is not further investigated.

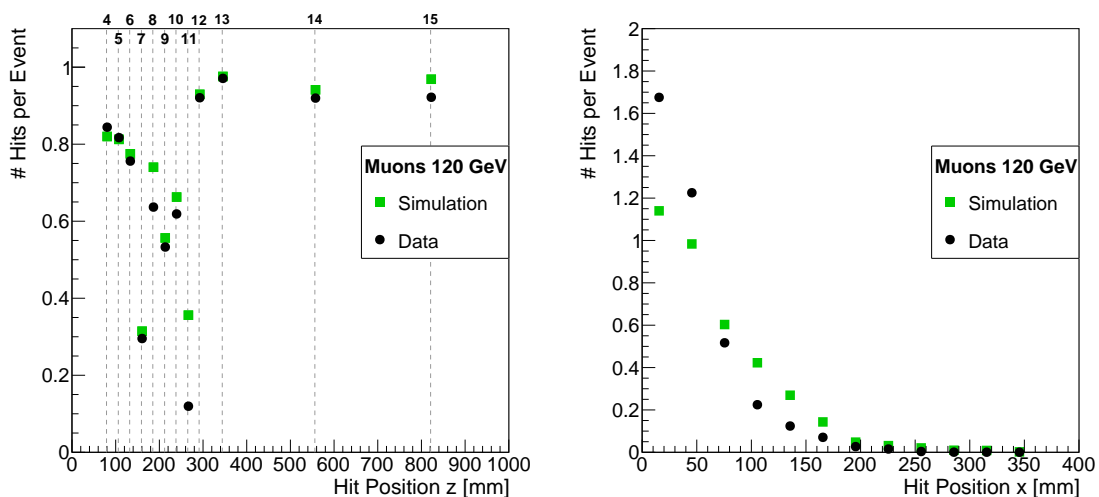


**Figure 3.4** – Distributions of hit positions for 120 GeV muon beam. *Left*:  $z$ -direction along the beam line. The position of the layers is drawn in broken lines with the corresponding layer number at the top. *Right*: Distribution of the hit position in  $x$ -direction. The distribution in  $y$ -direction looks similar and is therefore not shown.

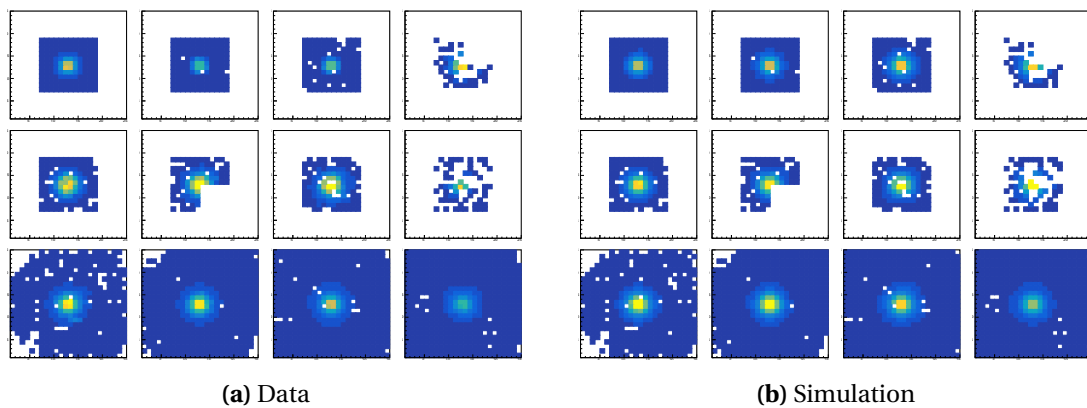
### 3.4.2 Beam Line and Beam Properties

The test beam campaign in August 2015 was performed at the H6 beamline [104] at the SPS at CERN. Upstream of the AHCAL, a Cherenkov detector, a large ( $500 \times 500$  mm) and a small ( $100 \times 100$  mm) scintillator were present in the beam line. These elements are as well implemented in the detector geometry of the simulations.

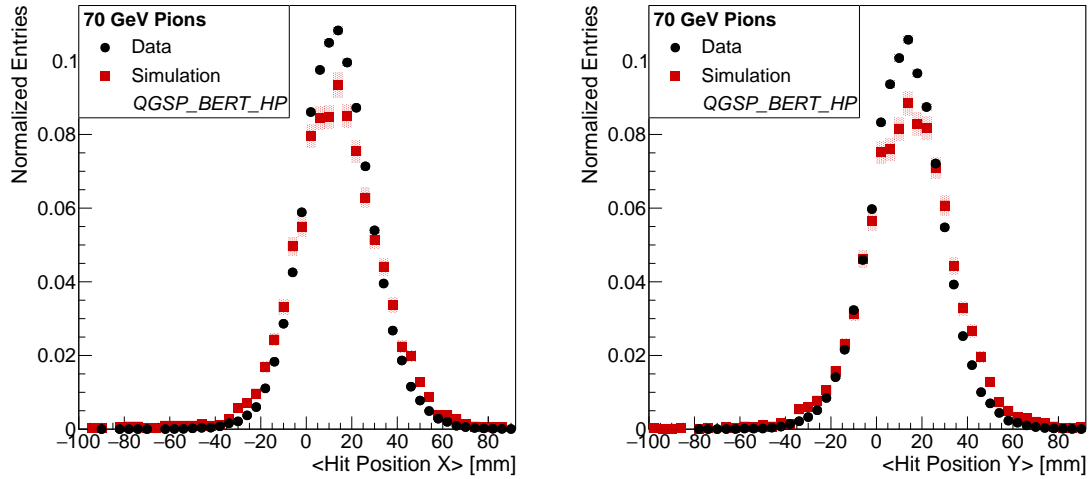
The beam smearing is estimated empirically. For electrons a beam smearing of 15 mm in  $x$ - and  $y$ -direction is used. For pions this value is increased to 20 mm. The particle source is located at a distance of 100 m to the detector. An additional radial smearing of 0.01 deg is applied.

Figure 3.5 shows hitmaps for all twelve layers for 70 GeV pion beam data and simulated data. There are no significant differences visible regarding the distribution of hits across the detector. This can be checked in more detail by comparing the distribution of the mean hit position in  $x$ - and  $y$ -direction between data and simulations as shown in fig. 3.6.

The mean hit position in  $z$ -direction for electrons (shown in fig. 3.7) is very sensitive to the material budget in the beam line, as this may lead to electrons showering early. It can be seen that this indeed may be the case for the studied data set. The mean hit position for data events has a tail to the left. For the simulated data of the July 2015 test beam campaign, this issue was solved by adding an extra plate of steel in front of the detector and optimizing its thickness by empirically matching the shape of the  $z$ -position distributions [86]. The effect is much less severe for the hadron beam, which is of main interest in this study. Thus, no extra material is added to the beam line.



**Figure 3.5** – Hitmaps for 70 GeV pions **(a)** data and **(b)** QGSP\_BERT\_HP MC simulation. Showing layers 4 to 15 from top left to bottom right. The color scale extends from blue (low number of hits) to yellow (high number of hits).



**Figure 3.6** – Mean hit position in  $x$ -direction (*left*) and  $y$ -direction (*right*) for 70 GeV pions data and QGSP\_BERT\_HP MC simulation.

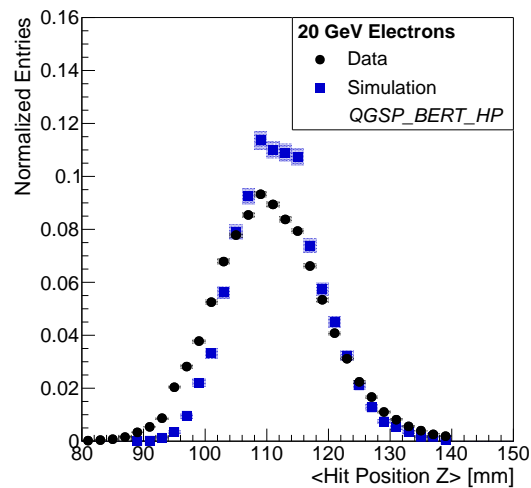


**Figure 3.7** – Mean hit position in  $z$ -direction for electrons compared to MC simulations.

### 3.4.3 Hit Energy Reconstruction

The energy reconstruction of hits is done following the standard procedure as described in section 2.4. For the hit energy reconstruction, the calibration constants determined for the July 2015 data set [86] are used. The calibration constants should not depend on the absorber material. However, differences may occur due to different settings (e.g., bias voltage of SiPMs) and environment temperature. Figure 3.8 shows the single hit energy in MIPs for muon beam and for electron beam. Even though the calibration constants were determined during the test beam campaign in July 2015 with a steel absorber stack, the precision of the energy reconstruction is satisfactory. For the muon beam, the MIP distribution peaks roughly at 0.95 MIP. The MIP to GeV factor in the digitization of MC simulation is tuned in such a way that the MIP distributions of data and simulation are in agreement for muons. It is determined to be:

$$C_{\text{MIP}2\text{GeV}} = 0.5200 \text{ MeV/MIP}. \quad (3.1)$$

As the lower part of the hit spectrum of muons is more sensitive to the pedestal and MIP calibration, the accuracy of the saturation and high-gain low-gain inter-calibration (see section 2.4.2) can be seen at the higher end of the electron's single hit spectrum. As the saturation correction is dependent on the hardware of the SiPMs, which has not changed between the July and August 2015 test beam campaigns, it is expected to be the same. The high-gain low-gain inter-calibration, however, depends on chip settings and is likely the reason for the observed differences between data and simulations in fig. 3.8 (*right*): Data is lacking hits especially in the region between 20 to 80 MIP. The analysis therefore relies as little as possible on variables related to the hit energy and instead uses variables related to the space and time distributions of hits.

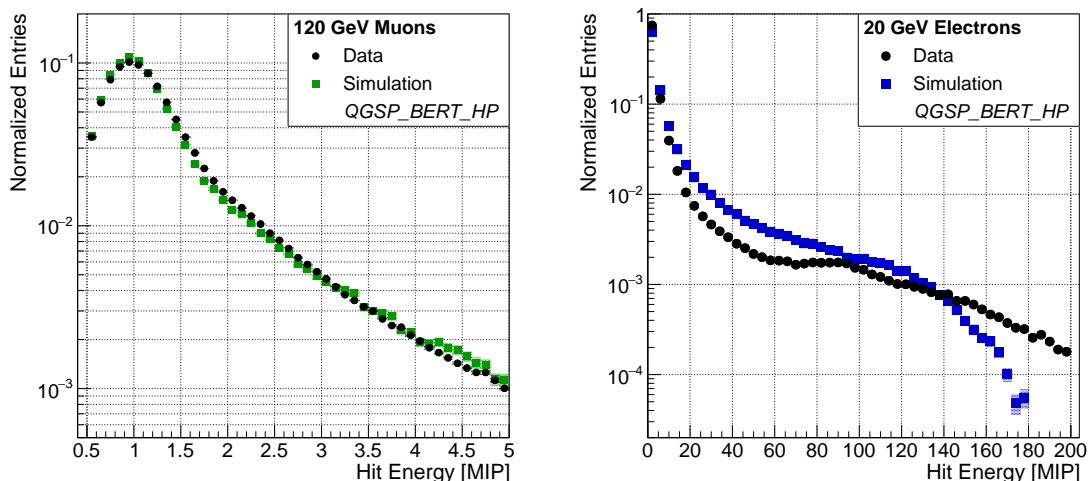


**Figure 3.8** – Single hit spectra for muon (*left*) and electron (*right*) beam compared to simulations.

### 3.4.4 Shower Simulation Validation

This section will evaluate the agreement in shower variables between data and simulation for hadron showers. Most characteristic for a hadron shower are the lateral and longitudinal shower development as well as the overall particle multiplicity in the shower.

Figure 3.9a shows the distribution of the number of hits per event. The total number of hits in each event is in good agreement between data and the simulations for all three physics lists. The double peak structure arises from the special geometry of the detector with the non-homogeneous spacing between the active layers in the back of the detector. Events that have their shower start deeper in the detector are mostly located in the on the left of the distribution with lower hit numbers, because of the lower longitudinal sampling in this part of the detector. The second peak with higher total hit numbers mainly consists of pions that shower early and hence have many hits in the first layers. The main difference between data and simulations arises for the middle and high number of hits. While the test beam data contains slightly more events with many hits, there are fewer events with an intermediate number of hits. In fig. 3.9b it can be seen that differences between test beam data and simulations mainly occur in five layers: layers 5 and 6 show fewer hits in data, while layers 8, 9 and 10 have more hits in data. For layers 5 and 6 it is likely that the lack of hits is related to the problems in these layers for high chip occupancies (see chapter 5). The number of hits is roughly halved in these two layers with respect to the simulation, while this problem is not observed for muon beam (fig. 3.4 *left*).

Figure 3.9c shows the lateral distribution of hits. The hit radius  $r$  is defined as the distance in  $x$ - and  $y$ -position of the hit to the mean position  $(\bar{x}, \bar{y})$  of all hits in that event:

$$r = \sqrt{(x - \bar{x})^2 + (y - \bar{y})^2}. \quad (3.2)$$

The distribution of hits of test beam data is in good agreement with all considered physics lists. Smaller deviations can be observed in the inner part of the shower, where hits in data are distributed a little more to the outside.

The longitudinal distribution of hits, the mean hit position in  $z$ -direction, is presented in fig. 3.9d. The shape of the distribution can again be explained by the special geometry of the prototype. Events located in the left half of the distribution shower rather early and have many hits in the first small layers, while the right half consists of events that shower later and thus reach the big layers located in the rear part of the detector. Discrepancies between data and simulation are especially apparent for events which shower later in the detector and have a high mean hit position in  $z$ . While the distribution falls off steeply for values around 500 mm in simulations, the distribution is smeared more towards higher values for test beam data. The events that are at the very right of the data distribution, exceeding the simulation distributions, are events that shower only right before the last two layers and have only few hits. The track in the layers before has a large influence on the mean hit position for

those events. For some events, the track is missing a few hits in the data sample because of inefficiencies not modeled in the simulations (e.g., small gap between tiles) and thus moving the mean hit position to higher  $z$ -values, which explains the discrepancy between data and simulations. In general, the QBBC physics list follows the data slightly better than the other two.

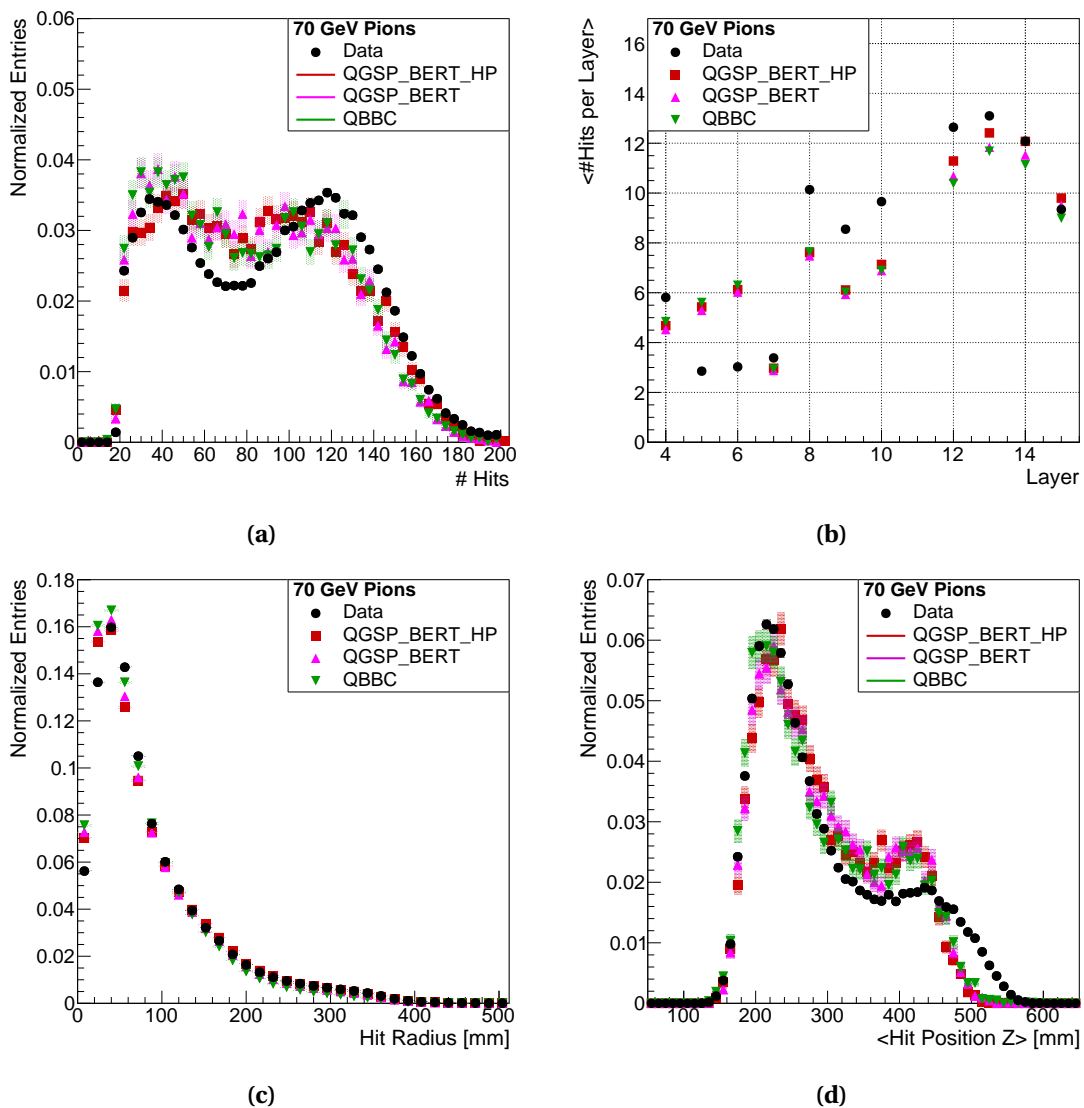


**Figure 3.9** – (a) Number of hits per event, (b) mean number of hits per layer, (c) hit radius and (d) mean hit position in  $z$ -direction for 70 GeV pions data compared to QGSP\_BERT\_HP, QGSP\_BERT and QBBC MC simulation.

### Pion-Proton Comparison

Because the pion beam at the H6 beam line for positive polarity is expected to have a significant contamination of protons, a Cherenkov counter was used during the test beam campaign in order to distinguish between pions and protons. The pressure in the Cherenkov detector was set in such a way that a signal in the Cherenkov detector indicates a pion event. The efficiency of the Cherenkov detector is estimated to be about 70 % [103].

In general, because of baryon number conservation, protons are expected to produce more heavy baryons in the first steps of the shower and thus fewer  $\pi_0 \rightarrow \gamma\gamma$  decays. This comes with an expected reduced electromagnetic content in the proton showers (see e.g. [105]). Furthermore, the nuclear interaction length for protons in tungsten (9.9 cm) is about 15 % smaller compared to the pion interaction length (11.3 cm). Thus, protons are expected to shower on average slightly earlier than pions.

Figure 3.10 shows the number of hits per event, the mean number of hits per layer, the distribution of the mean hit position in  $z$ -direction and the hit radius for both data samples with and without a Cherenkov signal and compares it to pion and proton MC simulation. It can be clearly seen that for all distributions the data sample with a Cherenkov signal is in better agreement with the pion simulation, while the data sample without a Cherenkov signal follows the distribution of the simulated protons. The most striking difference is that protons are producing on average about 10 % more hits across all layers. Furthermore, for the pion sample more hits are located close to the shower axis. These results are expected because of the aforementioned suppression of the electromagnetic content for protons. The mean hit position in  $z$ -direction is shifted to lower values for the proton sample, which is expected for a reduced interaction length of the protons. Similar effects were observed for a steel absorber in [72].

The differences between pion and proton sample are more striking for simulated data due to the inefficiency of the Cherenkov detector that affects only the test beam data. While the samples in simulation are perfectly pure, the proton sample from test beam data is expected to contain a significant amount of pion events. The pion sample, on the contrary, is expected to be mostly clean of proton events.

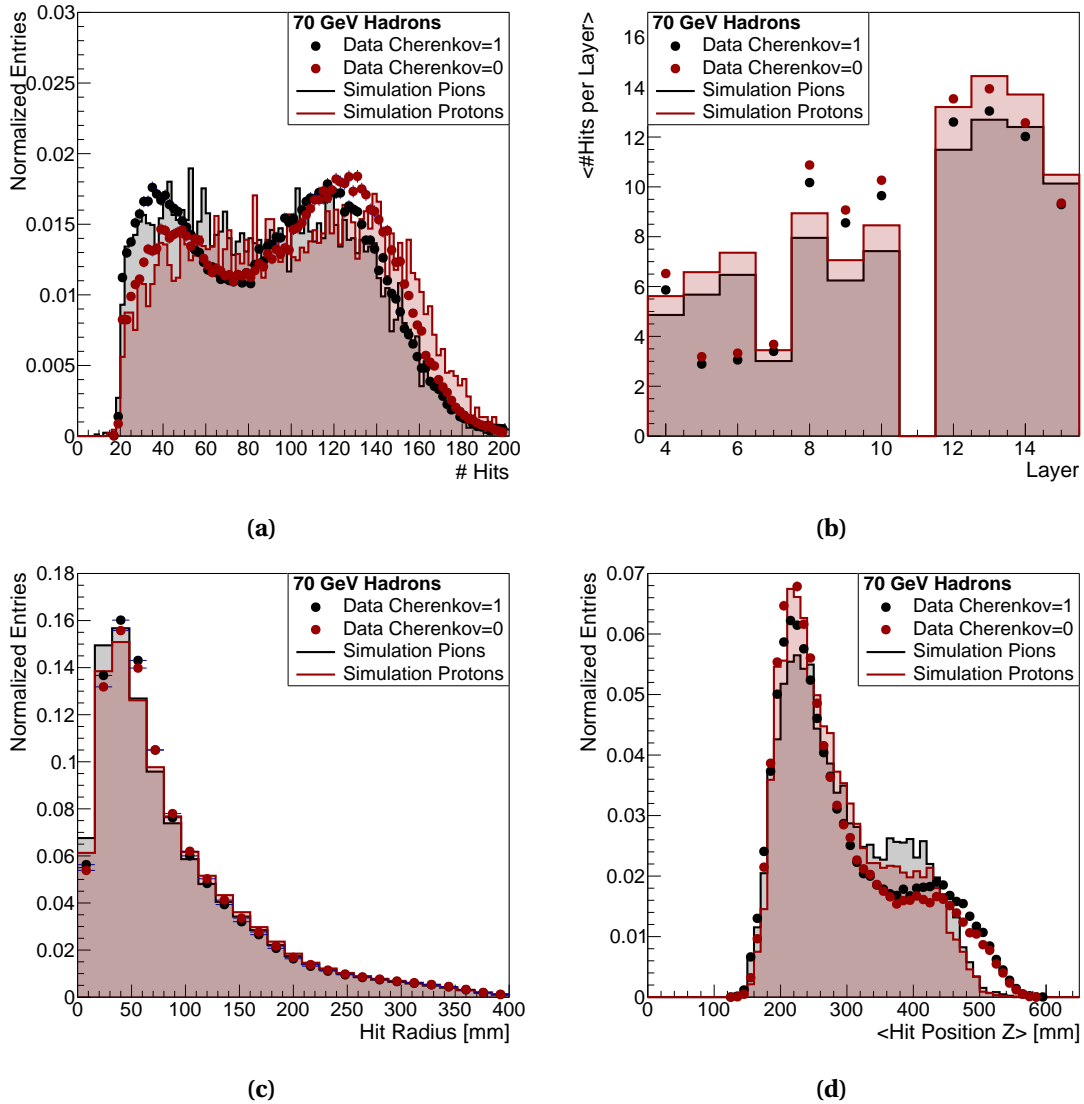


**Figure 3.10** – (a) Number of hits per event, (b) mean number of hits per layer, (c) hit radius and (d) mean hit position in  $z$ -direction for 70 GeV pion beam data with Cherenkov signal and without compared to QGSP\_BERT\_HP MC simulation of pions and protons.

## Chapter 4

# Time Calibration

Time measurements with the CALICE AHCAL technological prototype are performed in the readout ASIC<sup>1</sup> by a voltage that is ramping up over time with a periodicity of 4  $\mu\text{s}$  (see section 2.3.1). Upon a hit, the current height of the ramp is stored in one of 16 memory cells and digitized by a 12-bit ADC to TDC values at the end of a read-out cycle. As the TDC may not be linear at the beginning and at the end of the ramp, events with the reference time between 500 to 3500 ns are selected in order to avoid edge effects.

For a time analysis with one layer of the AHCAL reported in [80], the calibration of the slopes and pedestals of the SPIROC ASIC were done by charge injection measurements in the lab. This procedure is not feasible for a large scale prototype. The aim of this chapter is to establish a high precision time calibration scheme for the AHCAL technological prototype using test beam data. In a first step the reference time given by the external trigger is calibrated. Afterwards, the hit times are converted from TDC values to nanoseconds and further corrections are applied. Each of these steps are described in this section in detail. As high energetic muons are expected to give quasi-instantaneous energy depositions in the scintillator, muons that go through the detector without the production of any shower are selected for calibration.

### 4.1 Calibration of the Reference Time

The  $T_0$ -channels defined in section 3.2.1 are used as a time reference. The calibration of the time reference is done in a similar way to [50]. The pedestal and the slope of the voltage ramps can be extracted from the TDC spectra (see e.g., fig. 4.1 *left*). The pedestal is given as the start of the spectrum and the slope can be calculated using the width of the spectrum and the time the ramp needs to reach its maximum (3920 ns for a ramp up time of 4  $\mu\text{s}$ , assuming

---

<sup>1</sup>SPIROC2b [106]

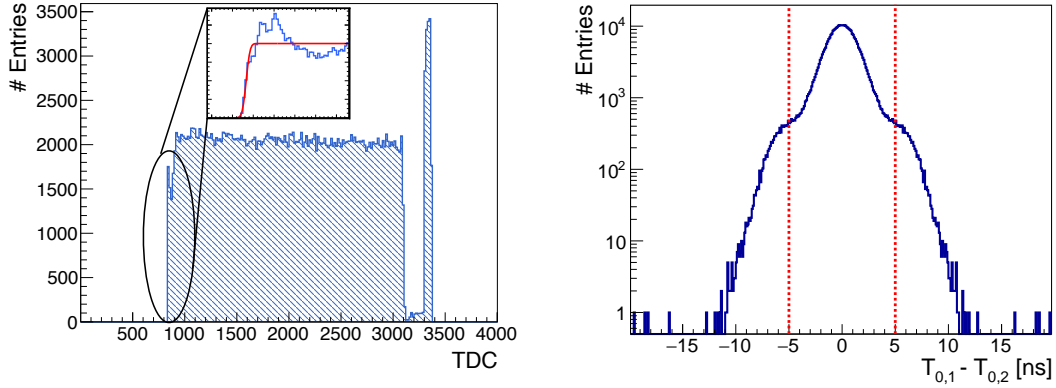


**Figure 4.1** – *Left*: TDC spectrum of a typical channel. The gap and the peak in the spectrum between 3000 to 3500 ns are due to a malfunction of the electronics. At the end of the TDC cycle, the validation is not working properly and all events are accepted leading to the peak, with a short period of no accepted events before, leading to the gap. *Right*: Distribution of differences between both  $T_0$ -channels. The red line marks the cut on the time difference

2% dead-time [107]):

$$\text{slope [ns / TDC]} = \frac{3920 \text{ ns}}{\max [\text{TDC}] - \text{pedestal} [\text{TDC}]} \quad (4.1)$$

The memory cells are analogue buffers and may differ in their pedestal values. Furthermore, there are two different TDC ramps operated in the SPIROC ASIC: one for even and one for odd bunch-crossing IDs (bxIDs) (see section 2.3.1). Thus, the pedestal is determined for each memory cell of the  $T_0$ -channels and separately for even and odd bxIDs. The TDC spectrum contains several features that are common to all channels: A small bump at the beginning of the spectrum arises due to distortions at the beginning of the TDC ramp, while the gap and the peak on the very end of the spectrum are the consequence of a problem with the validation signal near the end of the bunch crossing cycle. In order to enhance the precision of the extraction of the pedestal and to be less dependent on the varying shape of the rising edge, the rising edge of the TDC spectrum is fitted with a function of the form:

$$f(x) = \frac{a}{2} \cdot \left( 1 - \text{erf} \left[ \frac{(x-b)}{\sqrt{2} \cdot c} \right] \right), \quad (4.2)$$

with parameters  $a$ ,  $b$ ,  $c$ , and erf being the error function. The pedestal is given by the  $b$  parameter.

The slope is expected to be stable across the memory cells and the channels of one ASIC. Hence, for the slope, the average of all calculated slopes for all memory cells is taken as the slope value for this  $T_0$ -channel (separately for even and odd bxIDs). The time of the  $T_0$ -channels can now be calculated using the slope and the pedestal of the TDC ramp:

$$t_0[\text{ns}] = (\text{TDC} - \text{pedestal}) \cdot \text{slope}. \quad (4.3)$$

The time reference is calculated as the mean between both  $T_0$ -channels:

$$t_{\text{reference}} = \frac{t_{0,1} + t_{0,2}}{2}. \quad (4.4)$$

Figure 4.1 (*right*) shows the distribution of the differences between both  $T_0$ -channels. For an event to be declared as valid in the following, the event time reported by the two  $T_0$ -channels has to be within 5 ns. The time jitter between both  $T_0$ -channels after the cut is 1.8 ns.

### Linearity of the Reference Time

It is known that the TDC ramps of the SPIROC chip may not be completely linear [50, 79]. As the  $T_0$  channels are read out by AHCAL channels themselves, they also suffer from this effect. As there was no other time reference present in this test beam campaign, the exact linearity of the  $T_0$  channels cannot be verified. However, it is expected that they behave similar to the other channels. From measurements in the lab and at later test beam campaigns with an external time reference, it is shown that in general the non-linearity of the SPIROC TDC is limited to a few ns over the whole bunch crossing. Non-linearities of this size will have no significant impact on the presented results as they only introduce a small additional uncertainty if the hits are far apart (several 100 ns) in time.

## 4.2 Calibration of the Hit Time

After the  $T_0$ -channels are calibrated, each event is assigned a reference time in nanoseconds. The other channels could in principle be calibrated in the same scheme (as it is done for example in [50]). However, as we already have a calibrated time reference for each hit, the correlation between the hit's TDC value and the reference time can be used for each channel (and memory cell) (see e.g., fig. 4.2 *left*). In order to calibrate the channels, a linear fit between the hit's TDC values and its reference times is applied. The advantage of this method is a significant reduction in the amount of necessary hits in each channel for calibration and less dependence on features especially at the edges of the TDC spectrum.

For the time calibration an accuracy of about one ns is needed over a range of several thousand ns with as few data points as possible. Neglecting the non-linearities of the TDC ramps, the time calibration can be stated as a linear regression problem where the solution of the linear regression represents the slope of the TDC ramps. In the data there is a jitter on both the dependent and the explanatory variable. Moreover, noise is observed which is independent of the TDC ramp with large deviations. These outliers can have a large influence on the fitting results. Thus, to reach the necessary precision, a dedicated fitting procedure is necessary. This is done in four steps:

1. A robust fit taking 80 % of the hits into account is performed. To avoid edge effects, only the range from 1000 to 3000 TDCs is used. See discussion in section 4.2.1.

2. Every hit that differs from the prediction of the fit by more than 10 ns is ignored in subsequent fitting steps (outlier rejection).
3. As the slope of the TDC ramp is a feature of the ASIC and should be stable among channels, the average of all slopes of the first memory cells of all the channels in an ASIC is used as a fixed value for another linear fit that is performed for all memory cells.
4. The  $y$ -interception of this second fit is used as the offset value for each memory cell.

Again, even and odd bxIDs are treated separately. This procedure requires at least 30 hits in the corresponding memory cell and at most 1000 hits are considered. An example fit is shown in fig. 4.2 (*left*). The hit times are then calculated with respect to the  $T_0$ -reference time as:

$$t[\text{ns}] = \text{TDC} \cdot \text{Slope} [\text{ns}/\text{tdc}] + \text{Offset} [\text{ns}] - t_{\text{reference}}. \quad (4.5)$$

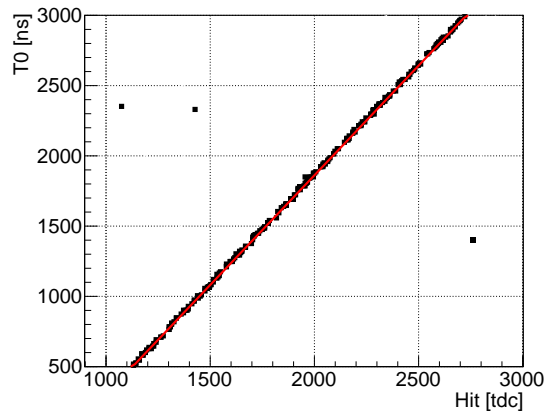


**Figure 4.2** – Linear fit between TDC values of hits and the reference time of the event shown for one representative channel.

#### 4.2.1 Determination of the Best Fitting Procedure

Because of the observed noise, a robust technique for fitting the ramps is necessary, such that single outliers are influencing the outcome of the calibration as little as possible. In order to test different fitting techniques, a toy MC simulation is set up. Data pairs are generated to simulate the TDC ramps using slopes of 1.6 ns/TDC and offsets of 1000 TDC. Random gaussian noise with zero mean and a standard deviation of 3 ns is added on the  $x$ -Axis (corresponding to the TDC value) and on the  $y$ -Axis (corresponding to the reference time). Additionally, 5 % of uniform noise are added over the whole range in order to simulate the outliers. The following fitting techniques are studied:

### Random Sample Consensus (RANSAC)

The RANSAC algorithm is an iterative technique that aims at finding model parameters which can explain a maximum number of *inliers*, while ignoring *outliers*. In a first step, a random subset of the data is chosen and the model parameters are fitted to this subset only. Second, the *consensus set* is determined, which is the set of data points of the total data that are within an error margin of the fitted model. The model with the largest consensus set after a fixed number of iterations is taken as the final model estimate [108]. The `Scipy` implementation of this algorithm is used [109].

### Least Trimmed Squares (LTS)

LTS is working on a subset of the whole data set with fixed size. The solution to the regression problem are the model parameters of a fit to the subset of the data that results in the minimum sum of the residuals between the data points and the prediction by this model [110]. The `ROOT` implementation of this algorithm is used [111] with a subset size of 80 % of the total data set.

### Theil-Sen Estimator

Another robust fitting technique is the Theil-Sen Estimator. It is defined as the median of the set of slopes through any two data points of the data set [112]. This method is stable for up to 30 % of outliers. The `Scipy` implementation of this algorithm is used [113].

## Results

The above mentioned fitting techniques are evaluated with respect to the mean absolute error on the slope and pedestal, averaged over 1000 pseudo-experiments. The number of data points for each fit was varied. The results can be seen in fig. 4.3. The Theil-Sen estimator and the LTS perform similar with the Theil-Sen estimator requiring slightly less data points to converge to high accuracy. The RANSAC algorithm performs significantly worse. The non-robust Ordinary Least Squares (OLS) estimator performs about two orders of magnitude worse in the given setting.

For the Theil-Sen and LTS algorithms the pedestal accuracy is on the order of 1 ns for at least 20 data points. For the slope parameter a reasonable accuracy of a few ps/TDC is reached for about 20 data points as well. Because of the slightly better performance on the slope parameter the LTS algorithm is chosen for the hit time calibration mentioned above. From fig. 4.3 it can be read that at least 30 hits in each memory cell are sufficient for a precise time calibration. Even though many other effects dominate the time resolution for this study, for most recent test beam campaigns much better resolutions are achieved using the same algorithm (see e.g., [114]).

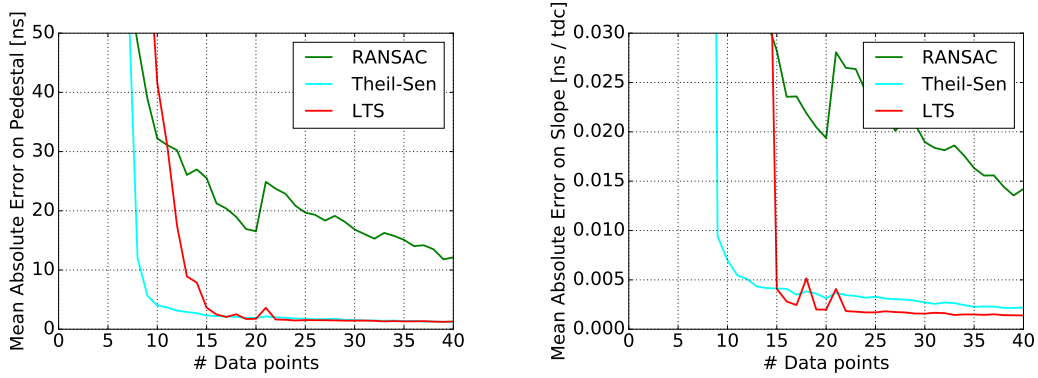


**Figure 4.3** – Comparison of several robust fitting techniques in terms of the mean absolute error on the pedestal ( $y$ -interception, *left*) and the slope of the TDC ramps (*right*).

#### 4.2.2 Non-Linearity Correction

As the TDC ramp may not be completely linear a phenomenological non-linearity correction is applied in a similar way to [50] using a 2<sup>nd</sup>-order polynomial fit. Figure 4.2 (*right*) shows the residuals of the linear fit for a representative channel together with the fit that is used for the non-linearity correction. The correction could be done in one step together with the time calibration by simply fitting a 2<sup>nd</sup>-order polynomial in the first place. Here, it is separated in two steps to better control the calibration and corrections.

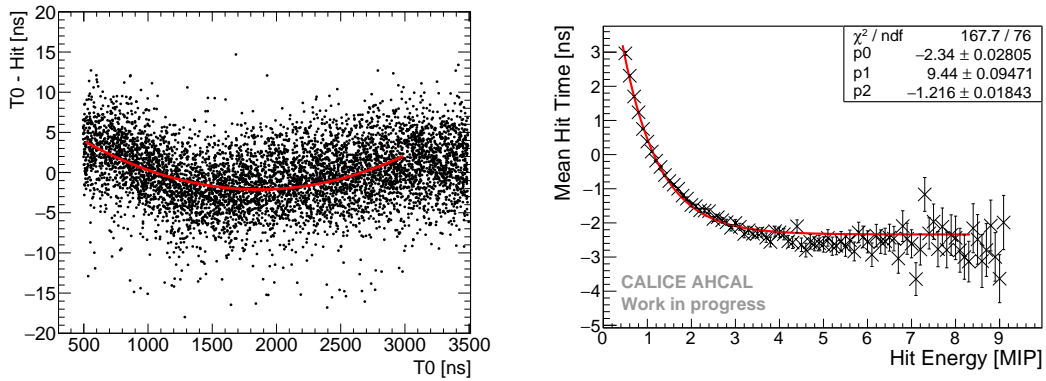


**Figure 4.4** – *Left*: 2<sup>nd</sup>-order polynomial fit to the residuals of the linear fit for the non-linearity correction. *Right*: Average hit time dependent on the hit energy. The distribution is fitted with an exponential function of the form:  $p_0 + p_1 \cdot e^{p_2 \cdot x}$ .

#### 4.2.3 Time Walk Correction

In order to correct for the fact that signals with a higher amplitude are expected to cross a constant threshold earlier than hits with a lower amplitude, a time walk correction is applied. The average hit time with respect to the hit energy is presented in fig. 4.4. The exponential fit

to the data is used as a correction of the hit time depending on the hit energy.

### 4.3 Evaluation of the Time Calibration

The offset and slope calibration constants are shown in fig. 4.5, separated for even and odd bxIDs. The distribution of slopes (fig. 4.5, *left*) is centered around 1.6 ns/tdc with minimum values of 1.35 ns/tdc and maximum values of 1.85 ns/tdc. The distribution is similar for even and odd bxIDs. Figure 4.5 (*right*) shows the distribution of offsets over all channels. The channels are ordered by the read-out chip they belong to, meaning that channels on the same chip are located next to each other in the figure with respect to the  $x$ -axis. Clusters of channels in the same chip can clearly be identified. The variations among chips are significantly larger than between channels in the same chip. On average the offset is about 1200 ns with a RMS of 110 ns.

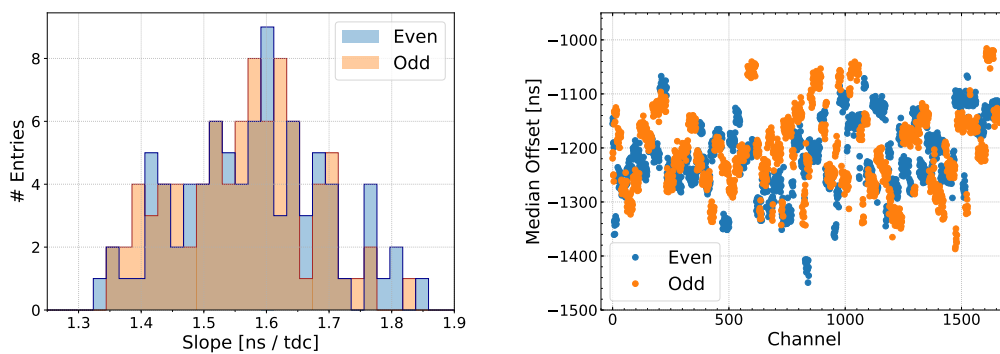


**Figure 4.5** – *Left*: Distribution of extracted slopes by the calibration procedure separated for even and odd bxIDs. *Right*: Median offset for each channel, again separated for even and odd bxIDs.

Within a channel the differences between the offset values of the different memory cells is on average about 5 ns (RMS). Between the first memory cell of all channels of the same chip, the deviations are on average 10 ns (RMS). Similar values were observed in laboratory measurements [80]. The corresponding distributions are shown in fig. 4.6. This shows the need of a calibration for each channel and memory cell, if nanosecond precision needs to be reached.

#### Non-Linearity Correction

Figure 4.7 shows the non-linearity correction evaluated at 2000 ns, about the middle of the TDC ramp. For most chips, the correction is below 1 ns. For some, however, the correction is a few ns. In general the non-linearity correction is small compared to the overall time resolution achieved in this analysis. Most channels show a less severe non-linearity than the

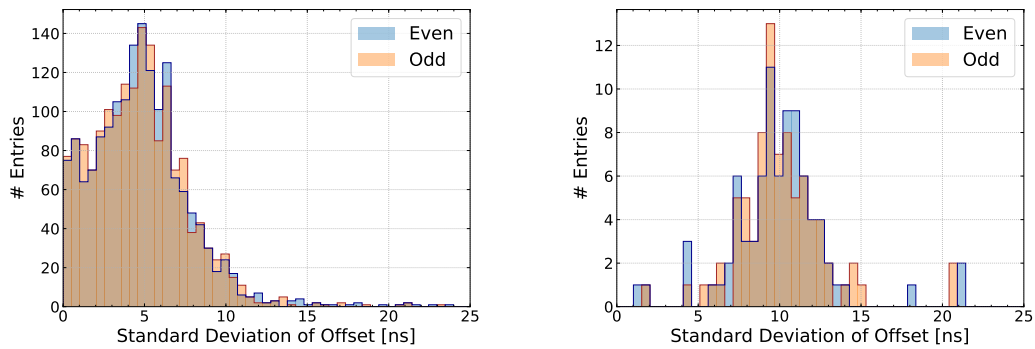


**Figure 4.6** – Variations of extracted offset values between memory cells in the same channel (*left*) and between channels in the same chip (*right*). Both distributions are shown separately for even and odd bxIDs.

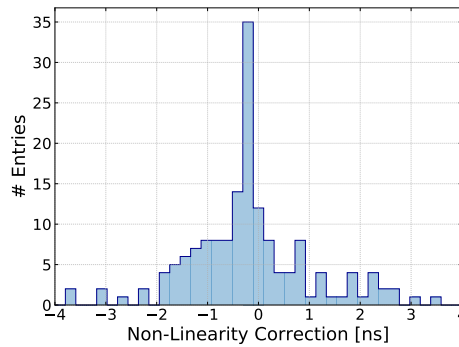


**Figure 4.7** – Non-linearity correction evaluated at 2000 ns for all chips.

example in fig. 4.2 (*right*). Thus, the impact on the results is limited. However, for test beam campaigns with a more precise time resolution it is a significant correction.

### 4.3.1 Handling of non-Calibrated Cells

Because the detector was not moveable for this test beam campaign and because of the limiting size of the trigger scintillator in front of the AHCAL, the channels in the outer part of the detector are significantly lacking hits, especially for higher memory cells. In total, with the given calibration, only 18 % of the memory cells could be calibrated individually. For 58 % of the channels, at least one memory cell is calibrated. Because of the lateral size of hadronic showers, excluding the non calibrated channels would significantly reduce the size of the pion data set, especially in the interesting outer part of the shower.

To recover as many channels as possible, the following procedure is applied: If the first memory cell of a given channel is calibrated, this offset value is used for all other memory cells in this channel without a calibration. The first memory cell has most hits in a channel

and thus is expected to give the most reliable reference offset for this channel. If a channel does not have calibration constants for the first memory cell, the average of the offsets of all other calibrated first memory cells in this chip is used. The expected uncertainty due to this procedure is about 5 ns for non-calibrated memory cells and about 10 ns for non-calibrated channels (see fig. 4.6 above). For non existing non-linearity corrections, no extrapolation is done and the non-linearity correction is skipped.

## 4.4 Muon Time Resolution

In this section the time resolution for Muons is analyzed. First, it is looked into the time resolution of single channels and chips in order to identify chips and channels with a particular bad time resolution.

### 4.4.1 Channel Dependent Time Resolution

The time resolution (defined as the RMS, in the interval  $[-50 \text{ ns}, 50 \text{ ns}]$ ) for a muon beam for each channel is summarized in fig. 4.8 (*left*). Most of the channels show a homogeneous time resolution between 5 to 7 ns. However, it can be clearly seen that channels located at the outer part of the big layers have a larger uncertainty in the time measurement. There are not many hits that can be used for calibration in those channels, the calibration has a higher uncertainty and the calibration constants have to be extrapolated for many channels as described above.

The same behavior becomes even more apparent by looking at the time resolution of whole chips as in fig. 4.8 (*right*). The chips are ordered in several subgroups. Chips located in the outer most part of the big layers have a significantly worse time resolution than chips located in the center of the detector. The chips located in the corner of the big layers have a particularly bad time resolution. It is apparent from this plot that most chips in layer 12 have a significantly worse time resolution. This was also observed in [50] and is probably due to wrong settings for the chips in this layer leading to bad TDC spectra. For the innermost chips, the time resolution is consistently about 6 ns.

Based on the results in fig. 4.8 (*right*), layer 12 and all chips that are located in the corner of the big layers are excluded for the time analysis. With this selection, the symmetry of the detector is preserved as much as possible, while at the same time excluding chips that perform worst by means of time measurements. After removal the chip with the largest RMS value is about 16 ns. The majority of remaining chips have an uncertainty in the time measurement of less than 10 ns.

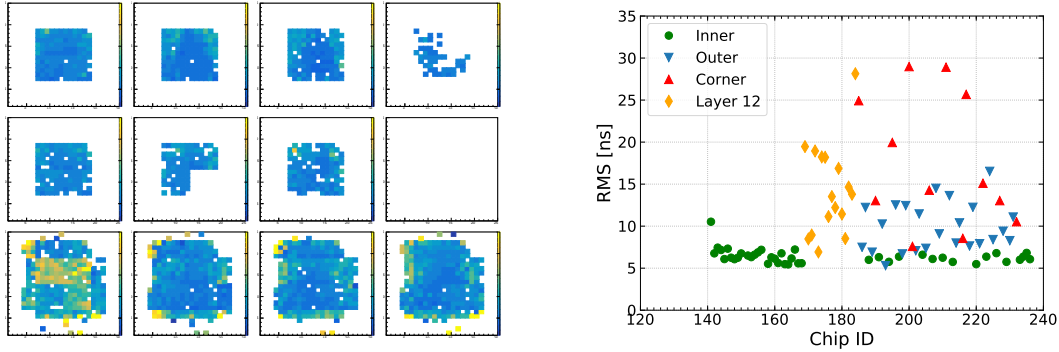


**Figure 4.8** – *Left*: Time resolution (RMS) for muon beam for each channel, ordered by the layer they are mounted on (layer 4-15 from top left to bottom right). The color scale ranges from 0 to 25 ns (blue to yellow). *Right*: Time resolution (RMS) for muon beam for each chip. The time resolution is defined as the RMS on the interval from  $-50$  to  $50$  ns. The different markers indicate different types of chips: The four innermost chips in each layer (green), chips, located at the outside of the big layers (blue), chips located in the corner of the big layers (red) and those on layer 12 (yellow).

#### 4.4.2 Total Time Resolution

The time distribution of muon hits after calibration in all remaining channels is shown in fig. 4.9. It is  $6.3$  ns (RMS, in the interval  $[-50$  ns,  $50$  ns]), or  $10.3$  ns FWHM.

The muon hit time distribution is used as an input for the time smearing of the MC simulation<sup>2</sup>. For this purpose the hit time distribution is parametrized by a double gaussian fit:

$$t_{\text{muon}} = \frac{A_1}{A_1 + A_2} * \text{gaus}(\mu_1, \sigma_1) + \frac{A_2}{A_1 + A_2} * \text{gaus}(\mu_2, \sigma_2) \quad (4.6)$$

with the parameters specified in table 4.1. The double gaussian function is selected for parametrization in order to take the empirical larger tails of the distribution into account.

**Table 4.1** – Parameters used as input for the time smearing of the MC simulation with eq. (4.6)

$A_1$	$66.8 \times 10^3$	$\pm 0.3 \times 10^3$
$\mu_1$	$-0.14$ ns	$\pm 0.01$ ns
$\sigma_1$	$3.61$ ns	$\pm 0.02$ ns
$A_2$	$39.8 \times 10^3$	$\pm 0.4 \times 10^3$
$\mu_2$	$0.24$ ns	$\pm 0.01$ ns
$\sigma_2$	$7.39$ ns	$\pm 0.02$ ns

The time resolution is slightly worse compared to what was observed in [50]. This is due to a number of factors. First, the lack of a muon scan over the whole detector is limiting the

<sup>2</sup>Geant4 10.1, Mokka v08-05

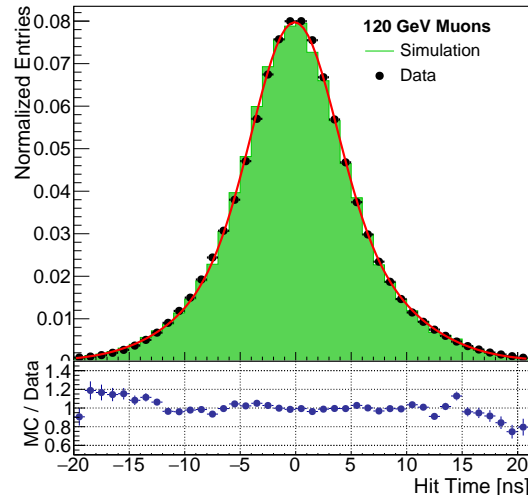


**Figure 4.9** – Muon hit time distribution. Comparison of data (black) and QGSP\_BERT\_HP (green). The shown fit (red) is performed on data using eq. (4.6).

time calibration. Second, in this analysis, a less stringent strategy to remove chips with a bad time resolution has a negative influence on the overall muon time resolution. Furthermore, only two  $T_0$  channels were available in the August test beam campaign, compared to three in the July campaign, as well as the cut on the allowed  $T_0$  time differences was more loose. However, for this analysis, the goal is not an optimization of the muon time resolution. This study rather focusses on the development of a reliable calibration process and the analysis of hadronic showers. For hadronic showers the time resolution is driven by the chip occupancy effect described in chapter 5.

#### 4.4.3 Muon Time Resolution with the Small Steel Stack

In between the partially equipped technological prototype (PTP) and large technological prototype (LTP) a series of test beams was performed with a smaller steel stack hosting 15 active single HBU layers. With the small size the aim of the test beam campaigns is to test new technologies of the AHCAL including powerpulsing, active temperature compensation and the response to electromagnetic showers. Furthermore, the beam interface board (BIF) was introduced, which is a new system for handling trigger input and the reference time. The BIF provides an external time reference with a frequency of 1.28 GHz (bin width of 0.78 ns), which replaces the  $T_0$ -channels used in the PTP. The time jitter of the BIF was estimated to 1.3 ns [115].

The same hit time calibration procedure as described in section 4.2 is applied to the data. The resulting muon time distribution is shown in fig. 4.10. The time resolution is again parameterized as a double gaussian function. Compared to the muon analysis with the PTP, both the narrow and the broader component improve by about 30 % (see table 4.1).

One reason for the better time resolution is the more homogenous detector with fewer broken channels. Additionally, the BIF provides a time reference which is much more stable compared to the  $T_0$ -channels.

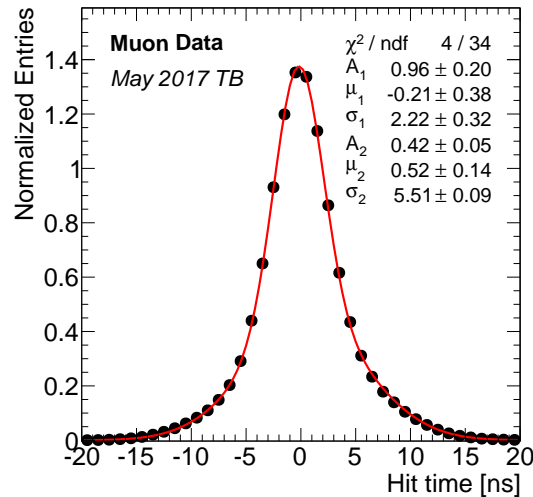


**Figure 4.10** – Muon hit time distribution for data from the May 2017 test beam campaign. A significant improvement in the time resolution is observed compared to the results from the 2015 August test beam campaign.

## 4.5 Conclusions

This chapter presents a time calibration scheme for the AHCAL technological prototype. The main difference to [50] is the calibration of hit times. Instead of determining the pedestal and slope by the edges of the TDC spectrum and determining the offset in a separate step, a linear fit is performed accessing directly the slope and the offset. This method is less prone to uncertainties introduced by features in the TDC spectrum, it simplifies the calibration procedure and fewer muon hits are necessary in order to calibrate the slope of the chips. For the fitting procedure to work, 30 muon hits are required for each memory cell. A toy MC simulation demonstrated that a precision of about 1 ns for the pedestal estimation and about 1 ‰ on the slope parameter are feasible with less than 50 hits for calibration.

During the discussed test beam campaign the detector was not moveable and thus not all cells have enough muon hits for calibration, especially at the outer part of the detector. For those cells, average values of the channel, or the chip are used. A clear decrease in performance of the time resolution between outer and inner chips is visible. For most chips in the inner part of the detector a time resolution of about 6 ns is achieved for muon beam.

## Chapter 5

# Electron Time Analysis

Electromagnetic showers are, as well as muon hits, expected to give instantaneous signals with respect to the achievable time resolution. Thus, they can be used to cross-check the muon time calibration. The hit time distribution for data and simulations of 20 GeV electrons is shown in fig. 5.1 (*left*). It is significantly broadened compared to the MC prediction, which is due to a problem with the readout ASICs that occurs for high channel occupancies in the ASIC. This effect manifests itself in two ways. First, a pedestal shift in the TDC ramp is observed which leads to a time shift (see fig. 5.2, *left*). Second, the hit time distribution is significantly broadened for events with a high ASIC occupancy. The shift can be easily corrected in data using the fit shown in fig. 5.2 (*left*). The broadening of the hit time distribution cannot be corrected but has to be included in the digitization of the MC simulation hits. In order to take this effect into account, the double gaussian fit explained in section 4.4 is convoluted by another gaussian distribution:

$$t_{\text{electron}} = C * \left( \frac{A_1}{A_1 + A_2} * \text{gaus}(\mu_1 + \mu_{\text{conv}}, \sigma_1^2 + \sigma_{\text{conv}}^2) + \frac{A_2}{A_1 + A_2} * \text{gaus}(\mu_2 + \mu_{\text{conv}}, \sigma_2^2 + \sigma_{\text{conv}}^2) \right), \quad (5.1)$$

with  $C$  being a scaling factor and  $\mu_{\text{conv}}$  and  $\sigma_{\text{conv}}$  being the mean and the standard deviation of the convolution function. The width of this additional gaussian depending on the ASIC occupancy is shown in Figure 5.2 (*right*). These values are determined by keeping the other parameters constant and fitting the distributions for different chip occupancies. These values are used as additional parameter for the time smearing of hits in the simulation. For two layers (5 and 6) these effects are so severe that their hit time distributions cannot be recovered at all and thus they are excluded from further analysis. Both effects, the shift and the broadening, are consistent with the observations of data with steel absorber [50, 80]. The electron hit time distribution after applying these corrections is shown in fig. 5.1 (*right*). The time resolution for electrons is 10.2 ns RMS, or 19.1 ns FWHM, with data and simulations being in good agreement. An overview of the full calibration process and the time smearing including the occupancy correction is illustrated in fig. 5.3.

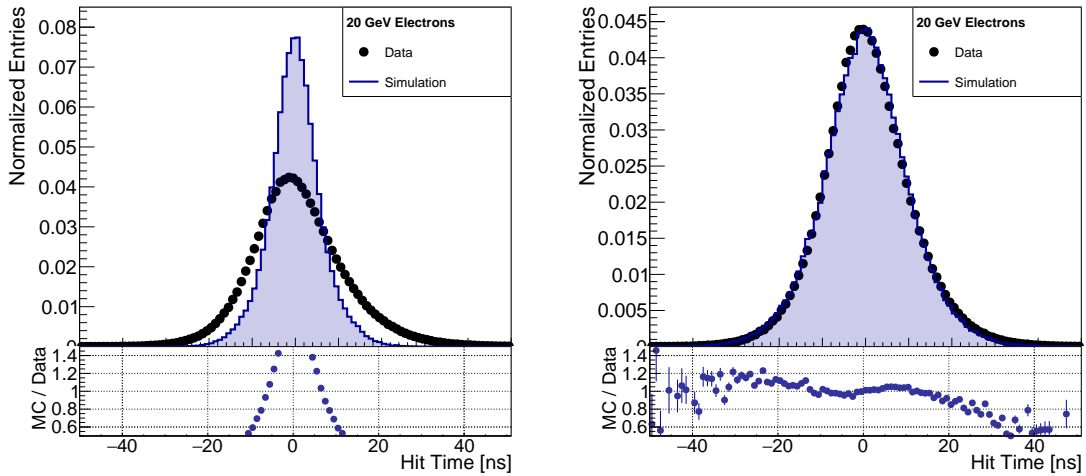


**Figure 5.1** – Distribution of hit times of 20 GeV electrons for data (black) and QGSP\_BERT\_HP simulation (blue) without corrections due to high ASIC occupancies (*left*), and with corrections (*right*).

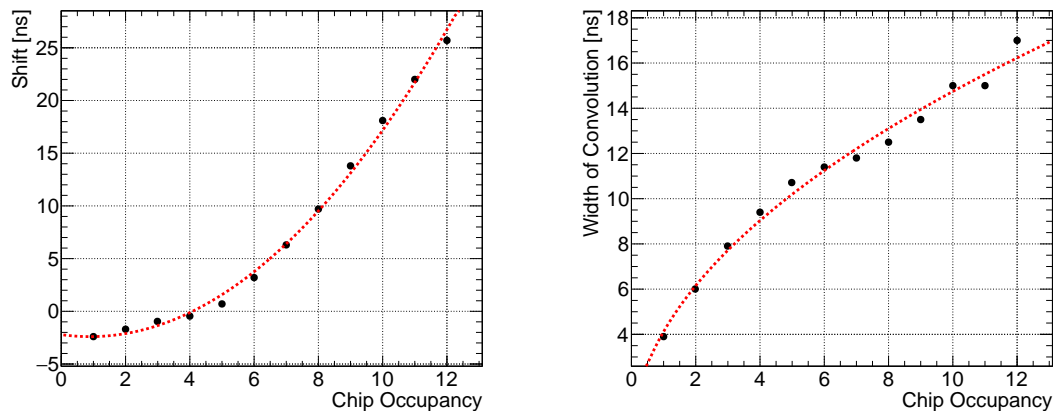


**Figure 5.2** – Correction to the hit time depending on the ASIC occupancy. The observed shift in the hit time distribution (*left*) is corrected for and the broadening of the hit time distribution (*right*) is implemented in the time smearing of the MC hit times. A quadratic and a square root function are fitted respectively.

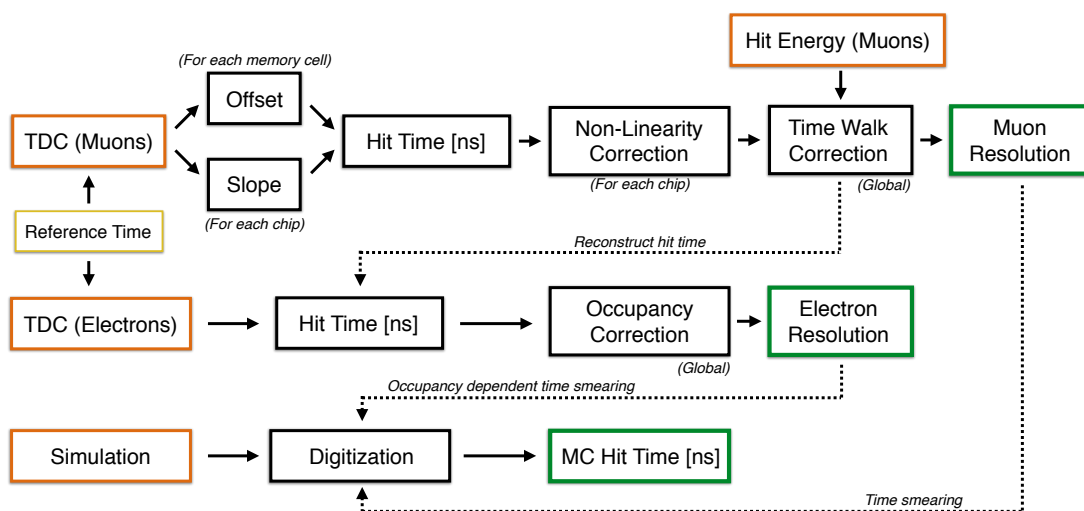


**Figure 5.3** – Overview of the full time calibration chain and the required type of data input (orange). First the hit times are calibrated by extracting the offset and slope parameters of the TDC ramps from muon data. In addition the non-linearity correction and time walk correction are applied. The electron data are reconstructed using these calibration constants. From the electron data the chip occupancy correction is extracted. This is used for the reconstruction of hadron data and used as input for the time smearing of the simulation digitization.

## 5.1 Late Energy Depositions in Electromagnetic Showers

For hadronic showers, late energy depositions are expected due to elastic scattering and neutron capture of slow neutrons. For purely electromagnetic showers no late energy depositions are expected. They may, however, occur in hadronic subshowers due to photonuclear or electronuclear interactions. In high  $Z$  materials, as tungsten, it is expected that mainly neutrons are produced in these interactions.

Figure 5.4 shows the fraction of late hits later than 75 ns for each event. As expected, the vast majority of events have no contribution due to late energy depositions. In the region below 10 % late particles, there are about twice as much events observed as in simulations. This may be due to a non-optimal electron selection with a few primary hadrons still being among the data sample. Above 20 % late particles, there are no events visible in the simulation, but a few in data. These may be double particle events that survive the double particle rejection (see section 6.1). For data there are in total 9.3 % of events in the electron sample with at least one late hit, while for simulated data 4.2 % are observed. In general, however, the shape between the data and simulated distributions are comparable.

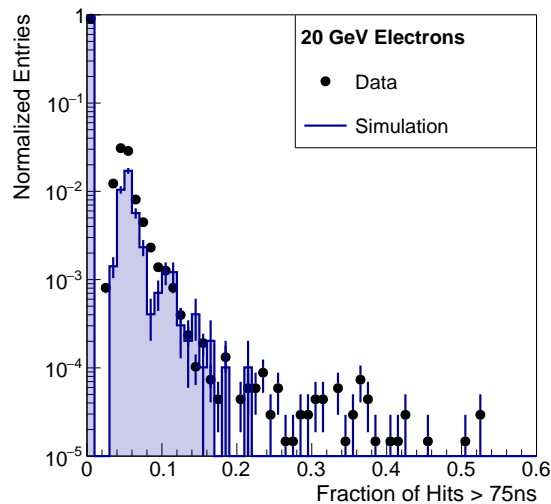


**Figure 5.4** – Fraction of hits later than 75 ns for 20 GeV electron events. Data is compared to MC simulations (QGSP\_BERT\_HP).

## Chapter 6

# Hadron Time Analysis

This section discusses the hit time distribution for pion data and compares it to MC simulation. A special focus is set on the distribution of late energy distributions. At the beginning of this section a new technique will be presented to identify events where two beam particles are measured by the detector shortly after each other, but merged into one event.

### 6.1 Using Time Information to Remove Double Particle Events

In the event building step, it is assumed that only one beam particle reaches the detector within one bunch crossing. However, at a test beam campaign it may happen that two particles arrive at the detector within the same bunch crossing. In a fully equipped prototype these events can be easily detected, because they are expected to have about twice the number of hits and deposited energy. With this particular prototype this method does not clearly separate double particle from single particle events, as there are many empty layers and dead channels and thus the event to event fluctuations in the number of hits and the measured energy sum are very large. Figure 6.1a shows for each hit time in layer 14 the closest hit in time in layer 15 for a 70 GeV pion beam. Because of the ten empty layers between layer 14 and 15 no correlation in the hit times is expected from physics processes for late hit times. The peak around (0,0) is created by the instantaneous part of the shower. The bands near the  $x$ - and the  $y$ -axis are part of the late component of the hadronic showers, where one of the two hits is instantaneous. The uncorrelated hits in between are again part of the late component, where both hits are induced by uncorrelated late energy depositions. Additionally, a correlated part along the diagonal is visible, which is not observed in simulations (fig. 6.1b). These correlated hits originate from double particle events, where a second particle in the same bunch crossing reaches the detector at a later time.

Two particles that arrive in the same bunch crossing but not at the exact same time can be distinguished by the time information. It is looked for clusters in the time dimension. With a sliding window technique a late cluster is defined as soon as there are more than

10 hits within 30 ns, starting from 100 ns after the reference time. Additionally, groups of hits with five to ten hits in such a time window are called a *late cluster* when their mean hit position in  $x$ - and  $y$ -direction between layers is close enough. The second selection criterion is intended to select muons and punch through pions. In total 1771 events are identified for the 70 GeV pion data sample in such a way. Figure 6.1d shows the size of the detected clusters. For simulations no event passes the selection. As can be seen in fig. 6.1c, after the rejection of events that contain a late cluster the correlation of late hits between layers 14 and 15 is removed below the background of the uncorrelated late energy depositions.

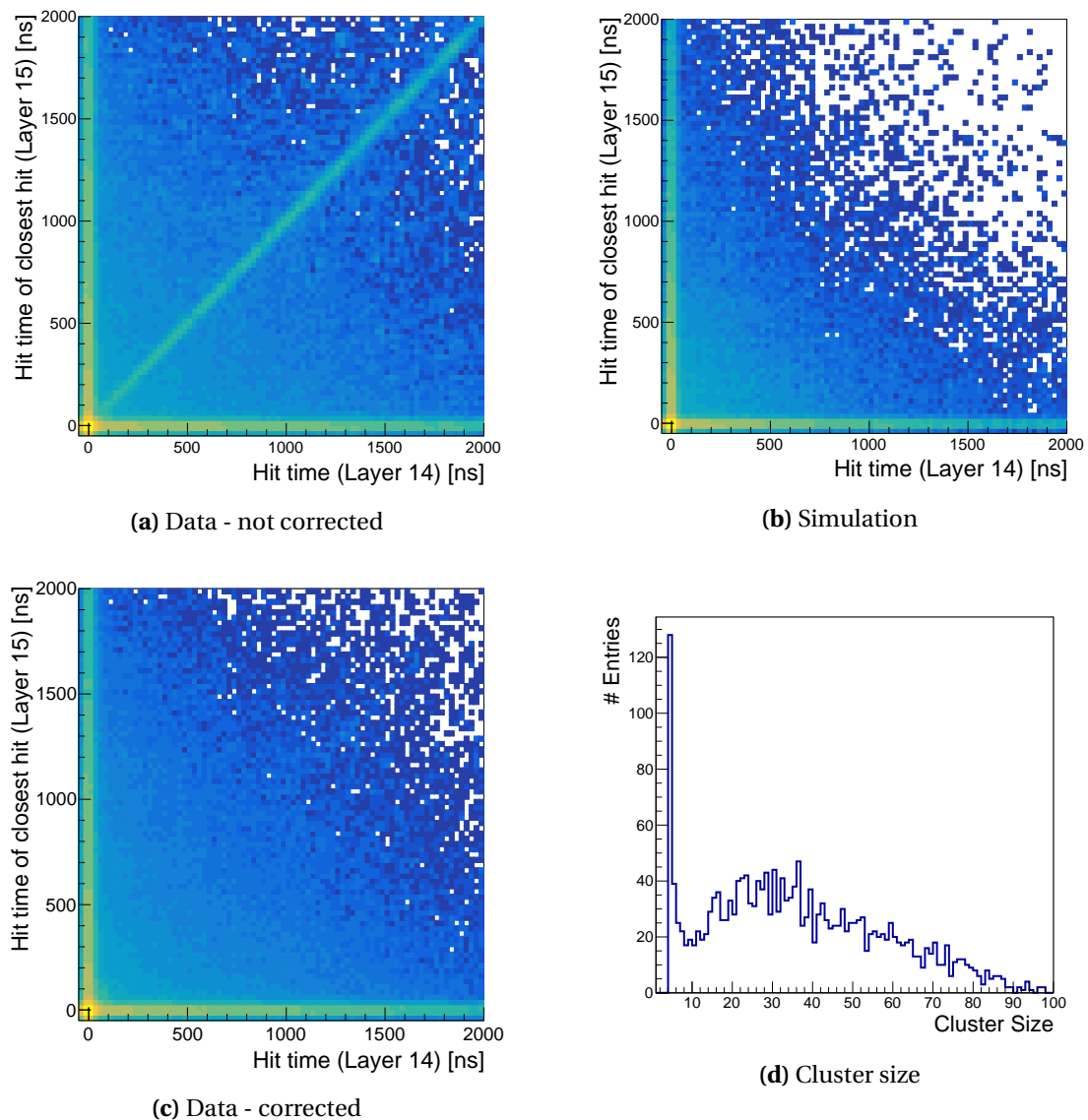


**Figure 6.1** – Hit time correlations of hits in layer 14 with the closest hit in time of layer 15 for 70 GeV pion samples (a) data and simulation (b) (c) correlations after the removal of the double particle events for data. (d) The size of the detected late clusters.

## 6.2 Pion Time Structure

The time distribution of hadronic showers is shown in fig. 6.2 (*left*). Compared to electromagnetic showers discussed in the previous section, a late tail in the distribution is visible. The production of slow neutrons in the hadronic part of the shower leads to two processes that produce delayed hits. On timescales of the order of a few ns, neutron-proton elastic scattering is the dominant process, while energy depositions due to neutron capture can extend to several  $\mu\text{s}$  after the primary particle hits the calorimeter. In general, an energy dependence of the electromagnetic fraction of an event is expected, leading to a higher electromagnetic fraction and thus a lower fraction of late energy depositions at higher energies. In fig. 6.2 (*left*) the relative amount of the number of late hits is constant across the whole energy range from 10 to 90 GeV. This is because for higher electromagnetic fractions, mainly the energy density increases leading to higher energy hits, while the number of hits in the core of the shower is expected to increase much less. The slight broadening of the distribution between 50 ns and 120 ns is due to the occupancy-dependent effects described in chapter 5. As higher energetic particles produce more hits, the average occupancy of the ASICs is higher in this case resulting in larger tails of the distribution.

A comparison of data with MC simulations is exemplified by 70 GeV pions for different physics lists in fig. 6.2 (*right*). It shows a sorting of the physics lists into two categories depending on the model that is used for low energetic particles. Physics lists as QGSP\_BERT\_HP that rely on the Bertini model [116] show significantly more hits with hit times  $> 100\text{ ns}$ . QBBC and QGSP\_BIC use a binary cascade model for the propagation of low energetic particles. For them, less of these late hits are observed compared to data. QGSP\_BIC\_HP that uses the high precision neutron model, shows a similar behavior as the QGSP\_BERT-like models.

The distribution of the fraction of hits in an event that are later than 75 ns is shown in fig. 6.3a. Data is compared to three physics lists: QGSP\_BERT as a representative using the Bertini model, QGSP\_BERT\_HP using the HP package for low energetic neutrons and QBBC relying on the binary-cascade model. In data the most probable value is 5% hits later than 75 ns. For QBBC the distribution is slightly shifted to lower values with significantly more events that do not have a late hit at all, while the distribution for QGSP\_BERT(\_HP) is shifted to higher values with the most probable value being around 13% (15%).

Figures 6.3b, 6.3c and 6.3d show the distribution of the average fraction of late hits over the position in  $z$ -direction, the hit radius (radial distance to center of gravity of the event) and the hit energy. It can be seen that the late hits are consistently distributed over all layers. The QBBC physics list is missing some of the late hits especially in the last layer. Low energetic energy depositions have a large fraction of late hits (up to 8% for hit energies between 0.5 MIP and 1.0 MIP). Large energy depositions above 5 MIP are again dominated by the electromagnetic part of the shower and thus show nearly no content of late energy depositions. While the center of the shower is dominated by the quasi-instantaneous electromagnetic shower, the

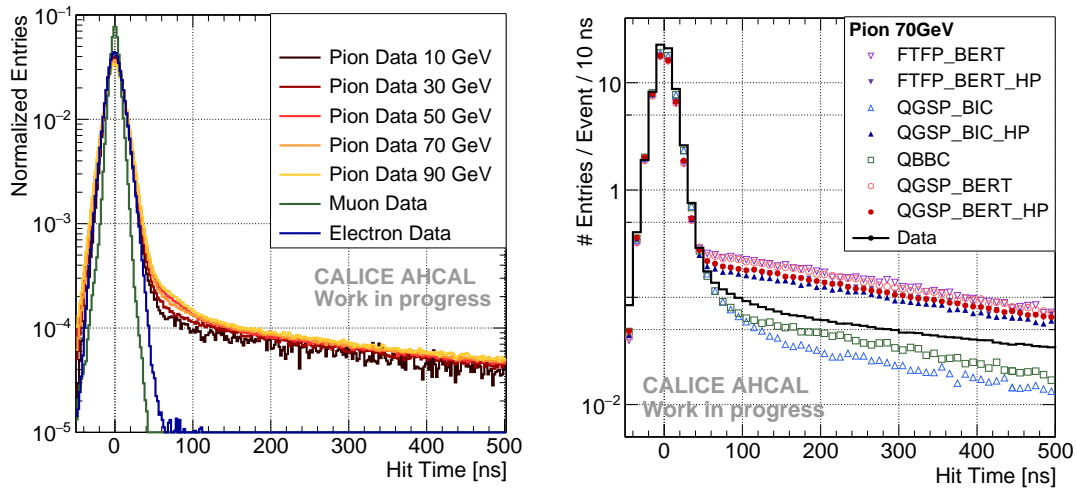


**Figure 6.2** – *Left*: Distribution of hit times for 10 to 90 GeV pions, 120 GeV muons and 20 GeV electrons. Distributions are normalized to 1. *Right*: Distribution of hit times of 70 GeV pions for data (black) compared to several Geant4 physics lists and normalized to the number of hits per 10 ns per event.

outer part of the shower consists to a large extent of late energy depositions (up to 25 % for data at hit radii close to 300 mm). The QGSP\_BERT(\_HP) physics lists have consistently more late hits distributed over all hit radii and hit energies compared to data, while QBBC is missing late hits mostly for low energy depositions ( $< 3$  MIP) at large hit radii ( $> 120$  mm).

Figure A.1 in the appendix shows the lateral shower shape as well as the hit radius distributions for early and late hits. It can be seen that the instantaneous part is well described by all physics lists. Also the shape of the hit radius distribution for late hits agrees between data and the QGSP\_BERT(\_HP) physics lists. This shows that it is not the transversal distribution of late energy depositions that is inconsistent between data and simulations, but the number of such occurrences.

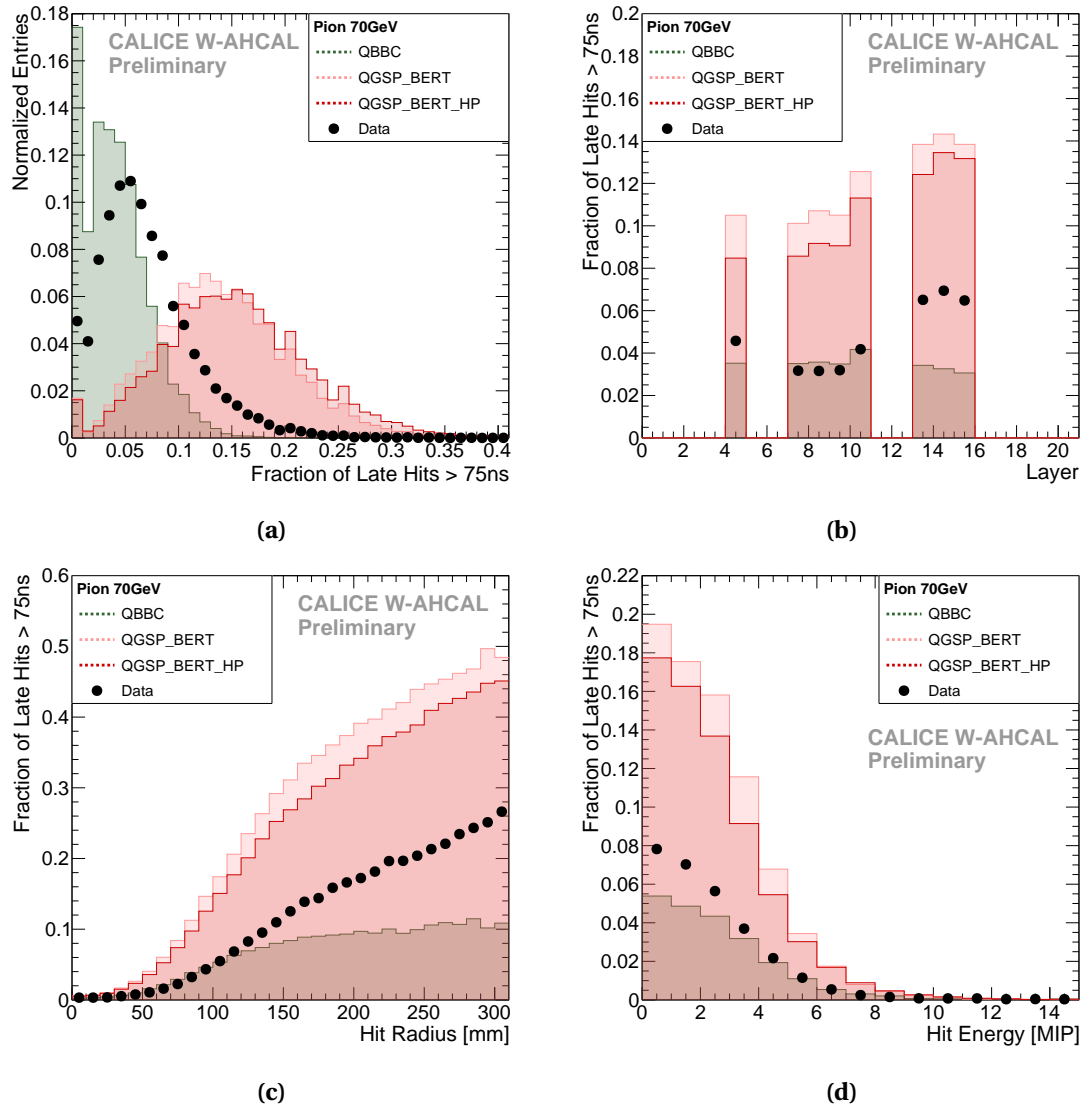


**Figure 6.3** – (a) Distribution of the fraction of hits in each event that are later than 50 ns, the fraction of late hits distributed over layers (b), hit radii (c) and hit energies (d). Comparison of data (black) with QGSP\_BERT (light red), QGSP\_BERT\_HP (dark red) and QBBC physics list (green).

### 6.2.1 Discussion of Uncertainties

Statistical errors are in general low for the distributions shown in this section and are not drawn in order to maintain readability of the plots. For systematic errors, various effects have to be discussed:

- **Calibration:** For the calibration a high precision is observed. Uncertainties in the calibration and time walk corrections are expected to be much smaller than 1 ns on average. However, especially at the outer part of the detector, not all channels can be calibrated properly, which may lead to uncertainties of a few nanoseconds for those channels.
- **Occupancy correction:** The occupancy correction may lead to uncertainties of a few nanoseconds, especially for high chip occupancies where less data is available to estimate the correction parameters.
- **Multi-particle events:** Most multi-particle events are rejected in the event selection. A few may survive the selection but are not expected to have a significant influence on the results.
- **Noise:** The noise hit rates are estimated from muon and electron runs to be about  $2 \times 10^{-5}$  to  $5 \times 10^{-5}$  hits/ns/event. Compared to the rate of the late component for hadrons (about  $3 \times 10^{-3}$  hits/ns/event) this is on the percent level. A noise hit is expected in only every tenth event.
- **Prior neutron activity:** The late neutron component of hadronic showers may extend up to hundreds of  $\mu$ s. However, the exact behavior seconds. For most particle energies about 40000 events are observed per spill. This translates to a rate of 4 kHz, with on average 250  $\mu$ s in between events assuming no substructure in the spills. Hence, it is possible that neutron activity from prior events still influences the next one. On average at 500 ns before the  $T_0$  signal about  $2 \times 10^{-4}$  hits/ns/event are observed, about 15 times less compared to 500 ns after the  $T_0$  signal. Therefore, the late component for the data might be overestimated by a few percent at 500 ns due to slow neutrons originating from prior hadron events.
- **Birk's law:** The effect of scintillator saturation is only understood empirically and differences in the size of Birk's constant may lead to uncertainties in the simulation. This is discussed in detail in the next section (section 6.3).

The total systematic uncertainties on the hit time measurements are of the order of a few nanoseconds, dominated by the chip occupancy correction and uncalibrated cells. For fig. 6.3, the fraction of hits later than a fixed threshold is used as a metric to compare data and simulations. The threshold of 75 ns is chosen in such a way that systematic uncertainties

have a minimal impact on the results. In order to check the robustness of this measure, the mean number of late hits is compared for thresholds of 70 ns, 75 ns and 80 ns. The mean fraction of late hits varies relatively by less than 1 % for these values.

### 6.3 The Influence of Scintillator Saturation

The default parameter for Birks' law (see section 1.4.1) implemented in Geant4 for a polystyrene scintillator is  $kB = (0.0794 \pm 0.0014)$  mm/MeV taken from [98]. The measurement was obtained from a SCSN-38 scintillator which is polystyrene based with a doping of 1 % buthyl-PBD and 0.02 % BDB [117]. The AHCAL tile is also polystyrene based with a doping of 1.75 % PTP and 0.01 % POPOP [118]. In [118], a study of Birks' constant for an AHCAL tile was performed and a significant deviation from the Geant4 default parameter was ( $kB = (0.151 \pm 0.007)$  mm/MeV).

In order to evaluate the uncertainties that may arise due to these differences, the simulation of 70 GeV pions were redone with the QGSP\_BERT\_HP physics list without taking Birks' law into account and with a twice as high value for Birks' constant  $kB$ . The results are shown in fig. 6.4. A significant influence of the scintillator saturation effect can clearly be seen. Without taking Birks' law into account much more hits are visible in the instantaneous part of the shower and in the intermediate part. This is expected, as highly ionizing particles are mostly recoil protons and small nuclei fragments originating from neutron elastic scattering [34], as well as low energetic electrons. The late part, later than 100 ns, is stable under these effects, as it mostly is due to photons originating from neutron capture. An increase of Birks' constant close to the region observed in the study mentioned above, however, has only a minor influence on the instantaneous and intermediate region. Up to 50 ns, doubling Birks' constant leads to 5 to 20 % decrease in the number of hits. The relative decrease is larger for the intermediate part between 20 to 50 ns. For hits later than 50 ns, no significant difference is visible.

From this study an additional uncertainty of 20 % is extracted for the amount of hits earlier than 50 ns. This result also has an influence on the fraction of late hits later than 75 ns shown in fig. 6.3. The mean of this fraction decreases relatively by about 6 % for the increased Birks' constant - moving the simulated results even further from the data observation.

The visible energy sum is enhanced by about 40 % if Birks' law is switched off and reduced by about 7 % for  $kB = 0.151$  mm/MeV compared to the standard case. In [118] only 20 % enhancement was observed without Birks' law for MC simulations with a physics prototype geometry using steel absorber. The reduction for the larger Birks' constant is comparable. As the geometry and the absorber material is very different between both studies, and because of the non-optimized energy calibration for this study, these numbers are only a qualitative cross-check.

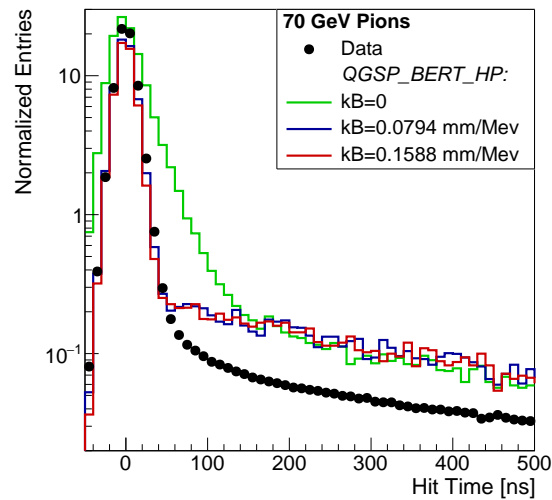


**Figure 6.4** – 70 GeV pion simulation using the QGSP\_BERT\_HP physics list. Comparing the standard birk's factor (blue) with twice the value (red) and no saturation (green) applied.

## 6.4 Pion-Proton Comparison

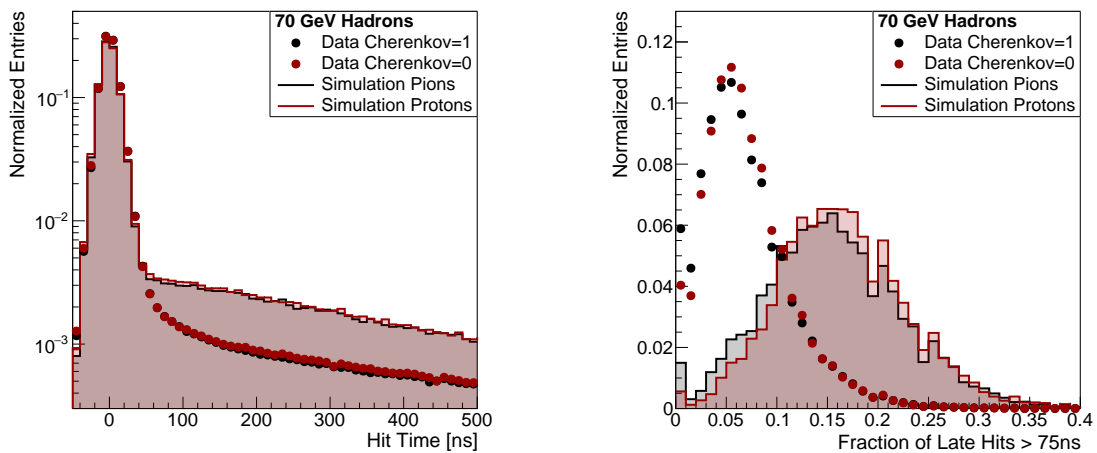


**Figure 6.5** – *Left*: Hit time distribution for data sample with and without a Cherenkov signal tag compared to pion and proton MC simulation using the QGSP\_BERT\_HP physics list. *Right*: Fraction of hits that are later than 75 ns after the reference time for the same data sets.

As mentioned already in section 3.4.4, the most striking difference between a proton and a pion beam is the expected higher electromagnetic content of pion showers. This is due to the enhanced probability for the production of baryons in the early stages of the proton shower because of baryon number conservation. In addition to the shower variables studied above, this effect can also be seen in the time distributions. Figure 6.5 shows the hit time distribution and the fraction of hits for each event that are later than 75 ns after the reference time for data samples with and without a Cherenkov tag. The Cherenkov detector was present in the

beam line and operated in such a way that a pion should give a signal, while a proton should not (see section 3.3). The distributions of the data sample with and without a Cherenkov signal are compared to simulations using the QGSP\_BERT\_HP physics list. A higher fraction of late hits can be observed in the data sample without the Cherenkov hit compared to the data with a Cherenkov hit. This behavior is compatible with the interpretation of a proton sample with a higher hadronic content than the pion sample. The same observation can be done for the MC samples. For the proton sample especially the number of events with very few late hits (first bin) is greatly reduced. On average the events in the proton sample show 3.5 % more late hits than the pion sample (5.8 % for simulations). Again, it should be noted here that the efficiency of the Cherenkov detector is estimated to be about 70 %, meaning that the proton data sample is expected to contain a significant amount of pion events. The results achieved in the pion-proton comparison show already the correlation of the electromagnetic fraction with the time structure of hadronic showers and the possibility to measure them even in a partially equipped prototype.

## 6.5 Comparison to the T3B Experiment

In T3B, good agreement is observed for QBBC and QGSP\_BERT\_HP with a tungsten absorber, while a large discrepancy for late hits is seen for QGSP\_BERT, based on simulations with Geant4 v9.4 [119]. In the presently used Geant4 v10.1 substantial changes have been implemented in nearly all physics lists. The neutron capture cross-sections and the neutron final state model of QBBC have been adopted by QGSP\_BIC, QGSP\_BERT and FTFP\_BERT. Also QBBC itself underwent changes especially in the low and medium energy regions ( $< 12$  GeV) for hadronic interactions [120].

In addition, the T3B experiment had a special geometry. It was located at the very end of the physics prototype probing on average a different depth of the shower, as well as giving more weight to hits near the center of the shower, due to the strip geometry of the experiment. Also the larger scintillator content in the physics prototype (5mm thickness and more layers equipped) leads to a larger thermalization of the neutrons.

As a cross-check, a toy Monte Carlo experiment was set up to check the influence of the different Geant4 versions as well as geometric effects. Even though it is difficult to directly compare the two experiments due to many systematic differences, the observed results of the toy MC simulation are consistent with the differences between the T3B results and the analysis presented in this thesis.

## 6.6 Comparison to Steel Absorber

As tungsten has a higher atomic number than steel, more hadronic interactions are expected with a tungsten absorber compared to a steel absorber leading to a larger number of produced

low energetic neutrons and thus to more late hits. The time analysis of the engineering prototype with a steel absorber is described in [50]. Figure 6.6 shows the time distribution of 50 GeV pions with a tungsten and steel absorber. In tungsten the late tail of the distribution is enhanced by about a factor eight.

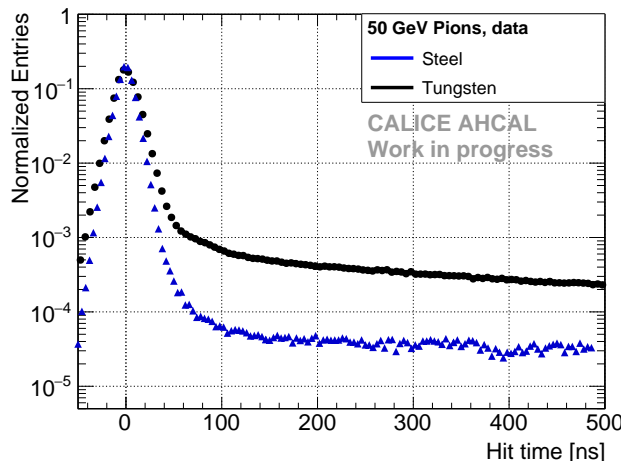


**Figure 6.6** – Comparison of the time distribution of 50 GeV pions between data with a steel absorber (blue) and a tungsten absorber (black).

## 6.7 Conclusions

In this chapter, the time structure of hadronic showers was studied with the PTP in a tungsten absorber stack and compared to simulations. The time information showed to be a valuable observable for the rejection of double particle events. For hadronic showers a significant contribution of late energy depositions to the calorimeter signal was observed. The fraction of late hits was found to be constant for the entire energy range from 10 to 90 GeV. Compared to simulations using Geant4 v10.1 it was observed that different physics lists show a very different behavior. Physics lists employing the bertini cascade or the neutron high precision package (`_HP`) are overestimating the late energy contributions by about a factor two. Physics list using the binary cascade model are underestimating the late contributions by about the same factor. On average about 5% of the hits in the calorimeter were observed later than 75 ns. The late hits predominantly have low energy depositions and are located most probably at the outer part of the shower. This is in line with the interpretation of energy depositions due to slow neutrons.

Differences in the time distribution between the proton and pion sample were observed. The pion sample shows significantly more events without any late hits compared to the proton sample. This is expected because of the reduced probability of protons to generate  $\pi^0$  particles in the very first step of the interactions, due to baryon number conservation. In

general, slightly less late energy depositions are observed for the pion samples compared to the proton samples. These results show the strong correlations between the time measurements and physics processes in the shower. It is encouraging that those effects can be observed already with the PTP regardless of the inhomogeneous distribution of active layers and the limited time resolution. In a full calorimeter with an improved time resolution these differences in the time structure could be used as a feature in a multivariate method to improve the particle identification between baryons and mesons.

Compared to the time analysis with the steel absorber, about eight times more late hits are observed with the tungsten absorber, which is expected because of the higher  $Z$  nuclei in tungsten. For the T3B experiment an enhancement of the late energy depositions in a tungsten absorber compared to a steel absorber was about a factor six. The differences may arise partly because of slightly different selection strategies and changed conditions between the PTP tungsten and steel analysis, but most likely also due to the different geometries of the T3B experiment compared to the LTP leading to a different sampling of the hadronic showers.

Despite the difficulties faced in this analysis of test beam data taken with the PTP in a tungsten absorber stack in August 2015, it could be shown that the presented time calibration allows for a complex analysis of the time structure of hadronic showers.



## **Part III**

# **Energy Reconstruction**



## Introduction and Overview

The third part of this thesis is devoted to the energy reconstruction of the AHCAL. The important role of spallation neutrons for the calorimeter response was highlighted in section 1.4.5. In [45] it is shown that measuring the neutron content of hadronic showers via their time development can be used to improve the performance of a dual readout calorimeter. Correlations between the energy sum of a calorimeter and the time structure of hadronic showers are also reported in a simulation study [121].

In this part, correlations of the hit time measurements with the reconstructed shower energy are explored in simulated data of a realistic, fully equipped AHCAL large technological prototype (LTP). After a presentation of the experimental setup and the data preparation steps in chapter 7, correlations between hit time observables, hit energy observables and global shower observables with the reconstructed energy are analyzed in chapter 8. Further, the influence of a limited integration time on the detector performance is studied. In chapter 9 it is investigated to what extent the hit time measurements can be used to improve the energy resolution. For this, a simplified and robust version of the global software compensation (SC) approach is implemented. The results are compared to the traditional global SC method which is relying on hit energy observables.

In chapter 10, an artificial neural network model is developed for energy reconstruction in the AHCAL. The neural network can be used with a large number of input features. It is studied whether hit time information together with other global shower observables are improving the energy resolution. This concept is extended to include the longitudinal shower profiles as input for the neural network. These methods are first developed on simulated data of the LTP and later verified on test beam data.



## Chapter 7

# Data Preparation

A careful data preparation is crucial for this study, especially for the use of machine learning techniques. The risk to *leak* true data into the training process is very high and subtle effects can easily lead to an exaggerated interpretation of an algorithms' performance.

Of the highest importance is the strict separation of training and testing data. The training data includes the true values of the target variable, which is unknown in the test set. This also has an effect on the data preparation processes. The event selection may not depend on the true beam energy, because the selection is also used for the test set and algorithms with many parameters could infer the true beam energy from this event selection process. Additionally, the beam energies used for training should be as uniformly distributed as possible in order to avoid binning effects in the true beam energies in the training process.

For the energy reconstruction studies, MC simulations based on the geometry of the CALICE AHCAL large technological prototype (LTP) with steel absorber are used. For validation with test beam data, data from the AHCAL test beam campaign in June 2018 are used. This chapter presents the experimental setup as well as the event selection.

### 7.1 Experimental Setup

The concept of the LTP is described in section 2.3.6. The setup consists of a steel absorber stack with 44 layers of 17 mm steel [122]. There are 38 active layers starting after the first absorber plate, each equipped with a full module of four HBUs. The 576 channels for each layer add up to 21888 total channels. In the beam line, two wire chambers, three trigger scintillators and a Cherenkov detector were present.

### 7.2 Test Beam Campaign May/June 2018

Data with the LTP was taken in two two-week test beam campaigns in May and June 2018 at the H2 beam line at the SPS (CERN). The two campaigns had slightly different setups. While

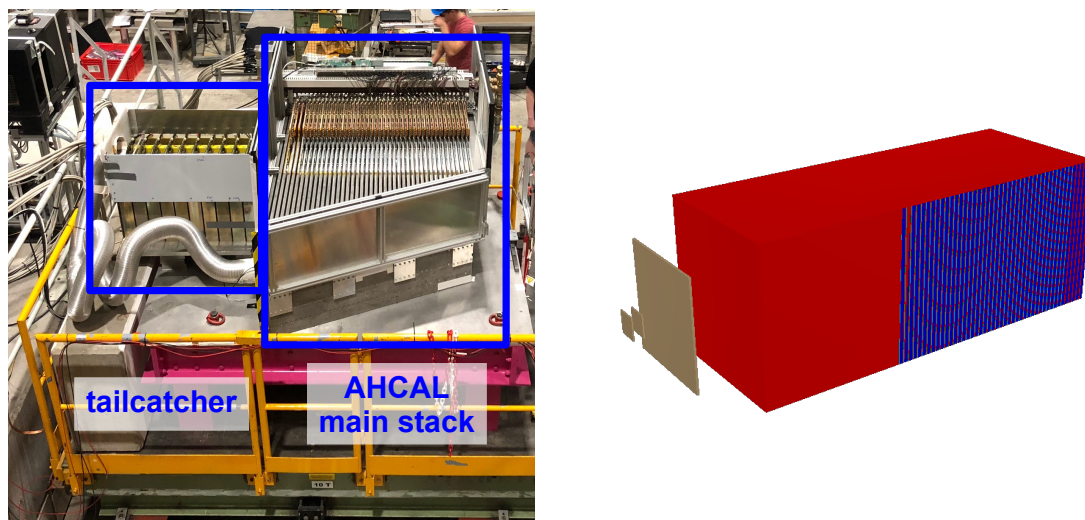


**Figure 7.1** – *Left*: Setup of the June 2018 test beam campaign at the SPS (CERN). The AHCAL main stack is placed in front of the tailcatcher. *Right*: Extended simulation model of the AHCAL with 65 absorber layers and 60 active layers. The separate layers are only partly visible. The three trigger scintillators in front of the AHCAL are displayed in brown color.

the core detector was the same, for the June test beam campaign an additional tail catcher was present behind the AHCAL. In addition, a special layer for testing a larger scintillator size, as well as a single HBU located in front of the AHCAL and used as a pre-shower detector, were added to the setup (see fig. 7.1, *left*). For simplicity, these additional detector parts of the June setup are not considered in this analysis. For calibration purposes, 40 and 120 GeV muons were taken, as well as hadrons in the range from 10 to 160 GeV. Additionally, electron data was recorded in the range from 10 to 100 GeV. Details can be found in [123].

### 7.3 Monte Carlo Simulation

The Monte Carlo simulations are done using the geometry of the May test beam campaign described above using the DD4HEP framework<sup>1</sup> [97]. The pre-shower layer, the additional layer with larger tile sizes and the tail catcher from the July geometry are not implemented. The digitization follows the standard procedure described in section 2.5.2.

With a depth of 38 layers (about  $4\lambda$ ) many high energetic hadrons deposit a significant amount of their energy after the last active layer (leakage). This problem can be mitigated in various ways. A tight cut on the shower start in the very first layers can be imposed in order to select only events that use as much of the active material as possible. This, however, is very inefficient, as only a small subset of the initially generated events can be used. For the highest energies, it is also possible that showers starting in the first layer may exceed the last active layer. A second possibility to reduce the effect of leakage is to select only

<sup>1</sup>ILCSOft v02-00-01, GEANT4 v10.03

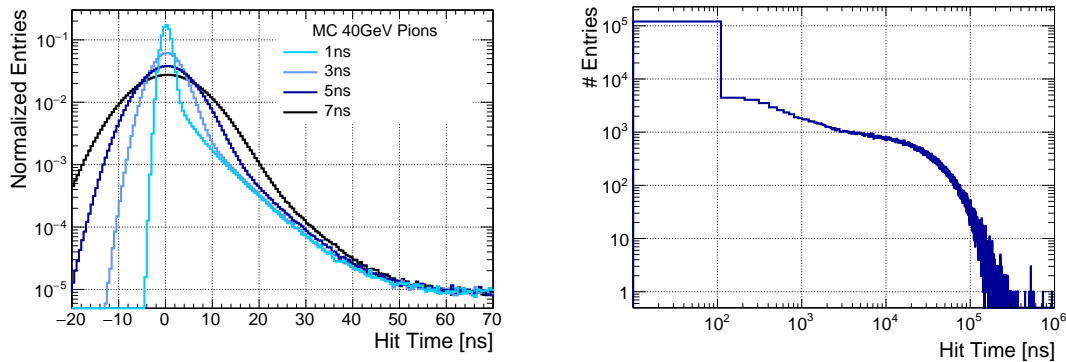


**Figure 7.2** – Time distribution of 40 GeV pions of simulated data with different time smearings (*left*) and an extended x-Axis (*right*).

events that have no energy deposition in the last layers and thus have a low probability of producing leakage. The downside of this selection procedure is a bias of the event sample, along with a significant reduction of usable data. It favors shorter showers and the sample is not representative for the broad range of showers expected in a future collider experiment. Because these side effects of the described selection procedures cannot be tolerated for the present study, the detector geometry is extended to 60 active layers in simulation. Material behind the last active layer may have an impact on the last layers for hadronic showers due to the possibility of backscattering of the particles. To account for this, five non-instrumented absorber layers are added behind the last active one, resulting in 65 absorber layers in total (see fig. 7.1, *right*). This extended geometry with 60 active layers allows to study correlations and energy reconstruction methods without the resolution being dominated by leakage. The effect of a reduction in the number of active layers is investigated in section 10.4.

For hit time measurements a gaussian time smearing of 1 ns is applied, unless stated otherwise. Despite being not yet reached in test beam measurements, a time resolution of 1 ns is the targeted time resolution of the AHCAL. The T3B experiment already showed that this can be achieved with scintillating tiles, SiPMs and typical hit amplitudes similar to the ones used in the CALICE prototype [124]. Figure 7.2 (*left*) shows the time distribution of 40 GeV pions after digitization with different time resolutions applied. The tail for hit times later than 50 ns is not influenced by a time resolution of up to 7 ns. The possibility to distinguish the intermediate part from the instantaneous one is largely influenced by the time resolution. A time resolution of at least 3 ns would be needed for a clear separation of parts of the intermediate time regime.

The time distribution of 40 GeV pions for a time resolution of 1 ns is presented on a large scale in fig. 7.2 (*right*). It can be seen that in simulation the hit times extend up to several tens of  $\mu\text{s}$  with only a slow decrease after 100 ns. However, in an optimal case, the current test beam setup can only record hits up to about 4  $\mu\text{s}$ . In a first step, the very late hits will be included in the simulation study and the effect of a limited integration time will be discussed

separately.

Especially for the training of machine learning techniques, a fine spacing between beam energies is important in order to avoid effects that exploit the binning of the beam energies. For this study, negative pions in the range from 10 GeV to 85 GeV are simulated in 1 GeV steps with 10000 events for each energy, resulting in 750000 simulated events. The stepping of 1 GeV is expected to be fine enough. With an estimated energy resolution of about  $50\%/\sqrt{E}$ , the standard deviation (assuming a gaussian energy distribution) of 10 GeV pions is expected to be about 16% (1.6 GeV). This allows for a significant overlap of the distributions of reconstructed energy of even the lowest energy pions.

Figure 7.3 shows event displays of two different simulated 60 GeV pion showers in the LTP. The color scheme represents the hit energy (*left*) or the hit time (*right*). The large variety of hadronic showers gets immediately apparent, as well as the possibility of the LTP to observe details of the shower. The high energetic, electromagnetic core of the showers is clearly visible (*left*) as well as late energy distributions located at the outer part of the shower (*right*). The second shower (*bottom*) has most likely more electromagnetic contributions due to its smaller size, a larger, high energetic core, and less late energy depositions.

## 7.4 Shower Start Finder

A special difficulty of the shower start finding algorithm is that it should not depend on the true beam energy, as most standard implementations within the CALICE reconstruction software framework do. In order to overcome this, a simple and robust shower start finder is developed. The shower start is defined as the first layer that fulfills one of the following two conditions:

1. At least 3 MIP energy deposition in the current layer, 5 MIP in the consecutive layer and 8 MIP in the next to next layer.
2. At least 2 hits in the current layer, 3 hits in the consecutive layer and 4 hits in the next to next layer.

## 7.5 Event Selection

The aim of the event selection is to clean the data sample from events that distort the reconstruction process. For the present study we want to remove events that have an atypical energy deposition in the calorimeter, caused mainly by leakage. On the other hand, the event selection should not depend on the true beam energy and should not bias the data sample. For this reason the event selection is kept as minimal as possible.

For simulated data, events are selected which have their shower start in the first ten layers. This cut reduces the data sample by about a factor of two. Additionally, the far tails

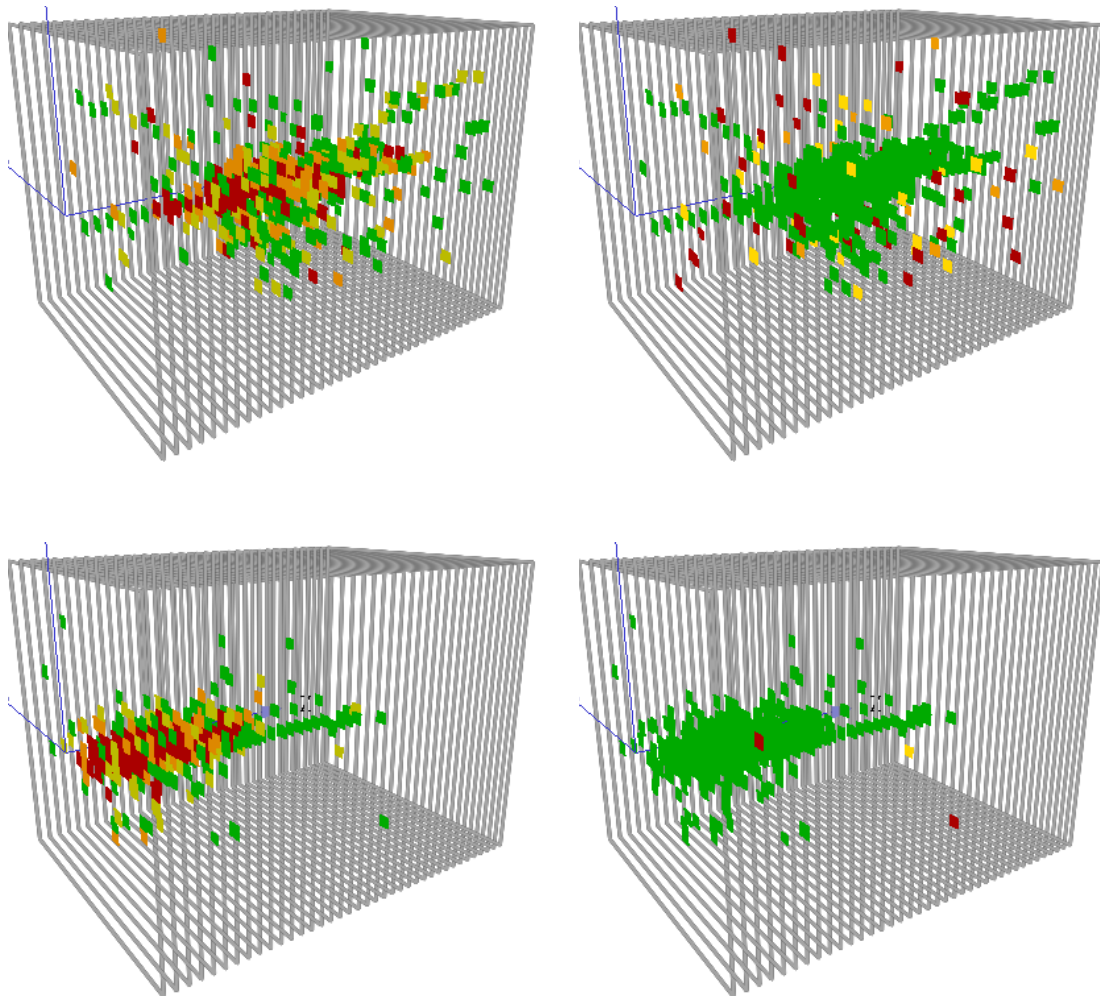


**Figure 7.3** – Event displays of two different simulated 60 GeV pions in the LTP (*top / bottom*). The color scale shows the hit energy (*left*) (green [0.5, 1.65), yellow [1.65, 2.9), orange [2.9,5.4), red  $\geq 5.4$  MIP) and the hit time (*right*) (green  $< 5$ , yellow [5, 15), orange [15,50), red  $\geq 50$  ns).

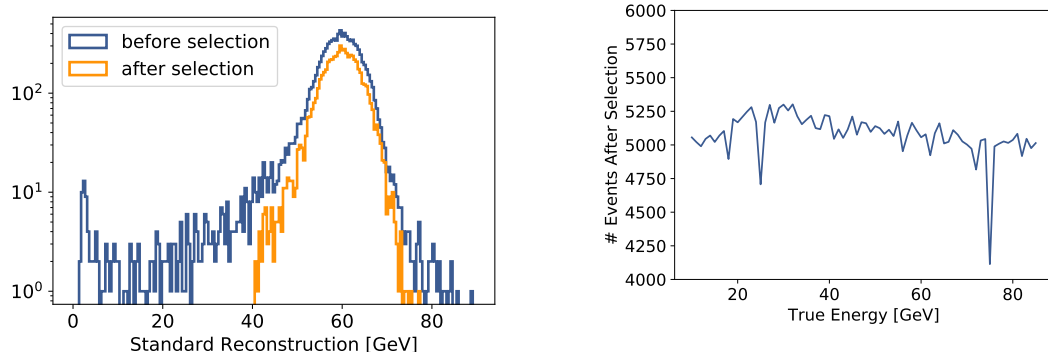


**Figure 7.4** – *Left*: Energy distribution of standard reconstruction for 60 GeV simulated pions before and after event selection. *Right*: Number of events in the data set for each energy after event selection. The few dips in the distribution are due to unfinished jobs of the simulation.

of the energy distribution are cut away by a cut on the energy sum of  $\pm 2.5 \sqrt{E_{\text{beam}}}$  for each beam energy. There are only few events that are effected by this cut ( $\ll 1\%$ ), mainly due to particles showering very late with large amounts of leakage. This cut helps greatly in reducing outliers in the distributions. Figure 7.4 (*left*) for example, shows the reconstructed energy distribution for 60 GeV pions before and after the event selection. On average slightly more than 50 % of the events are passing the selection. The number of selected events per energy is presented in fig. 7.4 (*right*). Few energies show slightly less events after the selection process. This is because of unfinished jobs in the MC generation procedure. In general the number of selected events decreases with energy, caused by the higher probability of leakage for higher energies. Overall, the data sample is sufficiently balanced between the different beam energies.

## Chapter 8

# Energy and Time Correlation Studies

The well established concept of software compensation (SC) (see section 2.4.3) has already been studied in great detail within the CALICE collaboration. It exploits the fact that the electromagnetic part of a hadronic shower has a higher energy density than the hadronic part. By assigning lower weights to regions of higher energy density, it is possible to correct the reconstructed energy for effects occurring because of the non-compensating nature of the prototype and thus improve the energy reconstruction for hadronic showers.

In this chapter, the correlation between energy and time dependent observables with the reconstructed energy will be studied. The strategy is to quantify correlations of hit energy dependent observables on simulated data with an idealistic geometry of the LTP. These results are compared with correlations found in hit time dependent observables. Furthermore, global shower observables such as the shower radius are considered. The effect of reducing the integration time of energy depositions and the number of active layers are investigated in order to steer the simulation more towards a realistic setup. Finally, the simulation results are compared to test beam data.

In order to quantify the correlations of an observable  $\theta$  with the deviation of the reconstructed energy  $E_{\text{reco}}$  to the true energy  $E_{\text{beam}}$ , the pearson correlation coefficient is used:

$$\text{corr}(\theta, \Delta E) = \frac{\text{cov}(\theta, \Delta E)}{\sigma_{\theta} \sigma_{\Delta E}}, \quad (8.1)$$

$$\text{with } \Delta E = \frac{E_{\text{reco}}}{E_{\text{beam}}}, \quad (8.2)$$

where  $\text{cov}(X, Y)$  is the covariance matrix of two samples  $X$  and  $Y$ , and  $\sigma_{X/Y}$  are the corresponding standard deviations. Further,  $E_{\text{beam}}$  is the true energy. Note that a pure correlation between a variable and  $\Delta E$  does not necessarily indicate a high predictive power for corrections of the reconstructed energy. The variable further needs to be uncorrelated with the beam energy. Still the correlation with  $\Delta E$  is a reasonable hint for a variable to be useful for

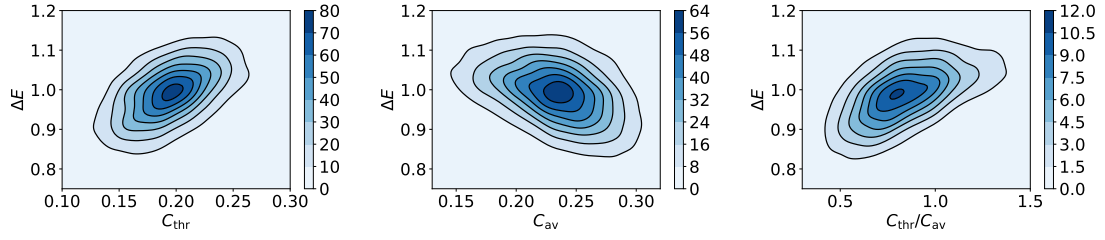


**Figure 8.1** – The deviation of the reconstructed energy from the true beam energy plotted over different hit energy related variables. The contour lines are calculated with a kernel density estimation (KDE) of the underlying data for visualization. *Left:*  $C_{thr}$ , *Middle:*  $C_{av}$ , *Right:*  $C_{thr}/C_{av}$ .

improving the reconstructed energy.

## 8.1 Correlation of Hit Energy Observables

In the original global software compensation approach [11] two observables are used: The fraction of hits with a reconstructed energy below a fixed threshold in an event and the fraction of hits in an event with a reconstructed energy below the average hit energy in that event. The ratio of both observables is used to correct the reconstructed energy for each event. Analogous to this we define:

$$C_{thr} = \frac{N(e_{hit} \geq \bar{e})}{N_{total}}, \quad (8.3)$$

$$C_{av} = \frac{N(e_{hit} \geq \overline{e_{hit}})}{N_{total}}, \quad (8.4)$$

$$C = \frac{C_{thr}}{C_{av}}, \quad (8.5)$$

where  $C_{thr}$  represents the fraction of hits with energies above a threshold  $\bar{e}$ , and  $C_{av}$  is the fraction of hits with energies above the average hit energy of that event. Throughout this thesis the threshold  $\bar{e}$  is set to 5 MIP (as in [11]), if not stated otherwise. In general, the performance of the global SC method depends only slightly on variations of this threshold. The two dimensional distributions of these variables and  $\Delta E$  are shown in fig. 8.1 across all beam energies. By eye, a strong correlation between all three observables and  $\Delta E$  can be observed. Figure 8.2 (*left*) shows the median of these observables for each energy together with the 50% central interval. As  $C_{av}$  is slightly decreasing with energy,  $C_{thr}$  is slightly increasing. Thus, the ratio of both is increasing from 0.6 to about 1.0 over the full energy range, which means that the average hit energy approaches  $\bar{e} = 5$  MIP for higher energies.

The correlation coefficients of those features with  $\Delta E$  across all beam energies are given in table 8.1. Figure 8.2 (*right*) shows the absolute value of the correlation coefficient as a function of the beam energy. A clear correlation of all three variables is observed. The

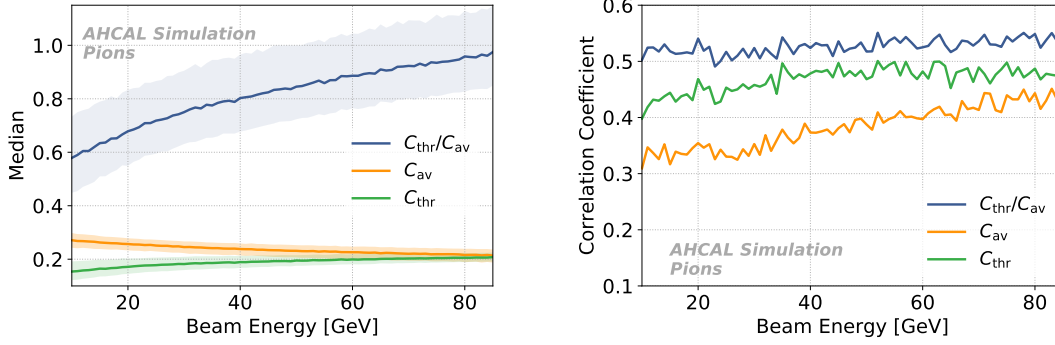


**Figure 8.2** – *Left*: Median value of several energy dependent observables across different beam energies for simulated pions. The shaded area gives the 50 % central interval of the distribution for each energy. *Right*: Absolute values of the correlation coefficient of these observables with the ratio of the reconstructed and the true beam energy.

correlation of  $C_{av}$  is negative, as also observed in [125]. Building the ratio of  $C_{thr}$  and  $C_{av}$  enhances the correlation slightly, indicating that both variables independently hold some uncorrelated information about  $\Delta E$ . The correlation coefficients are mostly stable with the beam energy. Only for  $C_{av}$  a mild increase with the beam energies is observed.

**Table 8.1** – Correlation coefficient of several features with  $\Delta E$ .

Feature	$C_{thr}$	$C_{av}$	$C_{thr}/C_{av}$
$\text{corr}(\theta, \Delta E)$	0.46	-0.36	0.49

For  $C_{thr}$  the intuition behind the correlation is that a shower with a high electromagnetic fraction,  $f_{em}$ , has a higher energy density leading to more high energetic hits. Thus, a positive correlation with  $f_{em}$  and consequently  $\Delta E$  is expected. For  $C_{av}$  the intuition is not as clear. For 40 GeV the average hit energy  $\overline{e_{hit}}$  is about 4.3 MIP, very close to the threshold energy of  $\tilde{e} = 5$  MIP. However, both observables have a different dynamic. While  $\tilde{e} = 5$  MIP is a constant,  $\overline{e_{hit}}$  changes from event to event with a standard deviation of  $\sigma_{\overline{e_{hit}}} = 1.1$  MIP. The hit energy distribution is highly skewed favoring low hit energies. In the case of a high electromagnetic fraction, the threshold  $\overline{e_{hit}}$  increases as the high energetic hits are pulling the mean. As a result, an event with a higher  $f_{em}$  is more likely to produce a lower  $C_{av}$  value leading to a negative correlation with  $\Delta E$ . Assuming an increase in low energetic hits, the mean hit energy  $\overline{e_{hit}}$  decreases and thus more hits are above this threshold. While  $C_{thr}$  changes in the same way (by  $\pm 1/N$ ) when a high or a low energetic hit is added, this is not the case for  $C_{av}$  and the behavior may depend heavily on the exact hit energy distribution of that event. This is the fundamental difference between the variables  $C_{av}$  and  $C_{thr}$ , explaining the increased correlation of the ratio of both variables with  $\Delta E$ .

## 8.2 Correlation of Hit Time Observables

The strong correlations which are found between the fraction of high energetic hits and the reconstructed energy motivate the search for other observables with similar correlations. In this section, the correlation of the hit time measurements with the reconstructed energy are studied and features for correcting the energy reconstruction are constructed.

### 8.2.1 Feature Construction

The hit time measurement may provide information about two processes in the hadronic shower: The process of elastic neutron scattering, which is expected to happen at time scales between 10 to 50 ns, and the capture of slow neutrons extending to times usually much later than 50 ns. All other processes in a hadronic shower are expected to be instantaneous with respect to the targeted time resolution.

The neutron content of a shower can give valuable insight into the processes happening in a hadronic shower and thus may be used to correct for parts of the fluctuations which determine the hadronic energy resolution. As shown in section 1.4.5 the neutron content of a hadronic shower is key for reaching offline compensation in an intrinsically non-compensating calorimeter. The amount of observed neutrons is expected to correlate with the amount of hadronic interactions in a hadronic shower. Additionally, the amount of neutrons in a shower is correlated with the amount of nuclear binding energy loss (see section 1.4.3).

There are two ways of constructing variables from the data set similar to the original global SC approach:

$$T_{\text{thr}} = \frac{N(t_{\text{hit}} \geq \tilde{t})}{N_{\text{total}}}, \quad (8.6)$$

$$T_{\text{edep}} = \frac{E(t_{\text{hit}} \geq \tilde{t})}{E_{\text{total}}}. \quad (8.7)$$

$$(8.8)$$

Here,  $T_{\text{thr}}$  is the fraction of hits in an event that are later than a fixed threshold  $\tilde{t}$  (in analogy to  $C_{\text{thr}}$  from above), while  $T_{\text{edep}}$  is the energy sum that is deposited after a time threshold. Using variables that are relative to the total number of hits or the total energy sum is advantageous, because those variables are expected to be much more stable across different beam energies than absolute values.

### 8.2.2 Time Resolution and Time Thresholds

The results of the correlation study of the observables designed above may depend on the threshold  $\tilde{t}$ . If the threshold is set too high, the fraction of hits above that threshold is very

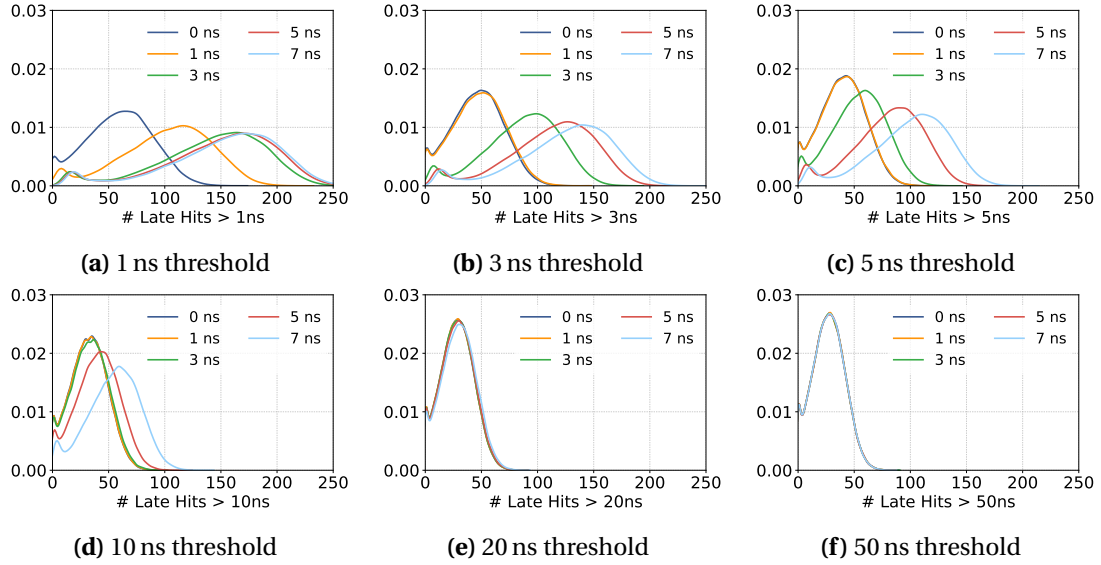


**Figure 8.3** – Distribution of the number of observed hits later than a certain threshold for 40 GeV pions and different time resolutions. The different figures are for different time thresholds (1, 3, 5, 10, 20, 50 ns).

low because of the exponential drop of the time distribution, leading to large statistical uncertainties in that variable. Setting the threshold too low may cause a substantial part of the instantaneous part of the shower being included in the variable, because of the finite time resolution. This means that the optimal threshold depends on the time resolution. Figure 8.3 shows the distribution of the number of hits later than a threshold of 1, 3, 5, 10, 20 and 50 ns ((a) - (f)) and time resolutions of 0, 1, 3, 5 and 7 ns (colored line). The scenario with a time resolution of 0 ns is the most optimal scenario assuming the best possible time resolution. The 1 ns case is the design goal of the AHCAL. For the LTP, currently a time resolution of about 5 ns seems to be feasible for test beam measurements.

For a time resolution of 1 ns a threshold of  $\tilde{t} = 3$  ns (equivalent to three standard deviations of the time resolution) seems to be optimal. The distribution overlaps nearly completely with the distribution of the data sample using the optimal resolution. This indicates that the number of late hits is not significantly affected by the instantaneous part of the time distribution. For a time resolution of 3 ns, a threshold of  $\tilde{t} = 10$  ns would be preferred with a significantly reduced number of late hits, leading to larger statistical uncertainties in these observables.

For the case of a 1 ns time resolution and a threshold of  $\tilde{t} = 3$  ns, on average about 50 hits are observed above the threshold. Assuming a poissonian distribution, the statistical error would be on average  $\sqrt{50} \approx 7$ , or 14%. Thus the statistical uncertainties on the number of late hits are expected to be smaller, but of the same order than the event by event fluctuations. With an optimal time resolution and a threshold of  $\tilde{t} = 1$  ns, about 70 late hits are observed on average leading to a reduced contribution of the statistical uncertainties compared to the

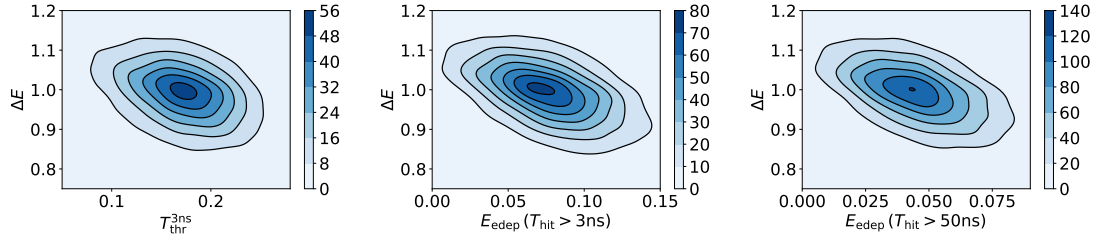


**Figure 8.4** – Different hit time related variables plotted over the deviation of the reconstructed energy from the true beam energy. The contour lines are calculated with a KDE of the underlying data for visualization. *Left:*  $T_{\text{thr}}^{3\text{ns}}$ , *Middle:*  $T_{\text{edep}}^{3\text{ns}}$ , *Right:*  $T_{\text{edep}}^{50\text{ns}}$ .

event by event fluctuations.

For the studies below a time resolution of 1 ns is assumed and several variables are selected:  $T_{\text{thr}}^{3\text{ns}}$ ,  $T_{\text{thr}}^{20\text{ns}}$  and  $T_{\text{thr}}^{50\text{ns}}$  defined as the fraction of hits in a shower later than 3, 20 and 50 ns respectively. The threshold of 3 ns is chosen to include as much of the late hits as possible. The threshold of 50 ns tries to separate the physics process of neutron elastic scattering ( $T_{\text{thr}}^{3\text{ns}} - T_{\text{thr}}^{50\text{ns}}$ ) and neutron capture. The threshold of 20 ns is an intermediate measure having more statistic than the 50 ns threshold. In addition, the fraction of deposited energies above the same time thresholds are considered:  $T_{\text{edep}}^{3\text{ns}}$ ,  $T_{\text{edep}}^{20\text{ns}}$ , and  $T_{\text{edep}}^{50\text{ns}}$ .

The distribution of three of these variables together with the distribution of  $\Delta E$  is shown in fig. 8.4. The corresponding correlation coefficients are given in table 8.2. All correlations are negative, as expected. More late hits are an indication for more neutrons, thus more hadronic interactions, leading to less reconstructed energy. It is interesting that the correlations do not degrade for the variables with higher time thresholds. Quite the contrary, if we select the neutron elastic part of the time distribution by subtracting the fraction of deposited energy after 50 ns from the fraction of deposited energy after 3 ns, the correlation drops. This indicated that the neutron capture process is more important for the energy reconstruction, even though there are much less hits falling into this category compared to the neutron elastic scattering process. Furthermore, the variables using the energy information show higher correlations than the ones counting the number of hits. One has to be careful in interpreting this difference, as with correlation coefficients in general. As the energy dependent variables are constructed dividing by the total reconstructed energy, it could be that part of the correlation arises from the construction of the variable.

**Table 8.2** – Correlation coefficient of several features with  $\Delta E$ .

Feature	$T_{\text{thr}}^{3\text{ns}}$	$T_{\text{thr}}^{20\text{ns}}$	$T_{\text{thr}}^{50\text{ns}}$	$T_{\text{edep}}^{3\text{ns}}$	$T_{\text{edep}}^{20\text{ns}}$	$T_{\text{edep}}^{50\text{ns}}$	$T_{\text{edep}}^{3\text{ns}} - T_{\text{edep}}^{50\text{ns}}$
$\text{corr}(\theta, \Delta E)$	-0.30	-0.28	-0.27	-0.40	-0.42	-0.41	-0.28

The dependence of a subset of the time observable on the beam energy is illustrated in fig. 8.5 (*left*). The median of most observables is relatively stable across different beam

energies. The slight increase with beam energy for the observable  $T_{\text{thr}}^x$  is due to the higher hit energy densities in the core of the shower. For higher beam energies the hit energies in the core of the shower increase more than the number of hits. In the outer part of the shower the hit densities are lower allowing for higher hit numbers with increasing energies. The 50 % quantile is decreasing significantly for higher beam energies. This is expected, since for higher energies more neutrons are produced which reduces the statistical uncertainties in these observables.

Figure 8.5 (*right*) shows the absolute values of the correlation coefficients separately for each beam energy. The observables constructed with the energy information ( $T_{\text{edep}}^{3\text{ns}}$  and  $T_{\text{edep}}^{50\text{ns}}$ ) have a higher correlation with  $\Delta E$  than the one constructed with the number of hit information ( $T_{\text{thr}}^{3\text{ns}}$ ). Increasing the threshold up to 50 ns does not worsen the correlation, while selecting the neutron elastic part with  $T_{\text{edep}}^{\text{N.el.}} = T_{\text{edep}}^{50\text{ns}} - T_{\text{edep}}^{3\text{ns}}$  significantly decreases the correlation coefficient. In general an increase in the correlation coefficient with energy is observed. The reason for this is the lower statistical uncertainties in these variables as shown in fig. 8.5 (*left*). The fact that the energy density increases with increasing energy explains why the correlation coefficient increases more with energy for the observable constructed with energy  $T_{\text{edep}}^x$  compared to the one shown using the number of hits  $T_{\text{thr}}^{3\text{ns}}$ .

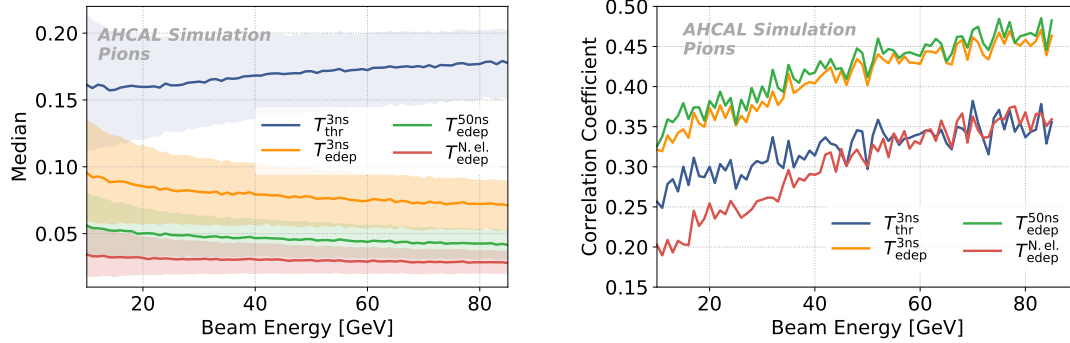


**Figure 8.5** – *Left*: Median value of several time dependent observables across different beam energies for simulated pions. The shaded area gives the 50 % central interval of the distribution for each energy. *Right*: Absolute values of the correlation coefficient of these observables with  $\Delta E$ .

### 8.3 Correlation of Shower Observables

Besides the observables constructed by the hit energies and the hit times, also global shower variables may hold correlations with the reconstructed energy. In this chapter four intuitive observables are studied similar to [126, 127]:

1. **Number of hits:** The number of hits in an event  $N$ . As the energy density changes, events with a higher  $f_{em}$  are expected to have less hits than events with more hadronic interactions.
2. **Shower radius:** The shower radius,  $R$ , is defined as the mean hit radius of the shower  $r_{hit}$ :

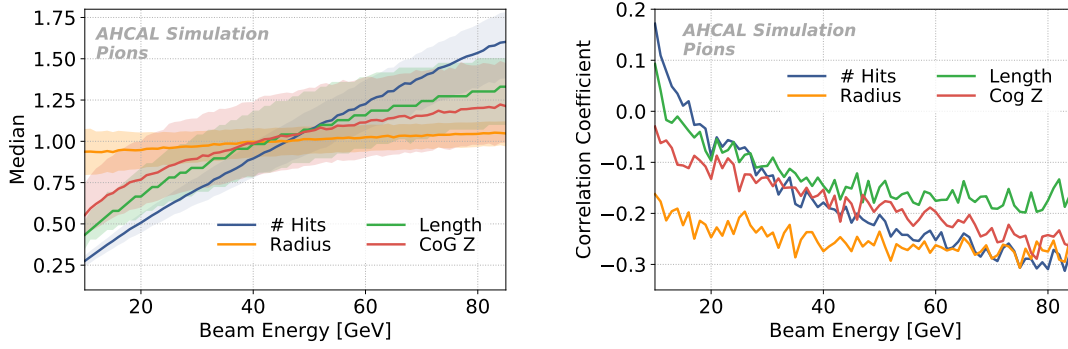
$$R = \frac{\sum_i r_{hit,i}}{N}, \text{ with } r_{hit} = \sqrt{(x_{hit} - cog_x)^2 + (y_{hit} - cog_y)^2}, \quad (8.9)$$

where  $x_{hit}$  and  $y_{hit}$  are the  $x$ - and  $y$ -position of each hit and  $cog_x$  and  $cog_y$  are the energy weighted center of gravity in  $x$ - and  $y$ -direction. Showers with a high hadronic component are expected to have a larger shower radii as the shower is less dense.

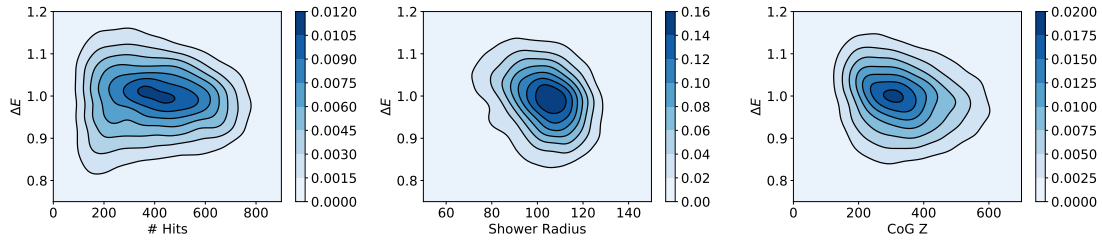
3. **Shower length:** The length of the shower is defined as the number of layers from shower start to shower stop. The shower stop is calculated the same way as the shower start, but from the back of the detector. In general, electromagnetic showers are shorter than hadronic ones. Thus a shorter shower could indicate a higher  $f_{em}$ .
4. **CoGZ:** The center of gravity in  $z$ -direction is the energy weighted center of gravity of the shower in longitudinal direction. The reasoning why the expected behavior depends on  $f_{em}$  follows the one for the shower length.

Figure 8.6 (*left*) shows the distribution of the median values of these observables for different beam energies. As the beam energy rises, the showers have on average more hits and extend further in radial and longitudinal direction. The correlation coefficients of these variables with  $\Delta E$  are shown in fig. 8.6 (*right*) for every beam energy. As reasoned above, most correlations with the beam energy are negative. For low energies there is a positive correlation with the number of hits. This is due to the larger statistical fluctuations for lower energies, where the number of observed hits is directly correlated with the visible energy depositions. For higher energies a relatively high number of hits is more an indication of a low  $f_{em}$ .

The two dimensional distributions of these variables over  $\Delta E$  for all energies are shown in fig. 8.7. Contrary to the hit energy and the hit time dependent observables, no clear correlation is visible across all beam energies. The reason for this lies in the strong correlation of these variables with the beam energy. This indicates that the shower observables are not useful for enhancing the energy reconstruction with low complexity algorithms such as the



**Figure 8.6** – *Left*: Median value of several shower observables across different beam energies for simulated pions. The distributions are shifted and scaled to be overlaid for better comparability. The shaded area gives the 50 % central interval of the distribution for each energy. *Right*: Correlation coefficient of these observables with the reconstructed energy.



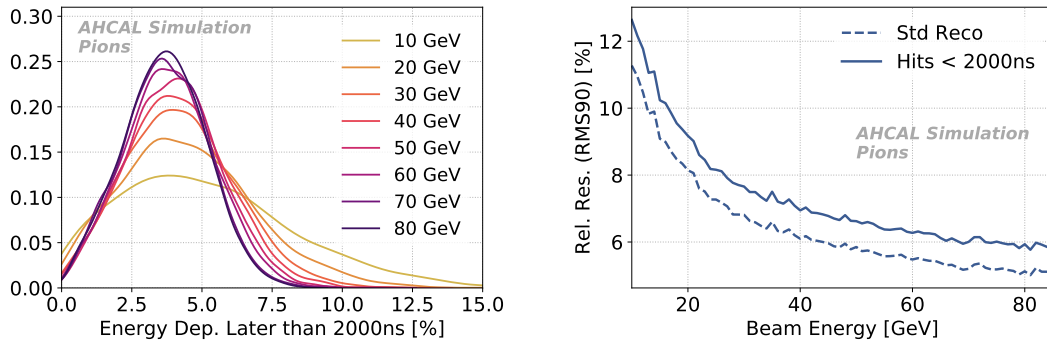
**Figure 8.7** – Different shower observables plotted over the deviation of the reconstructed energy from the true beam energy. The contour lines are calculated with a KDE of the underlying data for visualization. *Left*: Number of hits, *Middle*: shower radius, *Right*: center of gravity in  $z$ -direction.

global software compensation approach. However, multivariate methods as discussed in chapter 10, may be able to use the information stored in these observables. This was already demonstrated with a cluster based method in [127].

## 8.4 Limited Integration Time

As pointed out above, the assumption of capturing all late hits may not be valid at test beam campaigns or future experiments. The *test beam mode* of the current AHICAL readout chip assumes a bunch crossing length of 4000 ns over which data is taken and associated to the same event. In the so called *ILC mode*, this decreases to about 200 ns which is the expected bunch crossing length at a future linear  $e^+e^-$ -collider. In this section, the influence of the non-detected late hits on the energy resolution is studied. For this study, we assume an integration time of 2000 ns and consequently remove all hits later than that from the MC events. This time cut is also realistic for current AHICAL test beam campaigns running in *test beam mode*.

The distribution of the fraction of energy that is deposited later than 2000 ns is shown in



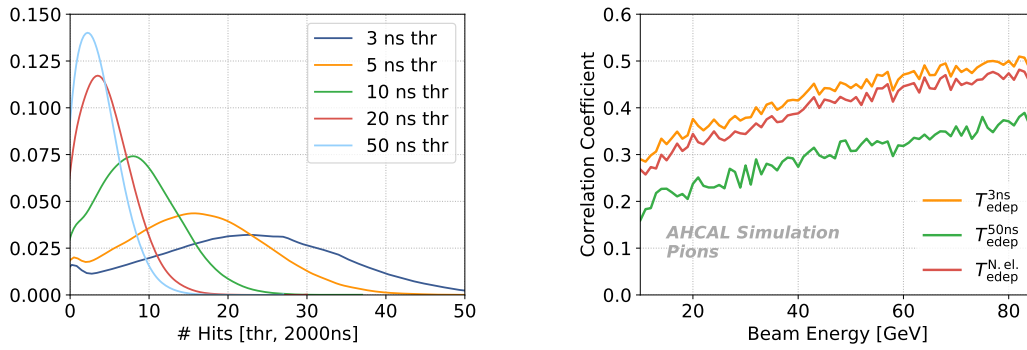
**Figure 8.8** – *Left*: Distribution of energy depositions later than 2000 ns. *Right*: Energy resolution of standard reconstruction for full integration time compared to a limited integration time of 2000 ns.

fig. 8.8 (*left*) for selected energies. On average this amounts to about 4 % for all energies. Most importantly, it can be seen that this number is subject to large event to event fluctuations. Because of lower statistics in the energy measurement, these fluctuations are especially large for low energies and seem to saturate around 70 GeV. The slight extension of the curves to values below zero is due to the KDE interpolation of the data for better visibility.

The large fluctuations in the amount of very late hits lead to a significant reduction of the energy resolution compared to the case with infinite measurement length, as depicted in fig. 8.8 (*right*). On average, the resolution decreases by about 14 %. The decrease is slightly smaller for lower energies than for higher energies. Even though the fluctuations are larger for lower energies, they are more dominant for the higher energies.

A finite measurement length has a large impact on the variables defined in section 8.2.1. The number of late hits is shown exemplarily in fig. 8.9 (*left*) for 40 GeV pions. For the 3 ns threshold, the number of late hits are about halved leaving around 25 on average. The influence of the time resolution becomes now even more important, as setting the threshold to higher values further reduces this number significantly. For a 10 ns threshold, on average less than ten late hits remain. Because of the flatness of the time distribution in the neutron capture regime, these numbers change only slightly when the integration time is reduced to several hundreds of ns or increased it to several  $\mu$ s.

The correlations between three of the variables constructed in section 8.2.1 with the reconstructed energy in the case of a finite integration time is illustrated in fig. 8.9 (*right*). Comparing the correlation coefficients to those found in section 8.2 without the restricted integration time, several differences can be identified. For  $T_{\text{edep}}^{3\text{ns}}$  (the energy deposited later than 3 ns), the correlation with the reconstructed energy increases slightly. Not surprisingly, the correlation for  $T_{\text{edep}}^{50\text{ns}}$  is reduced considerably by about a third over the whole energy range, as the number of late hits get very low in the time interval between 50 ns and 2000 ns. In contrast, the correlation coefficient for  $T_{\text{edep}}^{N.el.}$  increases over the whole energy range by about a third. This observation hints at an increased importance of the neutron elastic



**Figure 8.9** – *Left*: Distribution of the number of hits later than different thresholds up to times of 2000 ns for 40 GeV. *Right*: Correlation of time variables with reconstructed energy. Only hits earlier than 2000 ns are considered.

scattering part in the case of a limited integration length.

As neutron capture happens with high probability only at very low (thermal) energies, the neutrons have to be thermalized before by elastic scattering. This happens to a large extent also in the scintillator, which leads to detectable signals. This means that the neutron elastic processes are causally happening before the neutron capture. Thus, a strong correlation between both processes is expected. As shown in fig. 8.10 (*left*), indeed a very strong correlation between the energy depositions in the neutron elastic regime and the energy depositions later than 2000 ns is observed in the simulation. From this a linear relationship can be inferred and the ratio between both observables is stable across energies (see fig. 8.10, *right*).

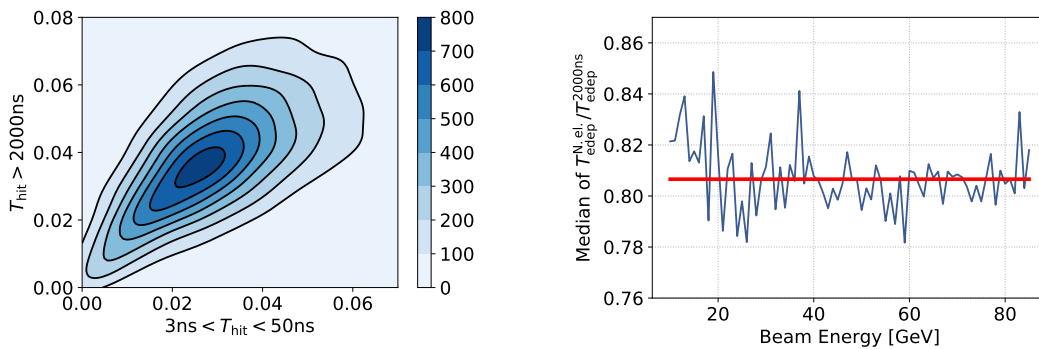


**Figure 8.10** – *Left*: Correlation between energy deposited in neutron elastic regime 3 to 50 ns and very late energy depositions > 2000 ns. *Right*: Fraction of energy deposited in neutron elastic regime 3 to 50 ns and very late energy depositions > 2000 ns for all beam energies.

## 8.5 Test Beam Data Correlations

For comparing the simulation results with test beam data, only the first 38 layers of the simulation are considered and all observables are recalculated accordingly. Figure 8.11 (*left*) compares the median of the hit energy dependent observables between the simulation and test beam data for different beam energies. For all energies the median value of the distributions are slightly higher in simulation than for test beam data. The overall dependence of these variables with the beam energy is the same. The absolute value of the correlation coefficients of these variables with the reconstructed energy are shown in fig. 8.11 (*right*). For  $C_{\text{thr}}/C_{\text{av}}$  and  $C_{\text{thr}}$  a slightly smaller correlation coefficient in data is observed compared to simulation. In general the correlation of the hit energy dependent observables with the reconstructed energy is stronger with the 38 layers simulation as for the 60 layers simulation shown in fig. 8.2 (*right*). As opposed to the 60 layers simulation, the correlation coefficients of  $C_{\text{av}}$  for higher beam energies gets stronger compared to  $C_{\text{thr}}$ . This suggests at an increased importance of  $C_{\text{av}}$  in the presence of leakage.

The results for the correlations of the shower observables are shown in fig. 8.12. In general good agreement between data and simulation is observed. The only larger deviations observed are for the correlation coefficients of the number of hits and the center of gravity in  $z$ -direction with the reconstructed energy. This could be again due to a higher electron contamination at the low energies.

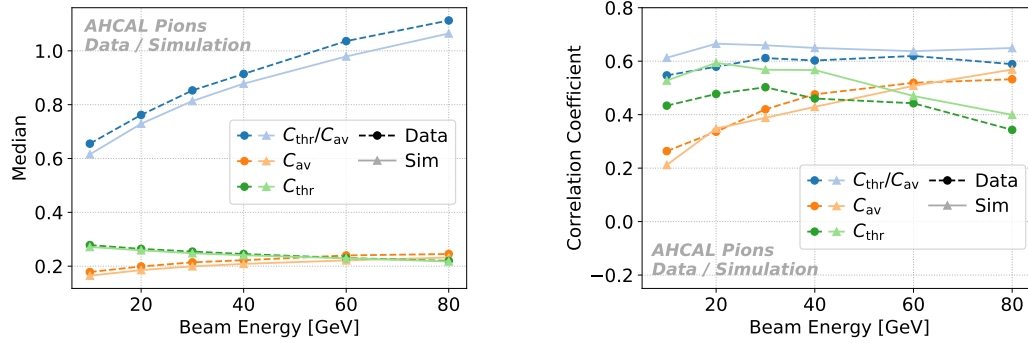


**Figure 8.11** – *Left*: Median value of several energy dependent observables across different beam energies for simulated pions (38 active layers) compared to test beam data. *Right*: Absolute values of the correlation coefficient of these observables with  $\Delta E$ .

## 8.6 Conclusions

In this chapter, the correlation of various observables with the ratio of reconstructed and true energy  $\Delta E$  of a highly granular calorimeter were investigated. Three different observables depending on the hit energies were defined accordingly to [125]. The observations made for the physics prototype, like the sign of the correlations, could be confirmed for simulations of

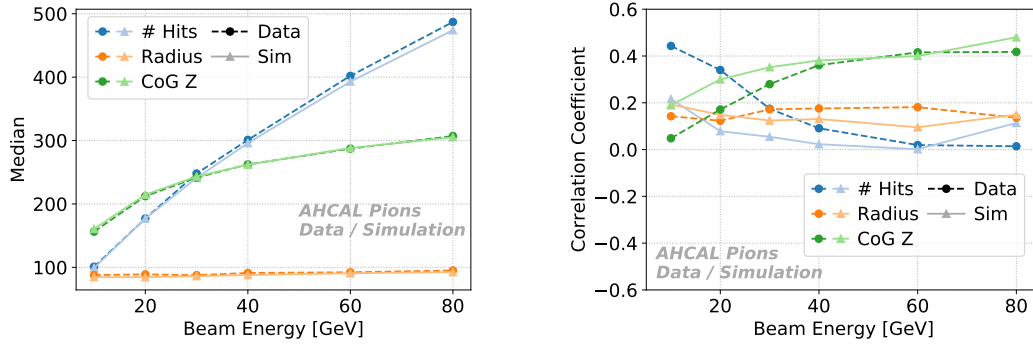


**Figure 8.12** – *Left*: Median value of several shower observables across different beam energies for simulated pions (38 active layers) compared to test beam data. *Right*: Absolute values of the correlation coefficient of these observables with  $\Delta E$ .

the LTP. Most importantly, it was found that the ratio  $C_{\text{thr}}/C_{\text{av}}$  has a higher correlation with  $\Delta E$  than  $C_{\text{thr}}$  or  $C_{\text{av}}$  separately. Additionally, the correlations of several shower observables were analyzed. Their behavior is observed as expected for hadronic showers. As these variables, e.g., the number of hits, also correlate highly with the beam energy, their use for correcting the reconstructed beam energy is expected to be limited.

Several variables were constructed in order to quantify the properties of a hadronic shower in the time domain. With infinite integration time, strong correlations between these time variables with the deviation of the reconstructed energy to the true energy are observed. In general, observables summing up the energy above a time threshold are found to hold stronger correlations than observables counting the number of hits over a time threshold for an event. Surprisingly, setting the time threshold to higher values, e.g., from 3 ns to 50 ns does not decrease the correlation. However, considering hits between 3 ns and 50 ns lowers the correlation considerably. This leads to the conclusion that the neutron capture part later than 50 ns has more potential for correcting the reconstructed energy than the neutron elastic part from 3 to 50 ns.

Limiting the integration time of the events to 2000 ns significantly reduces the energy resolution by about 14 %. The captured neutrons release binding energy that was lost earlier in the generation of free neutrons, which limits the effect of the fluctuations of invisible energy on the energy resolution. This highlights that the detection of neutron capture processes is important for an excellent performance of an intrinsically non-compensating calorimeter.

As in the scenario with the limited integration time the access to the neutron capture part of the shower is significantly reduced, the correlation of the neutron elastic part with the reconstructed energy is dominating. The reason for this lies in the strong correlation of the neutron elastic part with the neutron capture part. It opens up the opportunity to recover the undetectable part of the neutron capture regime by using the event information of the neutron elastic scattering.

Finally, test beam data and simulations are compared. In general, the correlations for

the hit energy dependent observables and the shower observables are in good agreement between data and simulation. In the next chapter, it is investigated whether these results can be exploited in order to enhance the energy reconstruction.

## Chapter 9

# Time Assisted Energy Reconstruction

The correlations between the energy and the time measurements found in chapter 8 have the potential to enhance the energy reconstruction. In this chapter it is studied how this can be achieved and how the improvements compare to traditional software compensation (SC) approaches. These studies are performed on simulated data using the geometry described in section 7.3.

### 9.1 Correcting for Limited Integration Time

In section 8.4 it is found that the limitation of the integration time, i.e., the time over which hits are associated with a given event, leads to a decrease of the energy resolution. At the same time a strong correlation of the energy deposited in the neutron elastic scattering regime and the very late part of the shower is observed. The relation between the neutron elastic and the neutron capture part is found to be linear and not dependent on the beam energy. This can be used to correct the reconstructed energy by recovering the non measurable energy depositions later than 2000 ns with a simple correction factor on event basis:

$$E_{\text{corrected}} = a_{\text{calibr.}} E_{\text{std}} (1 + C_{\text{corr}} T_{\text{edep}}^{\text{N.el.}}). \quad (9.1)$$

The correction factor  $C_{\text{corr}} = 1.24$  is given by the median of the values empirically found in fig. 8.10 and is taken to be the same for all energies and events. The global calibration constant  $a_{\text{calibr.}}$  is necessary in order to shift the energy distributions back to the correct beam energy values. The procedure is the same as for the standard reconstruction. Note that the form of the correction above can also directly derived from eq. (1.21).

The results of this approach are given in fig. 9.1. The first panel shows the relative resolution defined as

$$\text{Relative Resolution} = \frac{\text{RMS}_{90}(E_{\text{reco}})}{E_{\text{beam}}}. \quad (9.2)$$

With the RMS being evaluated only on the 90 % central interval. The improvement over the

standard reconstruction is depicted in the second panel. It is defined as

$$\text{Improvement} = 1 - \frac{\text{RMS}_{90}(E_{\text{reco}})}{\text{RMS}_{90}(E_{\text{std}})}. \quad (9.3)$$

In the third panel the linearity is shown, with

$$\Delta E = \frac{\text{mean}_{90}(E_{\text{reco}})}{E_{\text{beam}}} - 1. \quad (9.4)$$

These definitions stay consistent for similar subsequent figures.

On the sample with limited integration time the energy resolution after correction improves significantly compared to the standard reconstruction. The relative improvement gets larger for higher energies. Especially for larger energies most of the initial resolution without integration time can be recovered. This correction method is essentially a boosting of the calorimeter response of the neutron elastic processes in the scintillator. It aims at directly recovering parts of the energy lost due to invisible binding energy.

The success of this simple approach underlines the strong correlation of the time observables in the AHCAL with processes in the hadronic shower. It is a direct benefit of the hit-by-hit time capabilities of the AHCAL. In the next section this will be further developed in a SC like scheme and compared to traditional observables exploiting the energy density and the distribution of hit energies of the shower.

## 9.2 Global Software Compensation

In order to correct the reconstructed energy, a simple approach to global software compensation (SC) is used. The standard reconstruction energy  $E_{\text{std},i}$  of event  $i$  is weighted by a function  $\omega$  depending on observables  $\theta_i$ :

$$E_{\text{SC},i} = E_{\text{std},i} \omega(\theta_i). \quad (9.5)$$

The weights are represented by a second order polynomial of the event observable with parameters  $a$ ,  $b$  and  $c$ :

$$\omega(\theta) = a + b\theta + c\theta^2. \quad (9.6)$$

These parameters are determined by minimizing the function below:

$$\chi^2 = \sum_i \frac{(E_{\text{std},i} (a + b\theta_i + c\theta_i^2) - E_{\text{beam},i})^2}{E_{\text{beam},i}}, \quad (9.7)$$

where the sum runs over all events and  $E_{\text{beam}}$  is the beam energy. This method differs slightly from the approach described in [11]. Here, the goal is to have a simple and robust method for advanced energy reconstruction, where different features  $\theta$  can easily be used and compared

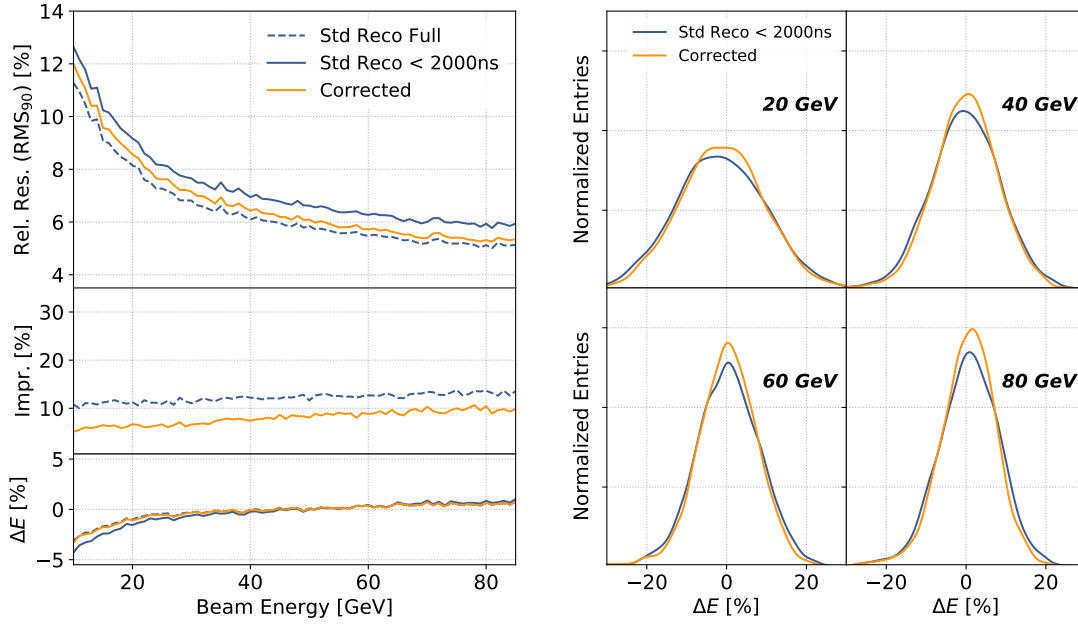


**Figure 9.1** – *Left*: Energy resolution, improvement and linearity for standard reconstruction with no integration time, standard reconstruction with 2000 ns integration time and corrected energy with 2000 ns integration time. The improvement is understood relative to the standard reconstruction with 2000 ns integration time. *Right*: Energy distributions for 20, 40, 60, 80 GeV. The data is smeared with a KDE and normalized for better visibility.

without extended optimization of the method to the given feature.

### 9.2.1 Energy Observables

In a first step the procedure described above will be studied with observables describing the hit energy distribution of an event. Figure 9.2 shows the energy resolution using the SC approach for  $\theta = C_{\text{thr}}$  and  $\theta = C_{\text{thr}}/C_{\text{av}}$  (green). Both approaches are compared to the standard reconstruction (blue), to the energy resolution of the time correction discussed in section 8.4 (orange broken lines), as well as applying this correction before the SC procedure (dark green broken lines). The SC approach for  $\theta = C_{\text{thr}}$  gives on average about 15 % improvement over the standard reconstruction. The improvement is slightly lower for the lowest energies below 40 GeV. The linearity improves over the standard reconstruction especially for low energies. Applying the time correction before the SC procedure significantly increases the resolution to about 20 % improvement over the standard reconstruction. This means that both approaches are correcting for different effects that are to some degree uncorrelated and the combination of both indeed is beneficial.

Using  $\theta = C_{\text{thr}}/C_{\text{av}}$  as the observable for SC gives significantly better results (see fig. 9.2 *right*), even though the improvement is more dependent on the energy. For energies above 40 GeV about 25 % improvement over the standard reconstruction are achieved. For energies

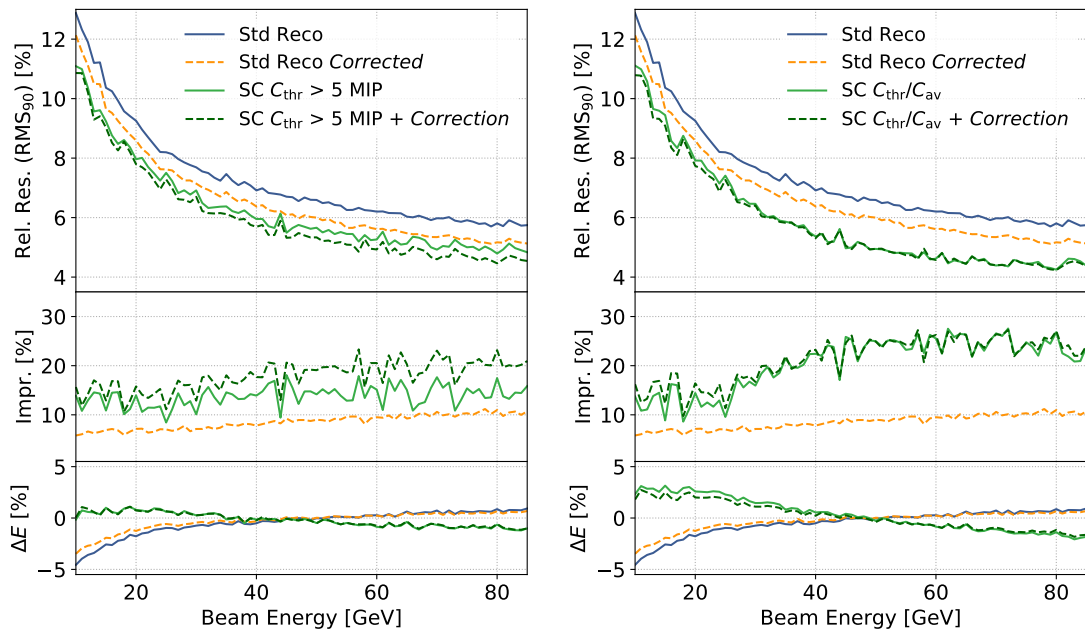


**Figure 9.2** – Energy resolution, improvement and linearity shown for the SC approach using  $C_{thr}$  (left) and  $C_{thr}/C_{av}$  (right). Shown are the standard reconstruction, the time correction described in section 8.4, the SC results as well as results for applying the time correction before SC.

below 30 GeV the improvement is on average only about 13 % and comparable to the results of  $\theta = C_{thr}$ . Applying the time correction before SC leads to a very mild improvement in resolution only for the lowest energies. For energies above 30 GeV, the resolution does not improve significantly with the time correction. In this case, the same information seems to be accessible via observables of the hit energy spectrum.

The linearity is worse for the approach using  $\theta = C_{thr}/C_{av}$ . This is of no concern, as the linearity can easily be restored by a linearity correction (e.g., multiplying the reconstructed energy by  $a + b E_{reco}$ ). This may have a slight influence on the relative energy resolution as it is divided by the absolute reconstructed energy. Nevertheless, the improvement shown in the second panel of Figure 9.2 stays stable.

### 9.2.2 Time Observables

As large correlations with the reconstructed energy are also seen for time observables, the same approach is studied for  $\theta = T_{edep}^{3ns}$ . The results are presented in fig. 9.3 (left). A clear improvement over the standard reconstruction can be seen. The improvement increases from about 8 % for low energies and up to about 19 % for the highest energies. With this, the improvement is significantly larger than for the simple time correction and of similar size as for the energy observable  $\theta = C_{thr}$ . However, the improvement is much smaller than the one for  $\theta = C_{thr}/C_{av}$ . The energy resolution cannot be further improved by applying

the time correction before the SC. This is expected, as both corrections are using the same information.

### 9.2.3 Combining Energy and Time Observables

An interesting question is whether the combination of both the energy and the time observables lead to an improvement in a SC like approach. In order to study this, the SC procedure is adapted such that eq. (9.7) is able to handle two independent observables  $\theta_1$  and  $\theta_2$ :

$$\chi^2 = \sum_i \frac{\left( E_{\text{std},i} \left( a + b\theta_{1,i} + c\theta_{1,i}^2 + d\theta_{2,i} + e\theta_{2,i}^2 + f\theta_{1,i}\theta_{2,i} \right) - E_{\text{beam},i} \right)^2}{E_{\text{beam},i}}. \quad (9.8)$$

Besides the quadratic dependence on each of the two features, a correlation term is added as well. By this extension, the number of parameters increases from three to six ( $a$  to  $f$ ). The other parts of the procedure are the same as above.

The results of this method using  $\theta_1 = C_{\text{thr}}/C_{\text{av}}$  and  $\theta_2 = T_{\text{edep}}^{3\text{ns}}$  are shown in fig. 9.3 (*right*). A mild improvement over the SC approach using only the  $\theta = C_{\text{thr}}/C_{\text{av}}$  feature can be observed. The improvement is larger for lower energies. If we use  $\theta_1 = C_{\text{thr}}$  and  $\theta_2 = T_{\text{edep}}^{3\text{ns}}$  a clear improvement of adding the time observable is seen over the SC case where only  $\theta = C_{\text{thr}}$  is used (see fig. A.2 (*left*) in appendix A.3). As a cross check the procedure is also done with  $\theta_1 = C_{\text{thr}}$  and  $\theta_2 = C_{\text{av}}$  (see fig. A.2 (*right*)), leading to the same results as only using the  $\theta = C_{\text{thr}}/C_{\text{av}}$  observable. This shows that the slight improvement of adding the time information to the SC method is not simply arising due to the increased number of parameters.

### 9.2.4 Why Do the Hit Energy Observables Perform so Well?

So far it could be shown that the energy resolution can be enhanced significantly over the standard reconstruction procedure by exploiting the hit time observables of a shower. However, no improvement over the method which is using the hit energy observables is achieved. Furthermore, using both, hit time and hit energy observables only leads to very small improvements. This suggests that the information provided by the time observables are already incorporated in the hit energy observables.

In order to explain why the hit energy observables perform so well, it is instructive to look at the correlations of the hit time observables and the hit energy observables with the reconstructed energy together. This is done in Figure 8.7. The data of 45 to 55 GeV pions is binned with respect to the hit time observable  $T_{\text{edep}}^{3\text{ns}}$  on the  $x$ -axis and hit energy observables ((**a**)  $C_{\text{thr}}$  (**b**)  $C_{\text{av}}$  (**c**)  $C_{\text{thr}}/C_{\text{av}}$ ) on the  $y$ -axis. The color coding represents the mean deviation of the reconstructed energy to the true energy for each bin ( $\Delta E$ ). In (**a**) and (**b**) it can be seen that both, the hit energy as well as the hit time observable, are correlated with the reconstructed energy. Both variables are necessary in order to point to an area of same color. This is not true for (**c**). Here the lines of same color are parallel to the  $x$ -axis, meaning that

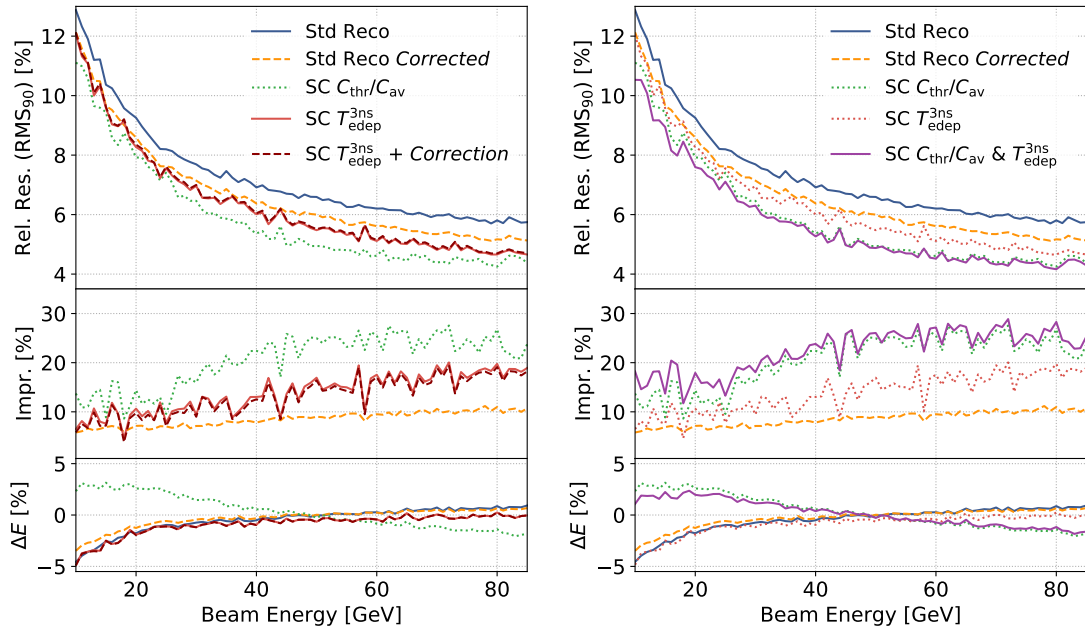


**Figure 9.3** – Energy resolution, improvement and linearity shown for the SC approach using  $T_{\text{edep}}^{3\text{ns}}$  (left), and  $C_{\text{thr}}/C_{\text{av}}$  and  $T_{\text{edep}}^{3\text{ns}}$  (right). Shown are the standard reconstruction, the time correction described in section 8.4, the SC results and the results for applying the time correction before SC.

the time observable does not add much additional information that is valuable in order to predict the deviation of the reconstructed energy to the true energy.

It can be concluded that by using  $C_{\text{thr}}/C_{\text{av}}$  as an observable for the global software compensation approach, the time observable does not add significant valuable information. However, it is not  $C_{\text{thr}}$  or  $C_{\text{av}}$  alone that hold this information, but the fraction of both. This means that variables derived from the hit energy spectrum of an event are capable of being sensitive to similar physics processes as variables related to the hit time spectrum.

### 9.3 Conclusions

In this chapter it was shown that the hit time information of a highly granular calorimeter can be used to exploit the strong correlations between the neutron elastic processes and the neutron capture processes in a hadronic shower. A procedure was presented using the relative energy depositions in the neutron elastic time regime up to 50 ns to correct the reconstructed energy for very late energy depositions that are outside of the integration time window of the data acquisition. This method artificially boosts the calorimeter response to the neutron elastic scattering processes in the scintillator. Up to 70 % of the initial energy resolution can be recovered with this method. The improvement in energy resolution is larger for higher energies, as the statistics of the time observables are increasing with the beam

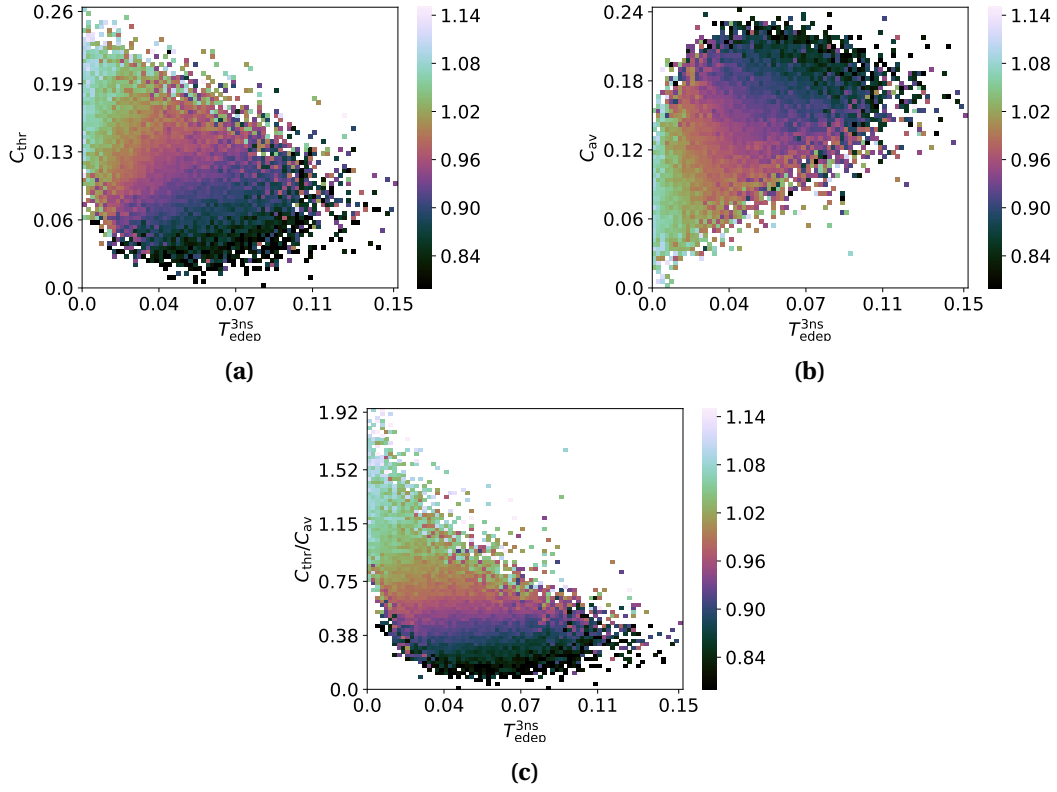


**Figure 9.4** – The color scale represents the mean value of  $\Delta E$  for simulated pions in the range from 45 to 55 GeV. The data is binned with respect to  $T_{\text{edep}}^{3\text{ns}}$  on the  $x$ -axis and (a)  $C_{\text{thr}}$  (b)  $C_{\text{av}}$  (c)  $C_{\text{thr}}/C_{\text{av}}$ .

energy of the event. A time resolution of 1 ns is necessary for a good performance because of the steeply falling time distribution of hadrons in the neutron elastic scattering regime.

Furthermore, a robust and energy independent version of the global SC approach was presented and was used to compare the predictive power of several hit energy and hit time dependent variables with respect to the reconstructed energy. It was shown that the  $C_{\text{thr}}/C_{\text{av}}$  observable leads to higher improvements than each of the two involved observables separately. For higher energies above 40 GeV, an average improvement of about 25 % is observed, which is close to the results found for global and local SC for the physics prototype [11]. Applying the correction for the limited integration time does not improve the energy resolution when the global SC approach is used with  $C_{\text{thr}}/C_{\text{av}}$ .

The same global SC approach was used with time dependent observables. An improvement of about 15 % over the standard reconstructed energy resolution was observed. The improvement is comparable to the one achieved with the  $C_{\text{thr}}$  observable and larger than the one for the linear time correction presented in section 8.4. The linear time correction is only correcting for the late energy depositions that are not observed because of the limited integration time. The minimization procedure of the global SC is capable of further weighting

the neutron response of the calorimeter up.

The combination of different observables for an enhanced energy reconstruction was studied by extending the global SC approach. By combining the  $C_{\text{thr}}$  with  $T_{\text{edep}}^{3\text{ns}}$  a clear improvement of the energy resolution over the case using just one of the two variables is observed. The total improvement is comparable to the improvement using  $C_{\text{thr}}/C_{\text{av}}$  with a better resolution at lower energies and a worse resolution for higher energies. Combining  $T_{\text{edep}}^{3\text{ns}}$  with  $C_{\text{thr}}/C_{\text{av}}$  leads to very moderate improvements at low energies. It was shown that  $C_{\text{thr}}/C_{\text{av}}$  and the hit time observable  $T_{\text{edep}}^{3\text{ns}}$  are highly correlated with respect to the reconstructed energy. This is an important insight, showing that in a highly granular calorimeter information connected to the hit time distribution of a shower is accessible via hit energy observables.

It should be noted that the presented simulated setup is idealized, because only single showers are considered. The late energy depositions are predominantly located at the outer part of the shower. Especially for particle jets at future  $e^+e^-$ -collider experiments, the outer parts of several hadronic showers may overlap. Therefore the assignment of late energy depositions to a certain hadronic shower might get ambiguous.

In the next chapter it is investigated whether the lack of improvement in energy resolution for added hit time dependent observables over the sophisticated hit energy observables can be overcome by more complex machine learning algorithms.

## Chapter 10

# Multivariate Energy Reconstruction

In this chapter, we evaluate if machine learning algorithms can make better use of the information that is encoded in the observables used in chapter 9. Furthermore, the developed machine learning framework is used to explore whether using several global and semi-global event observables can further enhance the energy resolution.

In [126] a neural network approach to global SC was studied using five input variables of clustered hadronic showers, similar to the ones described in section 8.3. The neural network framework described in this thesis is build upon modern machine learning packages and is capable of integrating a large number of input features into the model.

### 10.1 Artificial Neural Networks

Among machine learning algorithms, artificial neural networks (throughout this thesis called neural networks) are one of the most powerful and widely used methods. Due to the advent of hardware and algorithms which are capable to effectively train large networks new network architectures with many layers are emerging. These deep neural networks, are outperforming other algorithms at a wide variety of tasks ranging from image recognition [128] to natural language processing [129] and playing complex board games [130]. Relatively simple neural networks with a small number of nodes are well established within high energy particle physics for example as algorithms for b-tagging [131], or as triggers [132]. Recently, more complex, deep neural networks are also studied for problems as diverse as the search for exotic particles [133], jet tagging [134] or the fast simulation of particle showers [135, 136]. Most of these problems have in common that the algorithm needs to deal with large amount of highly correlated input data. This makes them highly suitable also for energy reconstruction, especially in highly granular calorimeters.

A neural network is based on a set of nodes (called *neurons*), which are organized in layers. A neuron has one or several inputs and one or several outputs. An activation function determines the outputs on the basis of the input signals. Weights can be applied to

each connection between neurons, thus enhancing or decreasing the importance of the connection. The weights are then trained in such a way that the specified *loss function* is minimized. A neural network typically has an input layer given by the input features and an output layer which provides the output of the network. Layers in between are called *hidden layers*. A network in which each neuron of is connected to each neuron of the following layer is called a *fully connected network*. Because of the large number of possible connections, neural networks with more than one hidden layer and many neurons are very powerful in finding hidden patterns in highly correlated, high dimensional data.

Due to the large number of free parameters (the trainable weights), a common problem of neural networks is overfitting. Overfitting may occur if a model is too closely fit to a limited set of data points. Instead of modeling the overall behavior of the dataset, the model represents more the fine structure of the data which may occur because of noise and random variations in the data point. This may lead to a significant decrease in performance of the predictive model. A proper regularization of the network can counter this problem. There are a number of different regularization schemes available. One of them is to add so called *dropout layers* to the network [137]. A dropout layer randomly drops a certain fraction of the connections between subsequent layers and thus forces the network to better generalize.

### 10.1.1 Pre-Processing

A crucial part in employing neural networks is the handling of the input data. As neural networks with a high number of neurons have many degrees of freedom, the networks are particularly prone to overfitting. This section will discuss extra preprocessing steps that are performed on the data in order to avoid overfitting and enhance the training process of the network.

#### Splitting of the Data Set

To avoid overfitting, the data set is split into three sets: 56 % of the data set are used for training; 14 % are used for validation during the training process; and 30 % are used for testing, i.e., evaluating the precision of the algorithm only after the training process. The size of the datasets were chosen such that the training data set is as large as possible, while the validation and testing data sets are just large enough to monitor the achieved accuracy with low statistical fluctuations.

#### Balanced Training Data

The training data should be quasi-continuous with respect to the energy resolution in order to avoid overfitting of patterns in the binning of the training beam energies. If the binning of beam energies is too coarse this pattern could be picked up by the algorithm, and may lead to an artificially enhanced energy resolution. Using training data on a wide range of

energies from 10 to 85 GeV in 1 GeV steps is found to be fine enough, as the distributions of the reconstructed energies overlay significantly over the range of several beam energies. Further, it is beneficial to balance the training data, i.e., having about the same number of data points for each beam energy, which is the case for the given data set.

### Normalized Input Variables

In order to make the input variables  $\theta_j$  comparable, the distribution of input variables is normalized to zero mean and a standard deviation of one across all beam energies:

$$E[\theta_j] = 0 \quad (10.1)$$

$$\text{Var}[\theta_j] = 1, \quad (10.2)$$

where  $j$  represents the different input features. This assures that all variables are comparable in size and no too large values occur.

### Feature and Target Variable Selection

A well known problem of using neural networks for regression is the overfitting of the edges of the energy spectrum. This results in strong non-linearities and usually in a too optimistic precision for the extreme energies. The reason for this is that the network learns the bounds of the range of training energies and uses this information to artificially enhance the energy resolution for these energies in order to artificially lower the loss function. A recent approach to solve this problem for low energetic particles in a simulation of an electromagnetic calorimeter is modifying the loss function in an analytic way to account for the boundaries of the training energy range [138]. For the present study, this approach is found to be not suitable, as a key assumption of gaussian energy distributions is heavily violated for hadronic showers.

Instead, this study uses input features that are as little as possible correlated to the beam energy. This means that features such as the energy reconstructed by standard reconstruction  $E_{\text{std}}$  or the number of hits are not used at all. A natural selection for the target variable that should be predicted by the network would be the energy in GeV. This approach would require input features that are highly correlated with the reconstructed energy, leading to the problem described above. Instead, this is overcome by training on a correction factor  $\Delta E$  instead:

$$\Delta E = \frac{E_{\text{std}}}{E_{\text{beam}}}, \quad (10.3)$$

which is the ratio between the standard reconstructed energy  $E_{\text{std}}$  and the true beam energy  $E_{\text{beam}}$ . These measures greatly enhance the results and avoid overfitting of the training

energy boundaries.

### 10.1.2 Fully Connected Architecture

The neural network is implemented in python using the *keras* [139] and *tensorflow* [140] packages <sup>1</sup>. As a baseline model, two fully connected hidden layers with 128 and 64 neurons are chosen. The output layer has one neuron representing the prediction of the network. The activation function for the hidden layers is the often used *ReLU* function ( $\text{ReLU}(x) = \max(0, x)$ ). The output layer has a linear activation function. In order to prevent the network from overfitting, a dropout layer with a drop rate of 50 % is included in between the hidden layers. The optimization algorithm *Adam* [141] is used for training the network. As a loss function, the mean squared error MSE is used:

$$\text{MSE} = \frac{\sum_i (\Delta E_{\text{predicted},i} - \Delta E_{\text{true},i})^2}{N}, \quad (10.4)$$

with  $\Delta E_{\text{predicted}}$  and  $\Delta E_{\text{true}}$  being the predicted and the true correction factors. The sum is running over the whole training set with  $N$  samples. Depending on the number of input variables, the architecture above leads to a network with a complexity of about 3000 to 10000 parameters. About 200000 data samples are used for training the network.

## 10.2 Global Variables

In a first step the network is trained using global event variables and the results are compared to the global SC approach. As a baseline, fig. 10.1 (*left*) shows results where the set of input parameters consists only of the standard reconstructed energy. This means that the network has no additional information over the standard reconstruction. Over an energy range from 20 to 60 GeV, the standard reconstruction resolution is recovered. However, at the edges the reconstructed energy gets highly non-linear which leads to an artificial enhancement of the energy resolution as described in section 10.1. The skewed energy distributions for the high and low energies can be seen in fig. 10.1 (*right*).

By removing  $E_{\text{std}}$  from the set of input features and adding the two best performing observables for the global SC approach,  $\frac{C_{\text{thr}}}{C_{\text{av}}}$  and  $T_{\text{edep}}^{3\text{ns}}$ , this problem does not occur any more (see fig. 10.2 *left*). Surprisingly, the results are nearly identical to the global SC approach. Despite the fact that the neural network has a much higher complexity it is not able to outperform the relatively simple global SC method with the information at hand.

In order to see whether we can enhance the energy reconstruction by further adding input features, the following features are used:

<sup>1</sup>keras v2.2.3, tensorflow v1.5.1, python v3.5

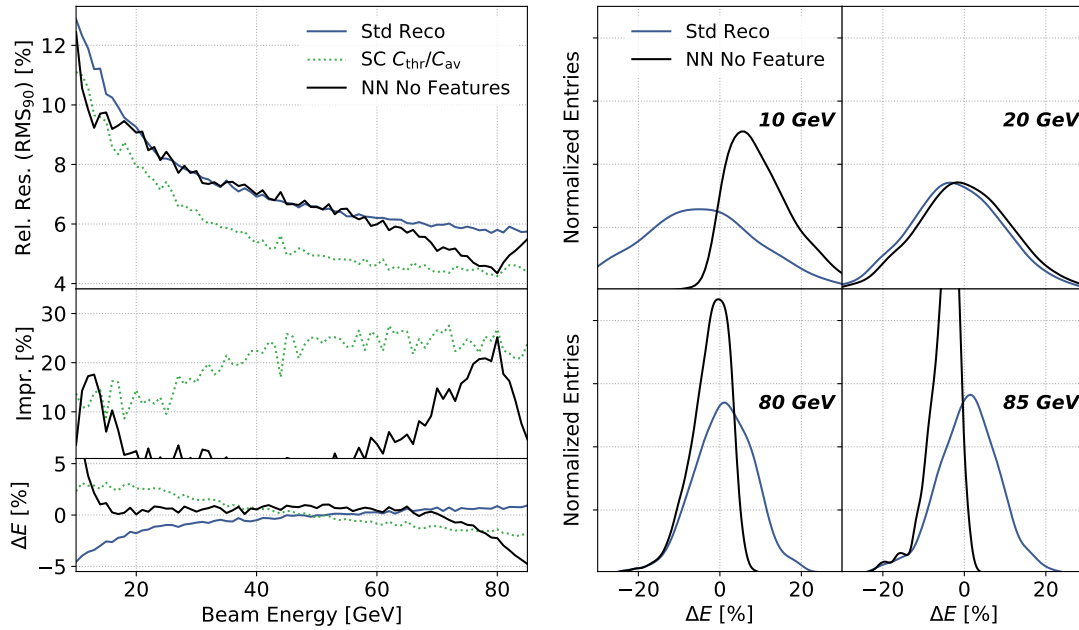


**Figure 10.1** – *Left*: Energy resolution for a fully connected neural network architecture. The only input variable is the standard reconstructed energy. *Right*: Energy distribution after NN reconstruction showing skewed distributions for low and high energies.

- The variable used in the hit energy dependent global software compensation approach  $\frac{C_{thr}}{C_{av}}$  (see section 8.1)
- The fraction of hits with more than 100 MIP  $C_{thr}^{100MIP}$ , selecting the very high energy depositions
- The time observables  $T_{edep}^{3ns}$ ,  $T_{edep}^{50ns}$  and  $T_{edep}^{N.el.}$  defined in section 8.2.2
- The mean shower radius  $R_{shower}$
- The center of gravity of the shower normalized to the shower start CoG<sub>z</sub>

The results are shown in fig. 10.2 (*right*). Indeed, a small improvement of a few percent of the energy resolution can be seen for low energies  $< 40$  GeV and for high energies  $> 60$  GeV. For the energies in between, no improvement, over the global SC approach is observed. Again, this results highlights the exceptionally good performance of the global SC approach.

### 10.3 Shower Profiles

In a next step, the number of input features is further increased. The idea is to include the whole shower profile and investigate if a neural network based analysis can improve the energy resolution by using the shower shape information. For this purpose, the energy per layer and the number of hits per layer are used. Both variables are normalized, i.e. they are

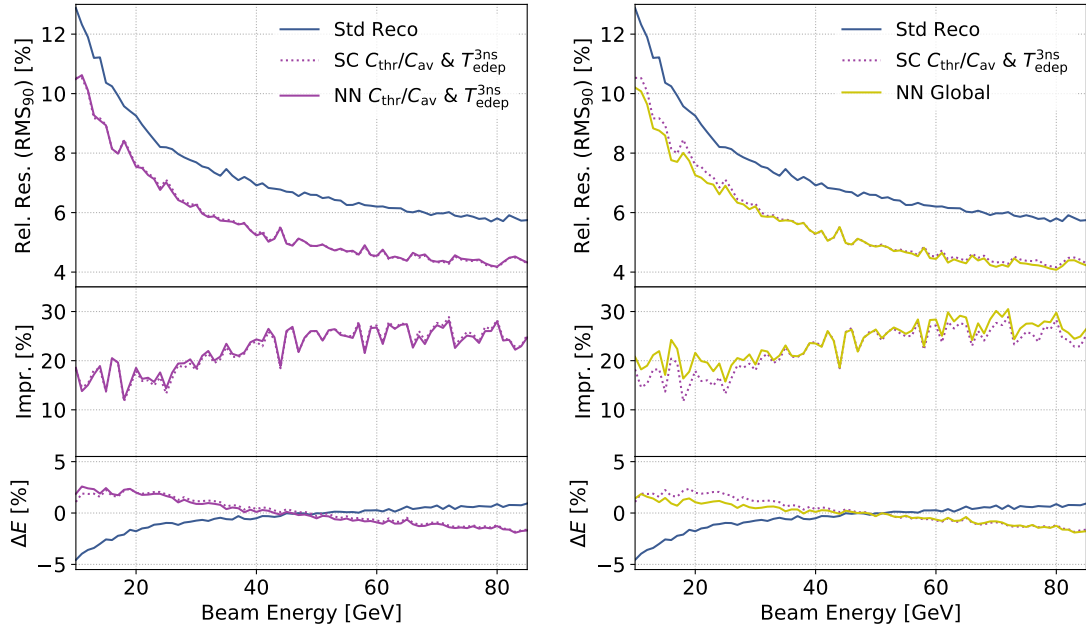


**Figure 10.2** – Energy resolution for a fully connected neural network architecture (black). *Left:* Using the same input variables as the best SC approach ( $C_{\text{thr}}/C_{\text{av}}$  and  $T_{\text{edep}}^{3\text{ns}}$ ). *Right:* Using more global observables as described in the text.

considered relative to the total energy sum and the total number of hits, respectively. This helps to keep the linearity of the reconstructed energy and suppresses the overfitting of the network at the boundaries of the training energies. Additionally, only the information of the first 45 layers after shower start is used to avoid correcting longitudinal leakage. Thus, the information of the last 5 to 15 layers, depending on the shower start, are not used. Figure 10.3 (*left*) shows the results for using only the energy shower shape information and using both the energy per layer and the number of hits per layer. Using only the energy shower shape, an average improvement of about 8% is achieved. Including the number of hits per layer, this improvement nearly doubles up to about 15% on average. The improvement is constant over the whole energy range in contrast to the SC and NN methods above, which show mostly much lower improvements for low energies. Using the NN with the energy and number of hits shower shape information yields similar improvements of up to 25 GeV compared to the best possible SC result.

The results for combining the shower shape information with the global observables described in the previous section are shown in fig. 10.3 (*right*). The energy resolution improves over the full energy range compared to the SC results, reaching improvements above 30% over the standard reconstruction for energies above 60 GeV. At the same time an excellent linearity of the reconstructed energy is achieved. These results show that the shower shape holds additional information which is not included in the selected global observables and can be used to enhance the energy reconstruction. A large improvement over the SC results

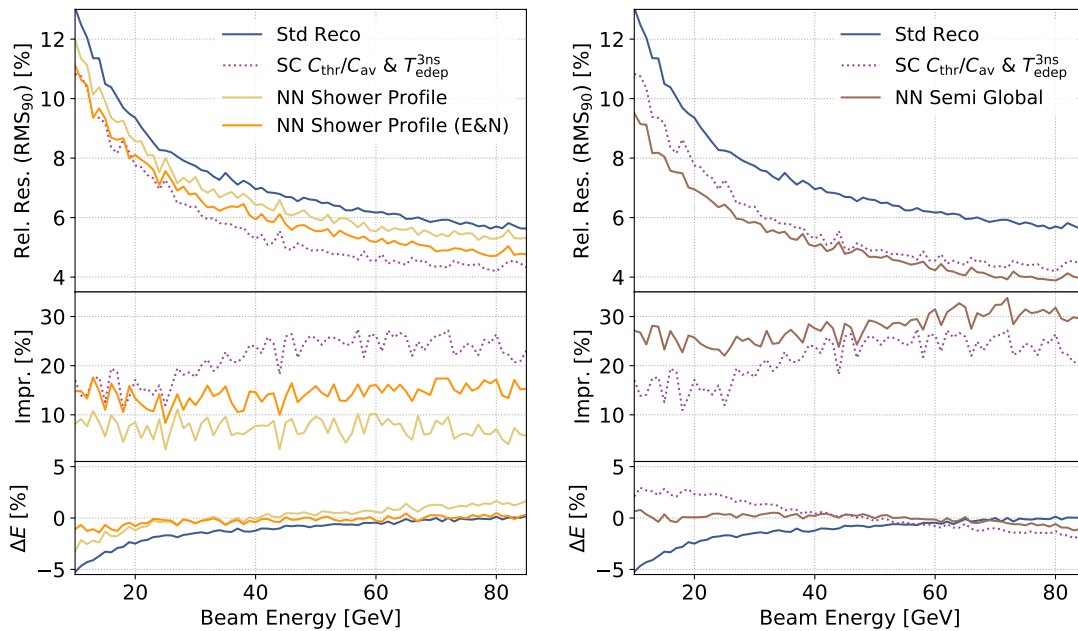


**Figure 10.3** – Energy resolution for a fully connected neural network architecture. *Left*: Using energy and number of hits information for each layer. *Right*: Adding global observables to the input variables.

are achieved, especially for lower energies. In the following, this neural network setup using the shower shape and the global observables will be referred to as the *semi-global* setup.

### 10.3.1 Stability

It is important to understand the robustness and stability of machine learning algorithms. For this purpose the splitting of the training and testing data sets is varied in this section. The fully connected neural network approach using the shower shape and global parameters (semi-global) is the most complex setup used and thus will be serving as a baseline model. Figure 10.4 (*left*) shows results for this setup with training done on all even energies (10, 12 GeV, ...) and the testing data set consisting of all odd energies (11, 13 GeV, ...). The neural network has to predict energies for which it has never seen an example of. At the same time this increases the binning of the training energies from 1 to 2 GeV steps. It can be seen that up to 60 GeV the results are similar to the results with the standard training set. For energies above 60 GeV, the resolution decreases slightly. Further, the linearity is worse than for the baseline case. In general inferring energies that the network was not trained on seems to be feasible. The slight deterioration of the energy resolution for the higher energies is probably due to the worse linearity.

As a second experiment the training data is restricted to a certain energy range and the behavior for the energies it was not trained on is examined. Three energy ranges are tested: 25 to 70 GeV (middle interval), 0 to 50 GeV (low interval) and 45 to 85 GeV (high interval). The

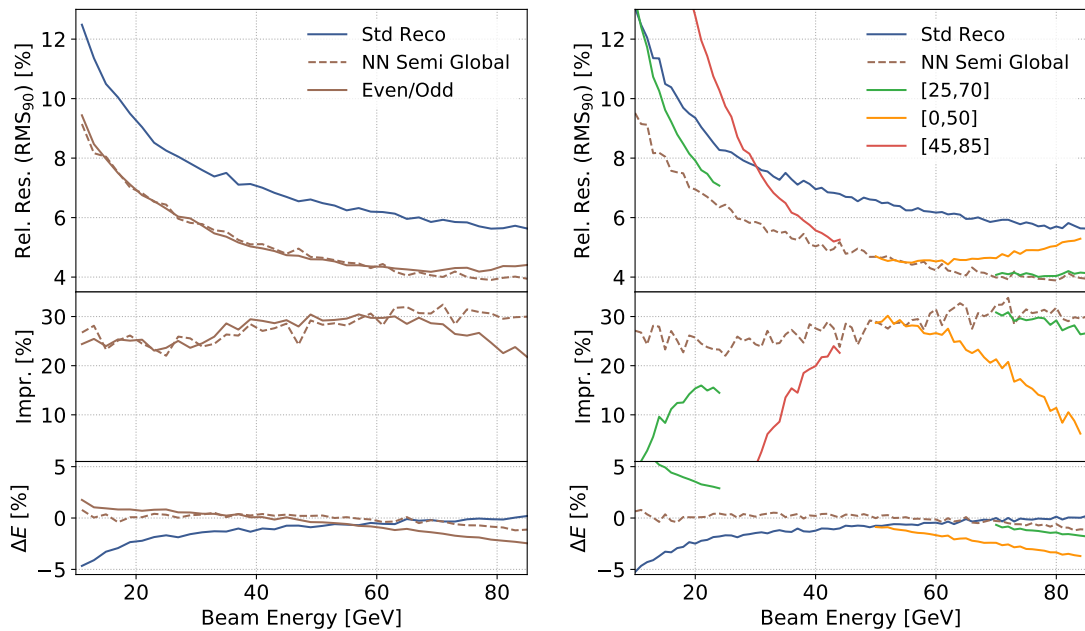


**Figure 10.4** – Energy resolution for fully connected neural network architecture. *Left:* Training on odd energies, predicting on even energies. *Right:* Training on several subsets of the whole energy range. See text for details.

results are shown in fig. 10.4 (*right*). For training on the middle interval from 25 to 70 GeV (green line) the predictions for the high energies from 71 to 85 GeV show very good results close to the benchmark NN case. For the low energies 10 to 24 GeV, however, the energy resolution decreases significantly. An improvement over the standard reconstruction is still visible. When training on low energies (0 to 50 GeV, orange line), reasonable predictions are observed up to 60 GeV. For higher energies, the resolution declines, but is still below the one for the standard reconstruction. This result is remarkable, since the network was trained only on showers up to 50 GeV. For the opposite case – training on high energies, evaluating on low energies – this is not the case (red line in fig. 10.4). Here, the energy resolution declines quickly and crosses the standard reconstruction resolution already at 30 GeV. Concluding, it is observed that the network can more easily extend to higher energies than to lower energies, when trained only on a subset of the energy range. This is in line with the fact that low energetic showers are usually very different from high energetic ones, as many shower observables scale with the logarithm of the energy.

## 10.4 Test Beam Geometry with 38 Layers

The aim of the studies above is to investigate machine learning algorithms for enhancing the energy reconstruction of the detector, while focussing on physics processes in hadronic showers. For this, effects by leakage were reduced as much as possible by increasing the

depth of the calorimeter. In this section we want to compare the simulation results with test beam data for which the simulation geometry has to be adapted to the test beam geometry.

#### 10.4.1 Simulation with 38 Layers

In order to use the neural network to correct the energy resolution of test beam data, the geometry of the detector in the simulation is changed back to the test beam geometry of 38 active layers. The event selection is kept similar: the required shower start is in the first ten layers and the cut on the energy distribution is increased requiring  $|E_{\text{std}} - E_{\text{beam}}| \leq 4\sqrt{E_{\text{beam}}}$ . This cut rejects about 5 % of the data sample after the shower start cut. Its main purpose is to reject outlier showers that have lots of leakage and thus are looking very different from a typical shower. The global training features are kept the same and all layers are considered for the shower profiles.

Results are shown in fig. 10.5 (*left*). The energy resolution of the standard reconstruction is significantly worse compared to the 60 layers scenario. Especially for energies above 30 GeV, the resolution stays constant instead of improving with the typical  $\sqrt{E}$  behavior. This shows that already for 30 GeV leakage is dominating the resolution. The global SC approach yields reasonable improvements over the standard reconstruction up to about 40 GeV. For higher energies the SC results get significantly worse. It is not a suitable method for correcting leakage. The NN results using the semi-global network show much better improvements for the high energies of up to 40 % improvement over the standard reconstruction. For lower energies more than 20 % improvement over the standard reconstruction are achieved. The linearity is worse than for the results with the 60 layer setup, which is most likely a result of the leakage. The deviations from the optimal linearity are approximately linear and can thus be corrected for by a simple linear fit optimizing parameters  $a$  and  $b$ , and correct the reconstructed energy  $E_{\text{NN}}$  by:

$$E_{\text{NN, corr}} = a + b \cdot E_{\text{NN}}. \quad (10.5)$$

This procedure gives a slight improvement in the energy resolution and enhances the linearity.

#### 10.4.2 Testing on Test Beam Data

The weights of the neural network trained on simulated data are now applied to test beam data. The results are shown in fig. 10.5 (*right*). In general, the resolution of the standard reconstruction is comparable to the simulation results. The characteristic flat distribution for energies above 30 GeV is seen as well. The 10 GeV point is significantly higher than the simulation results, which is probably due to the missing particle identification in the event selection. For the lower energies more electron contamination is expected at the CERN SPS beam lines.

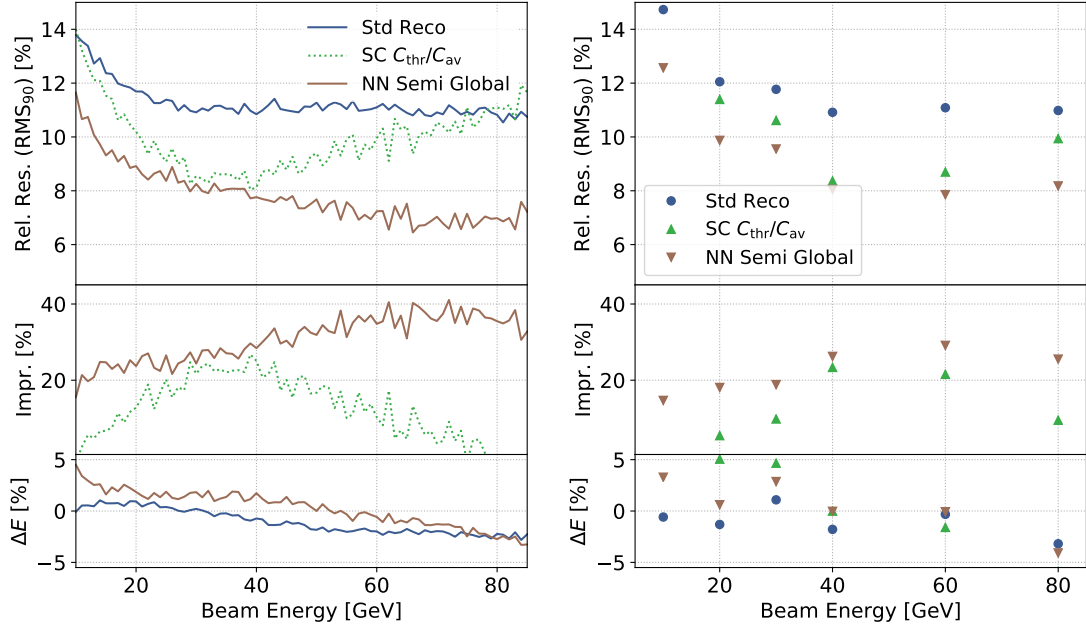


**Figure 10.5** – Energy resolution for fully connected neural network architecture. (*left*) Simulation results with 38 layers test beam geometry using the semi-global NN setup. (*right*) Applying the NN weights trained on simulation to test beam data. The SC results for comparison are optimized on test beam data.

The shown SC results in fig. 10.5 using the observable  $\frac{C_{thr}}{C_{av}}$  are obtained with weight factors derived by training on test beam data. For the lower energies up to 30 GeV only small improvements over the standard reconstruction are visible. For the middle energies of 40 and 60 GeV, about 20 % improvement are observed, while for the 80 GeV data point the improvement drops. The performance of the SC approach is comparable to the observations of the simulated data.

The application of the semi-global NN model with weights trained on simulation leads to results close to what is observed for testing on simulations. Here, improvements of up to 30 % over the standard reconstruction are achieved. About 18 % improvement for the lowest data point at 10 GeV is observed. The general features of the resolution curve apply also to the test beam data results: Higher energies have larger improvements. The distributions of the reconstructed energy for 10, 30, 60 and 80 GeV are shown in Figure 10.6 for the semi-global NN model applied to simulations (*left*) and to test beam data (*right*).

## 10.5 Cross Check: Electrons

Electromagnetic showers show a much better energy resolution than hadronic showers. They do not suffer from fluctuations in the invisible energy. Additionally, also the sampling fluctuations are expected to be lower in electromagnetic showers because of the higher compactness

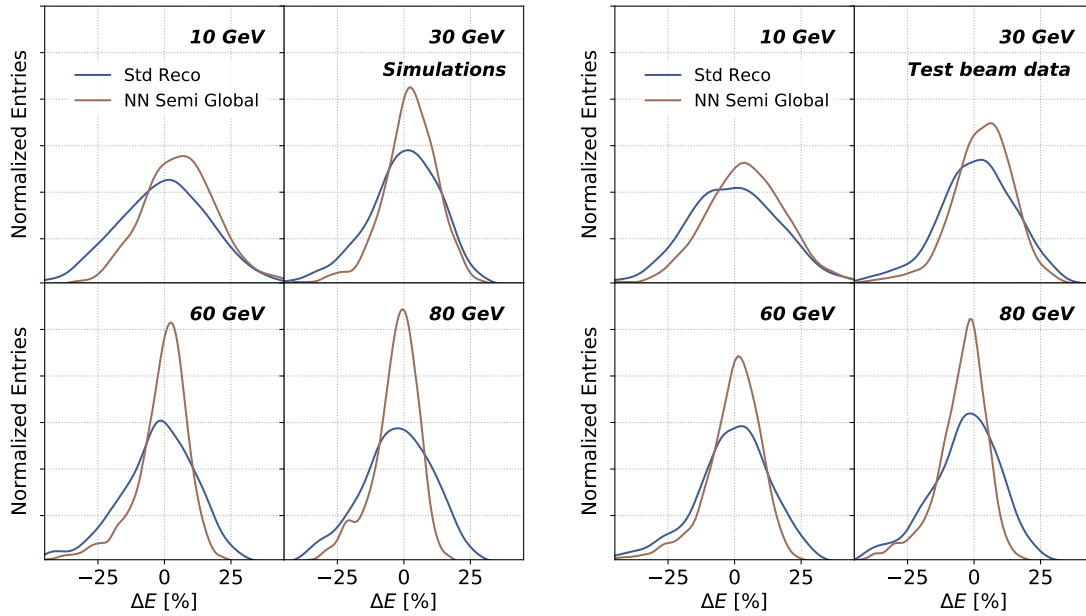


**Figure 10.6** – Energy distributions for simulations (*left*) and test beam data (*right*) with standard reconstruction and the semi-global reconstruction using the same NN model trained on simulations.

of the shower. As a cross check the fully connected neural network architecture is trained and tested on simulated electrons in the range from 10 to 100 GeV. Because the electromagnetic showers do not penetrate the detector as deep as the hadronic ones, the detector geometry with 38 layers is used. Figure 10.7 shows the results where the energy per layer and the number of hits per layer are used as input variables for training. As expected, no significant improvement is observed for the electromagnetic showers. The small improvement in energy resolution for low energies below 30 GeV can be explained entirely by the improved linearity.

## 10.6 Conclusions

In this chapter a novel approach for energy reconstruction of the AHCAL data based on a fully connected NN was developed. For global observables like hit energy and hit time dependent variables and several variables describing the shower geometry, only small improvements could be achieved over the SC approach. This result is compatible with the findings in [126], where a similar performance of global and local SC approaches were reported compared to a neural network model using five global input features. The fact that the addition of neither hit time observables nor shower geometry observables lead to a significant improvement in energy resolution (compared to the global SC approach), underlines the strong predictive power that can be extracted from hit energy observables.

It was shown that with the presented NN approach, the longitudinal shower profiles can be used to enhance the energy resolution compared to the standard reconstruction. This

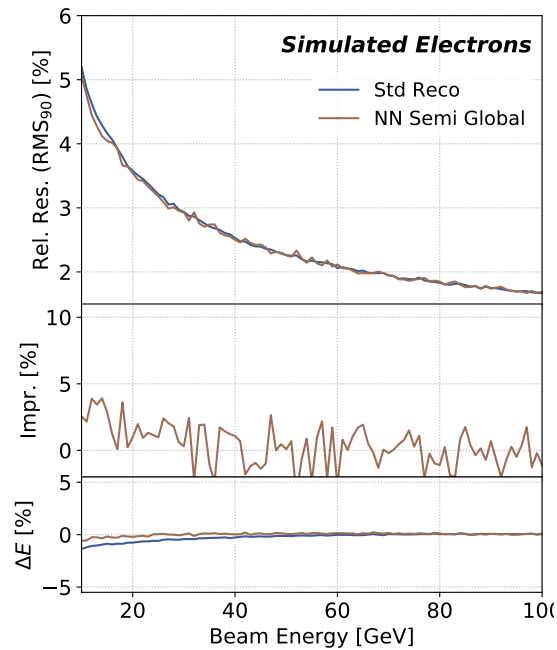


**Figure 10.7** – Energy Resolution for simulated electrons reconstructed with the fully connected neural network architecture.

shows that the longitudinal shape of a hadronic shower in a highly granular calorimeter can be used by machine learning algorithms to extract information about the processes happening in the shower. The combined use of the numbers of hits per layer as well as the energy sum per layer turned out to be beneficial for the energy reconstruction. Further adding the global observables to the list of input features leads to a significant improvement of the energy resolution compared to the global SC approach for the simulation setup with 60 layers.

For a simulation setup with 38 layers, leakage plays a larger role. For the semi-global NN model, improvements in energy resolution of up to 40 % for 70 GeV pions were observed. The same semi-global model with weights trained on simulations was applied to test beam data, leading to improvements of up to 30 % for the test beam data over the standard reconstruction.

## **Part IV**

# **Concluding Remarks**



# Conclusions

The overall goal of this thesis was to investigate to what extent the hit time information of the AHCAL technological prototypes can be used to enhance its energy resolution. To evaluate this, two main analyses were performed: A time analysis of test beam data taken with the partially equipped technological prototype (PTP) in a tungsten absorber, and an analysis of novel methods for energy reconstruction within the AHCAL.

## Time Analysis

For precision time measurements, the digital information provided by the readout ASICs need to be calibrated and converted to ns. In prior studies this was done manually by laboratory measurements [80, 101]. For the calibration of a whole detector, a manual measurement of all readout ASICs is not desirable and a calibration procedure using test beam data is foreseen. This was first demonstrated in an analysis of the PTP with a steel absorber stack [50]. This thesis presents the first analysis of a dataset taken with the PTP in a tungsten absorber stack. For this, a time calibration scheme was developed including a novel method for extracting the time pedestal and time slope calibration constants of the calorimeter cells. It was shown in a toy Monte Carlo (MC) simulation that a sufficient precision of the calibration can be achieved using 30 muon hits in each calorimeter cell. For muon beam, a time resolution of 6.3 ns was achieved. For electromagnetic showers a time resolution of 10.2 ns was measured. The time resolution gets broadened for electromagnetic showers because of an electronics effect leading to an increased time jitter for high chip occupancies. Similar results were also observed in [50]. The integration of the hit time calibration and reconstruction procedure within the CALICE analysis workflow sets the basis for future, high precision time analyses.

Compared to muons and electromagnetic showers, which give a quasi-instantaneous hit time response with respect to the time resolution, hadronic showers are expected to show a more complex time development. Neutrons with energies of a few MeV originating from spallation processes can travel long distances in the calorimeter before interacting with the active absorber material, leading to calorimeter signals late in the shower development. This time structure has important consequences for the performance of a calorimeter. Energy depositions later than the maximum integration time of the readout are lost and the large event-by-event fluctuations lead to a worsening of the detector performance. Furthermore,

the time development correlates with the lateral size of the showers and may be important with respect to timing cuts motivated by pile-up and background suppression. Therefore, it is crucial to measure the time development and correctly model it in simulations. The time structure of hadronic showers was for example measured with the uranium-scintillator barrel calorimeter of the ZEUS detector [142]. In the context of a CALICE prototype, the time development of hadronic showers was first measured with the T3B experiment [16], which was build of a row of scintillator tiles located at the back of CALICE prototypes with steel and tungsten absorbers. It was shown already by the T3B experiment that the late component of the hadronic showers are larger in tungsten than in a steel absorber because of the higher atomic number.

This thesis provides an analysis of the time development of hadronic showers in a tungsten absorber with the PTP. A component of late hit deposits (later than 75 ns after the trigger signal) is clearly visible. At 300 ns after the trigger signal on average about 1 hit/100ns is observed for 70 GeV pions. The average fraction of late hits is 7 %, which is found to be constant across all beam energies. The late energy depositions are predominantly located at the outer part of the shower and the average fraction of late hits is larger for deeper layers of the calorimeter. Furthermore, the late energy depositions were found to have mostly low energy ( $< 5$  MIP). These observations are consistent with the interpretation of late energy depositions due to neutron capture events. Set side by side to the hit time analysis of hadronic showers in the PTP with a steel absorber [50], about eight times more late hits are observed in the tungsten absorber.

The findings in test beam data were compared to simulated data using several physics lists. The physics lists could broadly be separated into two groups. Those employing the bertini cascade model or the high precision neutron tracking package are overestimating the late energy depositions by about a factor of two. Physics lists using the binary cascade model are underestimating the late contributions by about the same factor. For the T3B experiment, good agreement was observed between data and simulations using the high precision neutron tracking package, while for a physics list using the bertini cascade model large discrepancies were reported. The different findings can be explained by different versions of the simulation framework (T3B: Geant4 v9.4, this analysis: Geant4 v10.1), where substantial changes in the implementation of the time development were implemented [76]. Because of the special geometry of the T3B experiment, these measurements are likely dominated by deeper and more central parts of the shower compared to the results in the present analysis.

## Energy Reconstruction

After the insights gained into the hit time measurements of the AHCAL, the second analysis part of the thesis studied the energy reconstruction of the large technological prototype (LTP) with a steel absorber on simulated data and how the hit time measurements can be used to improve the energy resolution. Because the LTP is a non-compensating calorimeter prototype, the energy resolution of hadronic showers is governed by large fluctuations depending on the nuclear binding energy lost in an event due to spallation processes and the subsequent release of nucleons from the absorber nuclei. These fluctuations are highly correlated with the electromagnetic fraction of a hadronic shower. The reconstructed energy can be corrected on an event-by-event basis by software compensation methods exploiting the differences in energy density between the electromagnetic and the hadronic sub-showers [11]. It was demonstrated already with a dual readout calorimeter that the neutron content of a hadronic shower (anti-)correlates with its electromagnetic fraction [45]. The measurement of the time structure of a given shower could thus be used to further increase the energy resolution of a highly granular calorimeter.

In a first step, global observables were constructed with thresholds on the hit time distribution to select the energy depositions expected to arise from neutron elastic scattering ( $3 \text{ ns} < t_{\text{hit}} < 50 \text{ ns}$ ) and from neutron capture events ( $t_{\text{hit}} > 50 \text{ ns}$ ). For a given beam energy, a significant correlation of these observables with the reconstructed energy were observed, implying that these observables may be used to enhance the energy resolution over the standard energy reconstruction. First, this was shown on simulated data, where the limited integration time of the data acquisition system is ignored. It was shown that limiting the integration time to 2000 ns leads to a decrease in energy resolution of 14 %. On average, 4 % of the energy depositions are happening at hit times later than 2000 ns and the large event-to-event fluctuations of this number are leading to the decrease in energy resolution. These findings highlight the important role of neutron based energy depositions in the AHCAL.

Large correlations between the energy depositions in the neutron scattering time regime and the energy depositions later than 2000 ns were found. These correlations were exploited to correct for the non-measured, late energy depositions. A linear correction factor was introduced based on the estimate of the neutron scattering activity in a given event. This method artificially enhances the response of the calorimeter to the neutron scattering processes. Up to 70 % of the initial energy resolution performance could be recovered with this method.

Even larger improvements could be achieved by an approach similar to the global SC method. In this method the event energy is corrected by a second order polynomial function of the energy depositions later than 3 ns. The weights of this function are determined in a training process by minimizing the difference between the corrected and the true energy. With this method improvements of up to 18 % were achieved over the standard reconstruction. Hence, this result shows that significant improvements in the energy reconstruction can be achieved by exploiting the hit time measurements in a high granular calorimeter. However,

using the same method with observables derived from the hit energy spectrum (similar to the traditional global SC approach) leads to even larger improvements in energy resolution up to 25 %. It could be shown that the combination of both hit energy and hit time observables only leads to small improvements over using only the hit energy observables.

The feasibility of a neural network approach for energy reconstruction in a highly granular calorimeter was already shown in a study using data of the AHCAL physics calorimeter prototype [126]. In this thesis, a machine learning setup for energy reconstruction in the AHCAL was developed based on a modern neural network architecture. The used architecture is more complex compared to [126] and allows for a large number of input features. With this approach it was shown that the energy resolution can be improved taking the longitudinal shower profile of the showers as input features. Using the energy and number of hits per layer, improvements in the energy resolution over the standard reconstruction of 15 % could be achieved. Together with other global input features, up to 30 % improvement were achieved, significantly more compared to the global SC approach. It could be shown that the neural network model trained on simulated data can be applied to test beam data leading to improvements of up to 30 % over the standard reconstruction.

The main goal of this thesis was formulated to study whether the hit time capabilities of the AHCAL can be used in the energy reconstruction process to enhance the energy resolution. With the methods developed in this thesis it was shown on simulated data that observables constructed from the hit time measurements can be used for significant improvements in the energy resolution compared to the standard reconstruction. At the same time it was also shown that this approach does not outperform software compensation methods that are exploiting the hit energy spectrum of hadronic showers. However, it was demonstrated that machine learning algorithms offer the possibility for improvements in energy resolution in highly granular calorimeters using the shower shape information.

# Outlook

The work done in this thesis may be the starting point of further studies. In the following an outlook on possible directions for additional studies is presented.

The new test beam data taken with the large technological prototype (LTP) in 2018 opens the opportunity for time analyses with a fully equipped CALICE prototype. The LTP consists of 38 layers with only a very small number of dead channels. Amongst others an advantage over the partially equipped technological prototype (PTP) is the possibility to reconstruct a shower start for hadronic interactions, allowing to study the longitudinal time development of hadronic showers with higher precision. The precision of the time measurement is expected to increase compared to the results presented in this thesis. This is mainly due to a better time reference, a new version of the readout ASIC and an improved hit time reconstruction. The improved time resolution could allow not only to investigate the neutron capture time regime, but also the time regime before 50 ns after the reference time. Besides the data already taken with the LTP in a steel absorber, test beam campaigns of the LTP in a tungsten absorber stack are also foreseen. With the ongoing progress of the hit time reconstruction of the LTP data it is of interest to verify that the time assisted energy reconstruction presented in this thesis can be transferred to test beam data.

For the energy reconstruction studies in this thesis, a time resolution of 1 ns was assumed. Many experiment proposals are currently aiming at high precision timing capabilities. For example the CMS HGCALE endcap calorimeter proposes a time resolution of at least 50 ps [143] for electromagnetic showers. The sub nanosecond time resolution could open up a new window for time assisted energy reconstruction. A shower particle traveling at the speed of light takes about 200 ps to travel through one layer of the AHCAL. Very high precision timing could thus give more precise information on the origin of certain energy depositions within a shower, also for relativistic particles.

The machine learning setup developed in this thesis can easily be used to incorporate more complex global observables into the energy reconstruction process. Examples could be the number and length of sub-tracks within the shower, or the number of hard, secondary, inelastic interactions. Additionally, it could be thought of more semi-global observables used in the neural network approach, for example the average hit radius in each layer.

Ultimately, the use of 5-dimensional ( $x$ -,  $y$ -,  $z$ -position, hit energy, hit time), cell-wise

input data into a machine learning setup could make the manual feature construction obsolete. Handling this high dimensional input data is challenging but could be solved with more complex neural network architectures relying on convolutional neural networks with several hidden layers (deep neural networks). A first study for such an analysis was already presented in [144]. It remains an open question if the hit time measurements on cell level lead to an improvement in the energy resolution in such a deep learning approach.

Highly granular calorimeters are by now well established in the high energy particle physics community. Technologies developed within the CALICE collaboration are spreading to other experiments as for example the CMS HGCal [17]. Even though different experiments are facing different challenges, the conclusions drawn in this thesis may find applications outside of  $e^+e^-$ -collider experiments further advancing the field of particle physics.

## **Appendix A**

# **Supplementary Tables and Figures**

## A.1 Time Analysis: PTP Setup

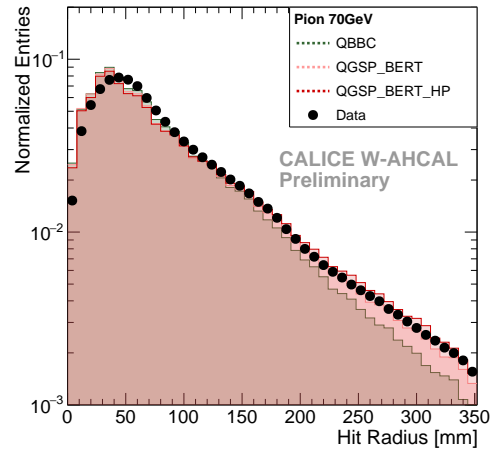
**Table A.1** – Physical ordering of layers in the AHCAL tungsten technological prototype for the August 2015 testbeam campaign. Additionally, the SiPM and tile configuration is given.

Phys. Order	Abs. Layer	Type	SiPM	Scintillator
1	0	1 × EBU	Hamamatsu 10000 px	strips
2	1	1 × EBU	Hamamatsu 10000 px	strips
3	2	1 × EBU	Hamamatsu 1600 px	strips
4	3	1 × HBU	Hamamatsu 1600 px	tiles w/ surf. mount SiPMs
5	4	1 × HBU	Ketek 12000 px	tiles w/o WLS fibres
6	5	1 × HBU	Ketek 12000 px	tiles w/o WLS fibres
7	6	1 × HBU	CPTA 800 px	tiles w/ WLS fibres
8	7	1 × HBU	CPTA 800 px	tiles w/ WLS fibres
9	8	1 × HBU	CPTA 800 px	tiles w/ WLS fibres
10	9	1 × HBU	CPTA 800 px	tiles w/ WLS fibres
11	10	1 × HBU	CPTA 800 px	tiles w/ WLS fibres
12	11	4 × HBU	Ketek 2300 px	tiles w/o WLS fibres
13	13	4 × HBU	Ketek 2300 px	tiles w/o WLS fibres
14	21	4 × HBU	SenSL 1300 px	tiles w/o WLS fibres
15	31	4 × HBU	SenSL 1300 px	tiles w/o WLS fibres

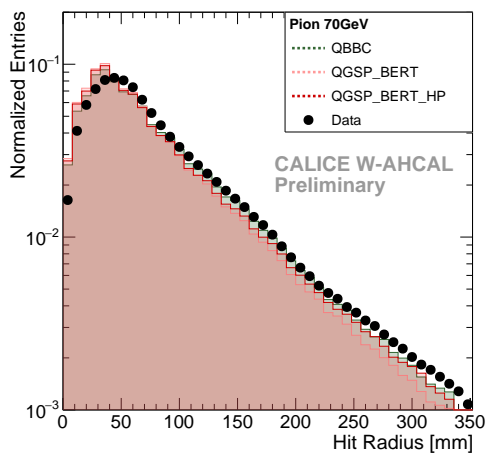
**Table A.2** – Status of  $T_0$ -channels: Out of the initial six validation channels, two are still working properly.

Layer	Chip	Channel	Status
12	169	29	noisy
12	177	23	broken
13	185	29	broken TDC
14	201	29	OK
14	211	6	broken
15	217	23	OK

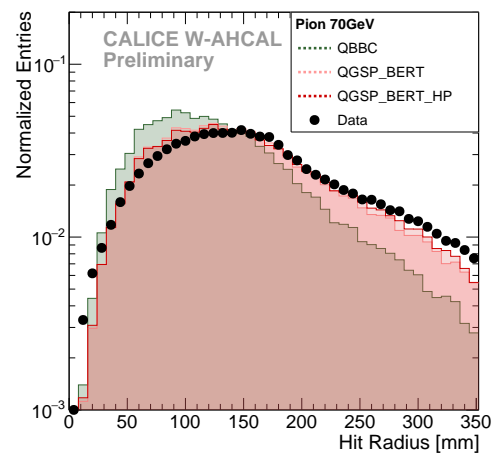
## A.2 Time Analysis: Lateral Shower Shape



(a) Hit radius distribution



(b) Hit radius distribution for early hits  $\leq 75$  ns



(c) Hit radius distribution for late hits  $> 75$  ns

**Figure A.1** – Hit radius distribution of data compared to MC simulation using different physics lists (a). The data is split up in early hits  $\leq 75$  ns (b) and late hit  $> 75$  ns (c).

### A.3 Energy Reconstruction: SC with Additional Variables

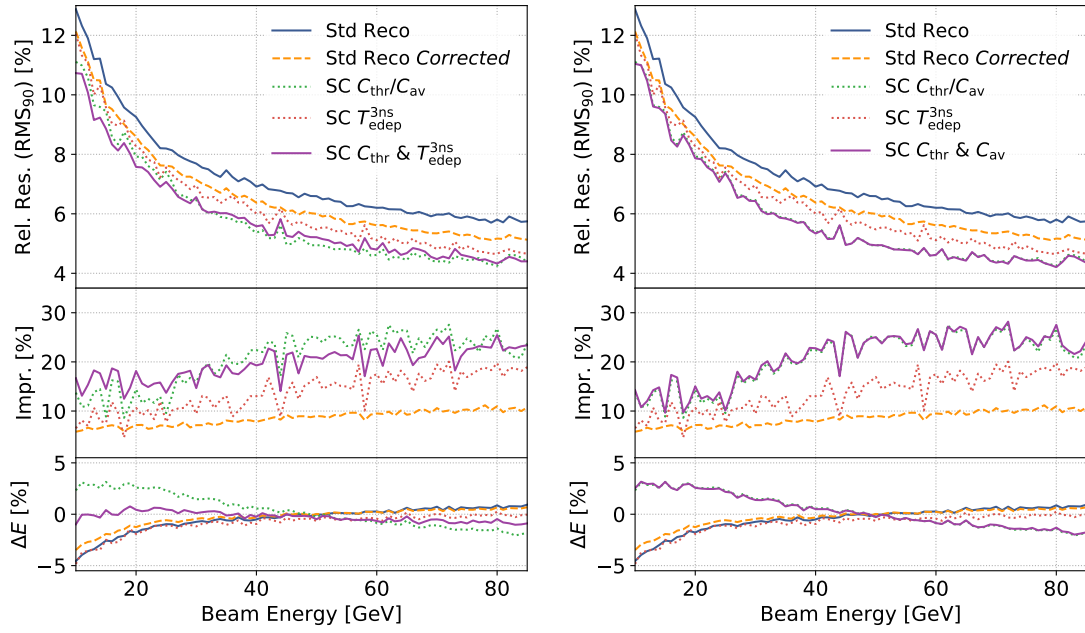


**Figure A.2** – Energy resolution, improvement and linearity shown for the SC approach using  $T_{\text{edep}}^{3\text{ns}}$  (left) and  $C_{\text{thr}}/C_{\text{av}}$  and  $T_{\text{edep}}^{3\text{ns}}$  (right). Shown are the standard reconstruction, the time correction described in section 8.4, the SC results as well as results for applying the time correction before SC.

# Bibliography

- [1] G Arnison, A Astbury, B Aubert, et al. Experimental observation of lepton pairs of invariant mass around  $95 \text{ GeV}/c^2$  at the CERN SPS collider. *Physics Letters B*, 126(5):398–410, 1983.
- [2] Po Bagnaia, B Madsen, JC Chollet, et al. Evidence for  $z^0 \rightarrow e^+ e^-$  at the CERN  $\bar{p}p$  collider. *Physics Letters B*, 129(CERN-EP-83-112):130–140, 1983.
- [3] F Abe, H Akimoto, A Akopian, et al. Observation of top quark production in pp collisions with the Collider Detector at Fermilab. *Physical Review Letters*, 74(14):2626, 1995.
- [4] S Abachi, B Abbott, M Abolins, et al. Search for high mass top quark production in pp collisions at  $\sqrt{s} = 1.8 \text{ TeV}$ . *Physical Review Letters*, 74(13):2422, 1995.
- [5] ATLAS collaboration. Observation of a new particle in the search for the Standard Model Higgs boson with the ATLAS detector at the LHC. *Physics Letters B*, 716(1):1–29, 2012.
- [6] CMS collaboration. Observation of a new boson at a mass of 125 GeV with the CMS experiment at the LHC. *Physics Letters B*, 716(1):30–61, 2012.
- [7] Erika Garutti. Silicon photomultipliers for high energy physics detectors. *Journal of Instrumentation*, 6(10):C10003, 2011.
- [8] Ties Behnke, James E. Brau, Brian Foster, et al. The International Linear Collider technical design report - volume 1: Executive summary. 2013.
- [9] Philip N Burrows, N Catalan Lasheras, Lucie Linssen, et al. The Compact Linear Collider (CLIC)-2018 summary report. 2018.
- [10] FCC collaboration. FCC-ee: The lepton collider: Future Circular Collider conceptual design report volume 2. *European Physical Journal: Special Topics*, 228(2):261–623, 2019.
- [11] CALICE collaboration. Hadronic energy resolution of a highly granular scintillator-steel hadron calorimeter using software compensation techniques. *Journal of Instrumentation*, 7(09):P09017, 2012.

- 
- [12] CALICE collaboration. Study of the interactions of pions in the CALICE silicon-tungsten calorimeter prototype. *Journal of Instrumentation*, 5(05):P05007, 2010.
- [13] Felix Sefkow, Andy White, Kiyotomo Kawagoe, et al. Experimental tests of particle flow calorimetry. *Reviews of Modern Physics*, 88(1):015003, 2016.
- [14] Roman Pöschl and The CALICE Collaboration. Recent results of the technological prototypes of the CALICE highly granular calorimeters. *Nuclear Instruments and Methods in Physics Research Section A*, 2019.
- [15] Felix Sefkow and Frank Simon. A highly granular SiPM-on-tile calorimeter prototype. *Journal of Physics: Conference Series*, 1162(1):012012, 2019.
- [16] CALICE collaboration. The time structure of hadronic showers in highly granular calorimeters with tungsten and steel absorbers. *Journal of Instrumentation*, 9(07):P07022, 2014.
- [17] CMS collaboration. The phase-2 upgrade of the CMS endcap calorimeter. Technical Report CERN-LHCC-2017-023. CMS-TDR-019, CERN, Nov 2017.
- [18] François Englert and Robert Brout. Broken symmetry and the mass of gauge vector mesons. *Physical Review Letters*, 13(9):321, 1964.
- [19] Peter W Higgs. Broken symmetries and the masses of gauge bosons. *Physical Review Letters*, 13(16):508, 1964.
- [20] Gerald S Guralnik, Carl R Hagen, and Thomas WB Kibble. Global conservation laws and massless particles. *Physical Review Letters*, 13(20):585, 1964.
- [21] ATLAS collaboration. Standard model summary plots summer 2019. Technical Report ATL-PHYS-PUB-2019-024, CERN, Jul 2019.
- [22] J. Grange et al. Muon (g-2) technical design report. *Fermilab Technical Publications*, 2015.
- [23] T Abe, I Adachi, K Adamczyk, et al. Belle II technical design report. *arXiv preprint arXiv:1011.0352*, 2010.
- [24] Jacqueline Yan, Shun Watanuki, Keisuke Fujii, et al. Measurement of the Higgs boson mass and  $e^+ e^- \rightarrow Z H$  cross section using  $Z \rightarrow \mu^+ \mu^-$  and  $Z \rightarrow e^+ e^-$  at the ILC. *Physical Review D*, 94(11):113002, 2016.
- [25] Howard Baer, Tim Barklow, Keisuke Fujii, et al. The International Linear Collider technical design report-volume 2: physics. *arXiv preprint arXiv:1306.6352*, 2013.

- [26] H Abramowicz, N Alipour Tehrani, D Arominski, et al. Top-quark physics at the CLIC electron-positron linear collider. *Journal of High Energy Physics*, 2019(11):3, 2019.
- [27] ATLAS collaboration. Combination of searches for Higgs boson pairs in pp collisions at 13 TeV with the ATLAS experiment. ATLAS-CONF-2018-043, 2018.
- [28] CEPC Study Group. CEPC conceptual design report. *arXiv preprint arXiv:1809.00285*, 2018.
- [29] Claude Leroy and Pier-Giorgio Rancoita. *Principles of radiation interaction in matter and detection*. World Scientific, 2011.
- [30] Claus Grupen and Boris Schwartz. Particle detectors, 2008.
- [31] Richard Wigmans. *Calorimetry: Energy measurement in particle physics*, volume 107. Oxford University Press, 2000.
- [32] Stephen M Seltzer and Martin J Berger. Evaluation of the collision stopping power of elements and compounds for electrons and positrons. *The International Journal of Applied Radiation and Isotopes*, 33(11):1189–1218, 1982.
- [33] C Amsler et al. Review of particle physics, passage of particles through matter. *Physics Letters B*, 667:1, 2008.
- [34] Richard Wigmans. On the role of neutrons in hadron calorimetry. *Review of Scientific Instruments*, 69(11):3723–3736, 1998.
- [35] C Enss and D McCammon. Physical principles of low temperature detectors: ultimate performance limits and current detector capabilities. *Journal of Low Temperature Physics*, 151(1-2):5–24, 2008.
- [36] CMS collaboration. Energy calibration and resolution of the CMS electromagnetic calorimeter in pp collisions at  $\sqrt{s} = 7$  TeV. *arXiv preprint arXiv:1306.2016*, 2013.
- [37] John Betteley Birks. *The theory and practice of scintillation counting*. 1964.
- [38] Masaharu Tanabashi and others (Particle Data Group). Review of particle physics, particle detectors at accelerators. *Physical Review D*, 98(3):030001, 2018.
- [39] John Betteley Birks. Scintillations from organic crystals: specific fluorescence and relative response to different radiations. *Proceedings of the Physical Society. Section A*, 64(10):874, 1951.
- [40] Nils Feege. *Low-energetic hadron interactions in a highly granular calorimeter*. Ph.D. thesis, Hamburg U., 2011.

- [41] D Acosta, S Buontempo, L Caloba, et al. Lateral shower profiles in a lead/scintillating fiber calorimeter. *Nuclear Instruments and Methods in Physics Research Section A*, 316(2-3):184–201, 1992.
- [42] James E Brau and Tony A Gabriel. Theoretical studies of hadronic calorimetry for high luminosity, high energy colliders. *Nuclear Instruments and Methods in Physics Research Section A*, 279(1-2):40–56, 1989.
- [43] Erwin Hilger. The ZEUS uranium-scintillator calorimeter for HERA. *Nuclear Instruments and Methods in Physics Research Section A*, 257(3):488–498, 1987.
- [44] Jan Philipp Goecke. Simulation of the time structure of hadronic showers in a highly granular calorimeter with RPC readout. Master Thesis, TU München, 2016.
- [45] N Akchurin, M Alwarawrah, A Cardini, et al. Neutron signals for dual-readout calorimetry. *Nuclear Instruments and Methods in Physics Research Section A*, 598(2):422–431, 2009.
- [46] Adolf Bornheim, Artur Apresyan, Javier Duarte, et al. Calorimeters for precision timing measurements in high energy physics. In *Journal of Physics: Conference Series*, volume 587, page 012057. IOP Publishing, 2015.
- [47] Erica Brondolin and Andre Sailer. Optimization of timing selections at 380 GeV CLIC. *arXiv preprint arXiv:1811.00466*, 2018.
- [48] R DeSalvo, FG Hartjes, AM Henriques, et al. A novel way of electron identification in calorimeters. *Nuclear Instruments and Methods in Physics Research Section A*, 279(3):467–472, 1989.
- [49] D Acosta, S Buontempo, L Caloba, et al. Electron-pion discrimination with a scintillating fiber calorimeter. *Nuclear Instruments and Methods in Physics Research Section A*, 302(1):36–46, 1991.
- [50] Eldwan Brianne. *Time development of hadronic showers in a Highly Granular Analog Hadron Calorimeter*. Ph.D. thesis, DESY, 2018.
- [51] Sea Agostinelli, John Allison, K al Amako, et al. Geant4: A simulation toolkit. *Nuclear Instruments and Methods in Physics Research Section A*, 506(3):250–303, 2003.
- [52] Geant4 collaboration. Geant4 physics reference manual. <http://geant4-userdoc.web.cern.ch/geant4-userdoc/UsersGuides/PhysicsReferenceManual/html/hadronic/index.html>, 2019.
- [53] Aatos Heikkinen, Nikita Stepanov, and Johannes Peter Wellisch. Bertini intra-nuclear cascade implementation in Geant4. *arXiv preprint nucl-th/0306008*, 2003.

- [54] Gunter Folger and JP Wellisch. String parton models in Geant4. *arXiv preprint nucl-th/0306007*, 2003.
- [55] G Folger, VN Ivanchenko, and JP Wellisch. The binary cascade. *The European Physical Journal A-Hadrons and Nuclei*, 21(3):407–417, 2004.
- [56] Ties Behnke et al. The International Linear Collider technical design report-volume 4: detectors. Technical report, 2013.
- [57] Dominik Arominski, Jean-Jacques Blaising, Erica Brondolin, et al. A detector for CLIC: main parameters and performance. *arXiv preprint arXiv:1812.07337*, 2018.
- [58] Georges Aad, Tatevik Abajyan, Brad Abbott, et al. Jet energy resolution in proton-proton collisions at  $\sqrt{s} = 7$  TeV recorded in 2010 with the ATLAS detector. *The European Physical Journal C*, 73(3):2306, 2013.
- [59] CMS collaboration. Jet energy scale and resolution in the CMS experiment in pp collisions at 8 TeV. *arXiv preprint arXiv:1607.03663*, 2016.
- [60] JS Marshall, A Münnich, and MA Thomson. Performance of particle flow calorimetry at CLIC. *Nuclear Instruments and Methods in Physics Research Section A*, 700:153–162, 2013.
- [61] Matthew Wing. Precise measurement of jet energies with the ZEUS detector. *arXiv preprint hep-ex/0011046*, 2000.
- [62] ALEPH collaboration. Performance of the ALEPH detector at LEP. *Nuclear Instruments and Methods in Physics Research A*, 360:481–506, 1995.
- [63] Albert M Sirunyan and CMS collaboration. Particle-flow reconstruction and global event description with the CMS detector. *Journal of Instrumentation*, 12(10):P10003, 2017.
- [64] MA Thomson. Particle flow calorimetry and the PandoraPFA algorithm. *Nuclear Instruments and Methods in Physics Research Section A*, 611(1):25–40, 2009.
- [65] Burak Bilki, John Butler, Georgios Mavromanolakis, et al. Hadron showers in a digital hadron calorimeter. *Journal of Instrumentation*, 4(10):P10008, 2009.
- [66] G Baulieu, M Bedjidian, K Belkadhi, et al. Construction and commissioning of a technological prototype of a high-granularity semi-digital hadronic calorimeter. *Journal of Instrumentation*, 10(10):P10039, 2015.
- [67] Naoki Tsuji. Performance of alternative scintillator tile geometry for AHCAL. *arXiv preprint arXiv:1902.05266*, 2019.

- [68] Patrick Eckert, Hans-Christian Schultz-Coulon, Wei Shen, et al. Characterisation studies of silicon photomultipliers. *Nuclear Instruments and Methods in Physics Research Section A*, 620(2-3):217–226, 2010.
- [69] Patrick Eckert. Advanced silicon-photomultiplier characterization for calorimetric applications, 2010.
- [70] Gianmaria Collazuol, G Ambrosi, Maurizio Boscardin, et al. Single photon timing resolution and detection efficiency of the IRST silicon photo-multipliers. *Nuclear Instruments and Methods in Physics Research Section A*, 581(1-2):461–464, 2007.
- [71] CALICE collaboration. Construction and commissioning of the CALICE analog hadron calorimeter prototype. *Journal of Instrumentation*, 5(05):P05004, 2010.
- [72] CALICE collaboration. Pion and proton showers in the CALICE scintillator-steel AHCAL: comparison of global observables. *Journal of Instrumentation*, 10(arXiv:1412.2653.04):P04014. 25 p, Dec 2014.
- [73] CALICE collaboration. Hadron shower decomposition in the highly granular CALICE analogue hadron calorimeter. *Journal of Instrumentation*, 11(arXiv:1602.08578):P06013. 38 p, Feb 2016.
- [74] CALICE collaboration. Shower development of particles with momenta from 1 to 10 GeV in the CALICE Scintillator-Tungsten HCAL. *Journal of Instrumentation*, 9(arXiv:1311.3505.01):P01004. 28 p, Jun 2012.
- [75] CALICE collaboration. Shower development of particles with momenta from 15 GeV to 150 GeV in the CALICE scintillator-tungsten hadronic calorimeter. *Journal of Instrumentation*, 10(arXiv:1509.00617. AIDA-NOTE-2015-011):P12006. 35 p, Aug 2013.
- [76] J Allison, Katsuya Amako, J Apostolakis, et al. Recent developments in Geant4. *Nuclear Instruments and Methods in Physics Research Section A*, 835:186–225, 2016.
- [77] M. Bouchel, S. Callier, F. Dulucq, et al. SPIROC (SiPM Integrated Read-Out Chip): Dedicated very front-end electronics for an ILC prototype hadronic calorimeter with SiPM read-out. *Journal of Instrumentation*, 6:C01098, 2011.
- [78] Omega. User guide (draft). 2009.
- [79] Oskar Hartbrich. Investigation of the time measurement capabilities of the SPIROC2b ASIC. DESY summer student report, 2011.
- [80] Sebastian Piet Laurien. *Time resolved imaging calorimetry*. Ph.D. thesis, Universität Hamburg, 2018.

- [81] Mathias Reinecke. Performance of the large scale prototypes of the CALICE tile hadron calorimeter. In *2013 IEEE Nuclear Science Symposium and Medical Imaging Conference (2013 NSS/MIC)*, pages 1–5. IEEE, 2013.
- [82] Peter Göttlicher and CALICE collaboration. A concept for power cycling the electronics of CALICE-AHCAL with the train structure of ILC. *Physics Procedia*, 37:1586–1593, 2012.
- [83] Mathias Reinecke. Power pulsing of the CALICE tile hadron calorimeter. In *2016 IEEE Nuclear Science Symposium, Medical Imaging Conference and Room-Temperature Semiconductor Detector Workshop (NSS/MIC/RTSD)*, pages 1–6. IEEE, 2016.
- [84] Yuji Sudo. Temperature compensation and HG/LG inter-calibration, CALICE Meeting Shanghai. [https://agenda.linearcollider.org/event/7799/contributions/42262/attachments/33592/51488/TempComp\\_HGLGIC\\_201809\\_calice.pdf](https://agenda.linearcollider.org/event/7799/contributions/42262/attachments/33592/51488/TempComp_HGLGIC_201809_calice.pdf), 20th September 2018.
- [85] Jiri Kvasnicka. Data acquisition system for the CALICE AHCAL calorimeter. *Journal of Instrumentation*, 12(03):C03043, 2017.
- [86] Ambra Provenza. *Calibration and analysis of data taken with the technological prototype of the Analog Hadron Calorimeter (AHCAL) for a detector at the International Linear Collider*. Ph.D. thesis, DESY, 2018.
- [87] Christian Graf. Performance of a highly granular scintillator-SiPM based hadron calorimeter prototype in strong magnetic fields. In *2017 IEEE Nuclear Science Symposium and Medical Imaging Conference (NSS/MIC)*, pages 1–4. IEEE, 2017.
- [88] Yong Liu, Volker Büscher, Julien Caudron, et al. A design of scintillator tiles read out by surface-mounted SiPMs for a future hadron calorimeter. In *2014 IEEE Nuclear Science Symposium and Medical Imaging Conference (NSS/MIC)*, pages 1–4. IEEE, 2014.
- [89] F Gaede and J Engels. Marlin et al: A software framework for ILC detector R&D. *EUDET-Report-2007-11*, 2007.
- [90] Oskar Hartbrich. Commissioning and LED system tests of the Engineering Prototype of the Analog Hadronic Calorimeter of the CALICE Collaboration. Master Thesis, Universität Wuppertal, 2012.
- [91] Sarah Schröder. Commissioning of a prototype hadronic calorimeter. Master Thesis, Universität Hamburg, 2015.
- [92] Daniel Heuchel. Pedestal, MIP and inter-calibration, CALICE Meeting CERN. [https://agenda.linearcollider.org/event/8213/contributions/44354/attachments/34779/53694/DH\\_calice\\_9\\_19\\_ahcal\\_calibration\\_v2.pdf](https://agenda.linearcollider.org/event/8213/contributions/44354/attachments/34779/53694/DH_calice_9_19_ahcal_calibration_v2.pdf), 1st October 2019.

- [93] Olin Pinto. Gain and saturation calibration, CALICE Meeting CERN. [https://agenda.linearcollider.org/event/8213/contributions/44355/attachments/34782/53701/Gain\\_saturation\\_CALICE\\_CERN\\_20190930.pdf](https://agenda.linearcollider.org/event/8213/contributions/44355/attachments/34782/53701/Gain_saturation_CALICE_CERN_20190930.pdf), 1st October 2019.
- [94] CALICE collaboration. Application of software compensation to 2011 W-AHCALtest beam data. *CALICE Analysis Note*, 2018.
- [95] Christian Winter. Energy reconstruction with software compensation techniques in highly granular calorimeters. Master Thesis, TU München, 2019.
- [96] P. Mora de Freitas and H. Videau. Detector simulation with MOKKA / GEANT4: Present and future. In *Linear colliders. Proceedings, International Workshop on physics and experiments with future electron-positron linear colliders, LCWS 2002, Seogwipo, Jeju Island, Korea, August 26-30, 2002*, pages 623–627. 2002.
- [97] Markus Frank, F. Gaede, C. Grefe, et al. DD4hep: A detector description toolkit for high energy physics experiments. *Journal of Physics: Conference Series*, 513:022010, 2014.
- [98] M Hirschberg, R Beckmann, U Brandenburg, et al. Precise measurement of Birks kB parameter in plastic scintillators. *IEEE Transactions on Nuclear Science*, 39(4):511–514, 1992.
- [99] D Dannheim, W Klempt, and E van der Kraaij. Beam tests with the CALICE tungsten analog hadronic calorimeter prototype. Apr 2012.
- [100] Oskar Hartbrich. *Scintillator calorimeters for a future linear collider experiment*. Ph.D. thesis, Hasylab, DESY, 2016.
- [101] Marco Ramilli. Towards hadronic shower timing with CALICE ANALOG Hadron Calorimeter. 2013.
- [102] CALICE collaboration. Shower development of particles with momenta from 1 to 10 GeV in the CALICE Scintillator-Tungsten HCAL. *CALICE Analysis Note CAN-036*, 2011.
- [103] Katja Krüger. private communication.
- [104] H6 manual. <http://sba.web.cern.ch/sba/BeamsAndAreas/h6/H6manual.pdf>, May 2000.
- [105] CALICE collaboration. Shower development of particles with momenta from 10 to 100 GeV in the CALICE Scintillator-Tungsten HCAL. *CALICE Analysis Note*, 2013.
- [106] Di Lorenzo et al. SPIROC: Design and performances of a dedicated very front-end electronics for an ILC Analog Hadronic CALorimeter (AHCAL) prototype with SiPM read-out. *Journal of Instrumentation*, 8(01):C01027, 2013.

- [107] Eldwan Brianne. Studies of the front-end electronics of the Analog HCAL. DESY summer student report, 2012.
- [108] Martin A Fischler and Robert C Bolles. Random sample consensus: a paradigm for model fitting with applications to image analysis and automated cartography. *Communications of the ACM*, 24(6):381–395, 1981.
- [109] SciPy community. SciPy v0.21.1 reference guide. [https://scikit-learn.org/stable/modules/generated/sklearn.linear\\_model.RANSACRegressor.html](https://scikit-learn.org/stable/modules/generated/sklearn.linear_model.RANSACRegressor.html), May 2019.
- [110] Peter J Rousseeuw. Least median of squares regression. *Journal of the American statistical association*, 79(388):871–880, 1984.
- [111] ROOT Reference Guide v6.17. <https://root.cern.ch/doc/master/classTLinearFitter.html>, May 2019.
- [112] Henri Theil. A rank-invariant method of linear and polynomial regression analysis. In *Henri Theil's contributions to economics and econometrics*, pages 345–381. Springer, 1992.
- [113] SciPy community. SciPy v0.21.1 Reference Guide. [https://scikit-learn.org/stable/auto\\_examples/linear\\_model/plot\\_theilsen.html](https://scikit-learn.org/stable/auto_examples/linear_model/plot_theilsen.html), May 2019.
- [114] Lorenz Emberger. Timing calibration, CALICE Meeting CERN. <https://agenda.linearcollider.org/event/8213/contributions/44356/attachments/34776/53688/EmbergerTimingCERN.pdf>, 1st October 2019.
- [115] Jiri Kvasnicka. Private communication, 2017.
- [116] J. Apostolakis et al. Geant4 physics lists for HEP. *2008 IEEE Nuclear Science Symposium Conference Record*, 2008.
- [117] T Kamon, K Kondo, A Yamashita, et al. A new scintillator and wavelength shifter. *Nuclear Instruments and Methods in Physics Research*, 213(2-3):261–269, 1983.
- [118] Klaus Alexander Tadday. *Scintillation light detection and application of silicon photo-multipliers in imaging calorimetry and positron emission tomography*. Ph.D. thesis, Universität Hamburg, 2011.
- [119] Frank Simon et al. The time structure of hadronic showers in imaging calorimeters with scintillator and RPC readout. *arXiv preprint arXiv:1308.6395*, 2013.
- [120] Alberto Ribon. Private communication.
- [121] Andrea Benaglia, Etienne Auffray, Paul Lecoq, et al. Space-time development of electromagnetic and hadronic showers and perspectives for novel calorimetric techniques. 63:574–579, 04 2016.

- [122] K Gadow, E Garutti, P Göttlicher, et al. Concept, realization and results of the mechanical and electronics integration efforts for an analog hadronic calorimeter. *EUDET-Report-2010-02*, 55, 2010.
- [123] Katja Krüger. AHCAL testbeam report, CALICE Meeting Shanghai. [https://agenda.linearcollider.org/event/7799/contributions/42261/attachments/33583/51471/AHCALtestbeams2018\\_CALICEShanghai\\_20180920.pdf](https://agenda.linearcollider.org/event/7799/contributions/42261/attachments/33583/51471/AHCALtestbeams2018_CALICEShanghai_20180920.pdf), 20. September 2018.
- [124] F Simon, C Soldner, and L Weuste. T3B - an experiment to measure the time structure of hadronic showers. *Journal of Instrumentation*, 8(12):P12001, 2013.
- [125] Marina Chadeeva. A new approach to software compensation for the CALICE AHCAL. *CALICE Analysis Note*, 2010.
- [126] Katja Seidel. *Top quark pair production and calorimeter energy resolution studies at a future collider experiment*. Ph.D. thesis, Ludwigs-Maximilians-Universität München, 2012.
- [127] Katja Seidel and Frank Simon. Software compensation for hadronic showers in the CALICE AHCAL and tail catcher with cluster-based methods. 2010.
- [128] Yanming Guo, Yu Liu, Ard Oerlemans, et al. Deep learning for visual understanding: A review. *Neurocomputing*, 187:27–48, 2016.
- [129] Tom Young, Devamanyu Hazarika, Soujanya Poria, et al. Recent trends in deep learning based natural language processing. *IEEE Computational intelligence magazine*, 13(3):55–75, 2018.
- [130] David Silver, Julian Schrittwieser, Karen Simonyan, et al. Mastering the game of go without human knowledge. *Nature*, 550(7676):354–359, 2017.
- [131] Leo Bellantoni, JS Conway, JE Jacobsen, et al. Using neural networks with jet shapes to identify b jets in  $e^+e^-$  interactions. *Nuclear Instruments and Methods in Physics Research Section A*, 310(3):618–622, 1991.
- [132] Sara Neuhaus, Sebastian Skambraks, Fernando Abudinén, et al. A neural network z-vertex trigger for Belle II. In *Journal of Physics: Conference Series*, volume 608, page 012052. IOP Publishing, 2015.
- [133] Pierre Baldi, Peter Sadowski, and Daniel Whiteson. Searching for exotic particles in high-energy physics with deep learning. *Nature communications*, 5:4308, 2014.
- [134] Markus Stoye, Jan Kieseler, Huilin Qu, et al. Deepjet: Generic physics object based jet multiclass classification for lhc experiments. In *NIPS Workshop on Deep Learning for Physical Sciences*, volume 36. 2017.

- 
- [135] Martin Erdmann, Jonas Glombitza, and Thorben Quast. Precise simulation of electromagnetic calorimeter showers using a Wasserstein Generative Adversarial Network. *Comput. Softw. Big Sci.*, 3(1):4, 2019.
- [136] ATLAS Collaboration. Deep generative models for fast shower simulation in ATLAS. Technical Report ATL-SOFT-PUB-2018-001, CERN, Jul 2018.
- [137] Nitish Srivastava, Geoffrey Hinton, Alex Krizhevsky, et al. Dropout: A simple way to prevent neural networks from overfitting. *The journal of machine learning research*, 15(1):1929–1958, 2014.
- [138] Simon Schnake. Energy regression with deep learning in particle collider physics. Master Thesis, Universität Hamburg.
- [139] François Chollet et al. Keras. <https://keras.io>, 2015.
- [140] Martín Abadi et al. TensorFlow: Large-scale machine learning on heterogeneous systems, 2015. Software available from [tensorflow.org](https://www.tensorflow.org).
- [141] Diederik P Kingma and Jimmy Ba. Adam: A method for stochastic optimization. *arXiv preprint arXiv:1412.6980*, 2014.
- [142] A Caldwell, L Hervas, JA Parsons, et al. Measurement of the time development of particle showers in a uranium scintillator calorimeter. *Nuclear Instruments and Methods in Physics Research Section A*, 330(3):389–404, 1993.
- [143] J Butler, D Contardo, M Klute, et al. CMS phase II upgrade scope document. Technical Report CERN-LHCC-2015-019. LHCC-G-165, CERN, Sep 2015.
- [144] Erik Buhmann. Deep learning based energy reconstruction for the CALICE AHCAL. Master Thesis, Universität Hamburg, July 2019.



# Acknowledgements

First and foremost, I would like to express my gratitude to my supervisor Frank Simon. I profited greatly from countless discussions, your patient answers to all my questions and lots of advice. Your constant support and guidance are inspiring. I could not have asked for a better supervisor.

I would also like to thank my thesis advisor Prof. Allen Caldwell for giving me the opportunity to perform my PhD at the MPP. I profited from many interesting suggestions and I especially enjoyed the task as a teaching assistant in the data analysis lecture. Furthermore, I would like to thank Prof. Bastian Märkisch and Prof. Andreas Weiler for agreeing to be on my thesis committee.

I am grateful to all current and former members of the Future Detectors group: Christian, Daniel, Hendrik, Ivan, Justin, Lorenz, Malinda, Miro, Naomi, Thomas, Yasmine, and the whole Belle II group for the entertaining lunch and coffee breaks, the great work atmosphere and the occasional kicker matches. I would like to thank my former office mate Marco for a lot of help and the interesting discussions related to physics or not. A special thank you goes to Andi and Hendrik for the intense table tennis matches.

I would like to thank all members of the CALICE collaboration, especially Ambra, Amine, Anna, Eldwan, Erik, Jiri, Linghui, Naoki, Olin, Saiva, Tatsuro, Vladimir, Yuji, Katja and Felix for the amazing collaboration and the great time at test beam campaigns, meetings and especially in Tokyo. Thank you Eldwan for lots of help with the software. I am very grateful to Katja Krüger and Felix Sefkow for many discussions and suggestions.

I would especially like to thank Frank Simon, Christian Kiesling, Miroslav Gabriel, Lorenz Emberger, Thibaud Humair and Isabell Bludau for proof reading this thesis.

Finally, I would like to say thank you to my whole family. Your support throughout all the years is helping me in everything I do. Thank you Isa! For all the support and the amazing time together.